Alma Mater Studiorum – Università di Bologna

School of Science
Department of Physics and Astronomy
Master Degree Programme in Astrophysics and Cosmology

Study and test of alignment techniques for extremely large-scale telescopes' instrumentation

Graduation Thesis

Presented by:
Diego Gilioli

Supervisor:
Chiar.mo Prof. Gabriele Umbriaco

Co-supervisor:
Dott. Gabriele Rodeghiero

Academic year 2024–2025
Graduation date XXXI, XX, MMXXV

Abstract

In the context of the INAF instrumentation development program for the MORFEO instrument at the Extremely Large Telescope (ELT), I tested an optical alignment procedure based exclusively on the ghost reflections, without introducing any external target into the system. MORFEO, the multi-conjugate adaptive optics system for the ELT, contains both natural and Laser Guide Star (LGS) wavefront sensors. The alignment technique has been proposed for the alignment of the Laser Guide Stars Objective (LGSO) to MORFEO. To assess the reliability of this technique, I built a laboratory prototype to study its advantages and criticalities. The system was made of 2 commercial lenses illuminated by a point-like source; the 1st lens was a collimator lens, while the 2nd was a converging lens. I used the Micro Alignment Telescope (MAT) to set the reference of the optical axis and observe the ghosts, analyzing them using Python codes. From the analysis of the position of the centroid of the ghosts, both lenses resulted aligned with ~ 5 μm of residual error in decenter and $\sim 5 - 10$" of residual error in tilt. I applied the results retrieved with the lab prototype to a ray tracing simulation environment with the MORFEO LGSO, demonstrating a potential alignment residual error of ~ 10 μm in decenter and ~ 2" in tilt. Comparing these values with the LGSO alignment requirements, decenter < 1 mm and tilt < 360", the ghost alignment technique proves to be reliable and yields better results than other methods considered, such as laser tracker and back reflections techniques.

Index

List of Acronyms

In this section, the main acronyms and abbreviations used throughout the text are listed.

Acronym	**Meaning**
AGN	Active Galactic Nuclei
AO	Adaptive Optics
BH	Black Hole
BIH	Bologna Integration Hall
CBS	Cubic Beam Splitter
CMOS	Complementary Metal–Oxide–Semiconductor
CP	Corrective Plate
DIC	Dichroic
DM	Deformable Mirror
d.o.f.	Degree of Freedom
EE	Encircled Energy
ELT	Extremely Large Telescope
FFT	Fourier Transform
ESO	European Southern Observatory
FFT^{-1}	Inverse Fourier Transform
FM	Folding Mirror
FoV	Field of View
FWHM	Full Width Half Maximum
GLAO	Ground-Layer Adaptive Optics
HO	High Order
IMBH	Intermediate-Mass Black Hole
IMF	Initial Mass Function
INAF	National Institute for Astrophysics
JWST	James Webb Space Telescope
LGS	Laser Guide Star
LGSO	Laser Guide Stars Objective
LO	Low Order
LOR	Low Order and Reference
LT	Laser Tracker
MAT	Micro Alignment Telescope
MCAO	Multi-Conjugate Adaptive Optics
MMSE	Minimum Mean Square Error
MICADO	Multi-AO Imaging Camera for Deep Observations
MORFEO	Multi-Conjugate Adaptive Optics Relay for ELT Observations
MTF	Modulation Transfer Function
NGS	Natural Guide Star
NIR	Near-Infrared (light)
PIP	Point-Image-Point
POLC	Pseudo-Open Loop Control
PSF	Point Spread Function

Acronym	**Meaning**
RI	Relative Intensity
ROI	Region Of Interest
RTC	Real-Time Computer
SCAO	Single-Conjugate Adaptive Optics
SF	Star Formation
SFR	Star Formation Rate
SH	Shack–Hartmann
SMBH	Supermassive Black Hole
SQ	Sequential
SR	Strehl Ratio
TIFF	Tagged Image File Format
TT	Tip-Tilt
UNIBO	University of Bologna
UV	Ultraviolet (light)
VCM	Voice Coil Motors
VIS	Visible (light)
WF	Wavefront
WFE	Wavefront Error
WFS	Wavefront Sensor

Chapter 1

Introduction

The European Southern Observatory (ESO)[1] is a consortium of several European institutes of research, with the aim of designing and developing advanced telescopes for astrophysical observation in the Southern hemisphere. The latest, in-construction telescope is the Extremely Large Telescope (ELT)[1], whose first light is planned to be in 2029; ELT is a revolutionary telescope that will be equipped with several subsystems in order to perform different types of observations simultaneously. ELT, whose primary mirror has diameter $D = 39$ m, will be the largest optical telescope ever build. Each ESO member country is responsible for developing a specific instrument, but they also collaborate with other countries to ensure the final integration into the ELT. In particular, the Italian contribution is the Multiconjugate adaptive Optics Relay For ELT Observations (MORFEO) for an infrared imager camera, which will study the exoplanets and the resolved stars in our galaxy. Several Italian universities and research centers participate in the MORFEO consortium, and each of them has a specific task to accomplish. The Alma Mater Studiorum - University of Bologna (UNIBO) and the National Institute for Astrophysics in Bologna (INAF-OAS) are already working on the integration of each subsystem of MORFEO. The Bologna Integration Hall (BIH) of MORFEO will be the location in which the components will be mounted, calibrated, and tested before being sent to the ELT facility in Chile. This strategy allows us to characterize the instrument and eventually correct and improve its design and performance, before being mounted at its final destination.

During my thesis, I worked under the supervision of Prof. Gabriele Umbriaco and Dr. Gabriele Rodeghiero, in the facilities of UNIBO and INAF-OAS. I was assigned to an innovative project scheduled by the MORFEO Consortium: the study of the feasibility and criticalities for a potential alignment technique planned for the alignment of the LGSO module to MORFEO. This method relies on the ghosts alignment and is a relatively new topic of research and development of the instruments, which has been proposed by joint research on INAF and Officina Stellare[2]. My role was to understand how to perform the analysis on a laboratory prototype, study the alignment residual errors, estimate the results of the LGSO alignment (based on the prototype results) and compare them with the requirements. The alignment accuracy required by the MORFEO consortium is necessary for a correct observation of the Laser Guide Stars, and from simulations, they have been established as: maximum residual error = 1000 μmion decenter and maximum residual error = 360”[3] in tilt .

I worked as an optical engineer, designing optical systems using Zemax OpticStudio software, realizing them in the laboratory using optical and photonic instrumentation, and analyzing the results using Python scripts. I could not work on the MORFEO LGSO because it is still in the design phase, and building a physical model of the system would have been inefficient in terms of costs and time. Thus, I applied the results obtained in the laboratory to the LGSO simulated in Zemax.

1.1 Overview on alignment techniques

In case of small misalignment, the error can be calculated using the 1st order approximated formula for small angles ($\theta \approx \tan\theta$)

$$\Delta\theta = \frac{\Delta x}{L} \tag{1.1}$$

In which Δx is the spatial difference between the target position and the achieved position, and L is the optical path length between the source and the target. The result is expressed in radians, but can be converted to arcseconds by multiplying by 206265. Many alignment methods[4][5] can be conducted automatically or manually. The coarse alignment is performed using masks, dowel pins, and kinematics mounts; while the fine alignment techniques are more varied and are typically conducted using instruments like lasers, interferometers, and Wavefront Sensors (WFS).

1.1.1 Laser tracker

One of the most used alignment techniques, also proposed for the alignment of the LGSO, is based on the use of a Laser Tracker (LT): the tracker is placed in a reference, stable location and fires lasers on target objects, which reflect the laser back. These are typically Spherically Mounted Retro-reflectors (SMR), mechanical components located on the instrument to align. Inside the tracker, the reflected lasers are detected and the real-time distance is measured by interferometry or by the time passed between the firing and the receiving of the laser; moreover, the angle of incidence of the laser is measured, providing the 3D location of the SMR. The use of multiple SMR on the object allows the fit of its overall position, guaranteed by the tolerance on the position of each SMR of $\sim 50\ \mu$m. However, since the mechanical positioning of the SMR introduces additional errors, MORFEO consortium estimated that the LGSO alignment conducted using a LT and 5 SMR will be able to achieve uncertainty of $\approx 0.1 - 0.8$ mm in decenter and $\approx 0.3 - 5'$ in tilt.

1.1.2 Laser back reflection

An alternative solution is to use the back reflected laser spots of the lenses faces; these observables are originated by the reflectivity of the lenses, which transmit the majority of the laser beam and reflect a small fraction of it. Using back reflection coming from several lenses and fitting their positions, it is possible to achieve alignment residuals on the order of $\sim 10\ \mu$m. This technique typically offers a reliable and relatively cheap solution, however it is not optimal for the LGSO alignment. In fact, the laser divergence is not negligible, especially in this case, when the beam travels for tens of meters before reaching the target. Achieving the required collimation accuracy is technically challenging, resulting in the spot on the LGSO lenses being too large to provide an accurate characterization of the back reflection. Moreover, lasers are monochromatic, thus susceptible to interference, parasite phenomena.

1.1.3 Wavefront sensors alignment

The fine alignment can be also performed using the wavefront sensors of the LGSO itself, capable of detecting the decenter of a light beam with respect to a reference position. However, this technique is affected by the error introduced when the light beam crosses the optics of the LGSO, resulting in lower accuracy compared to the other methods. Moreover, if the source is a laser, interference of the monochromatic wavelength is an issue; if the light is polychromatic, the different wavelengths have different focus positions (chromatism).

1.1.4 Ghost alignment technique

The technique I tested for aligning the prototype lenses was based on the ghost reflections generated by the lenses themselves, as dictated by Snell's law: when a ray impacts on a lens, a small percentage of light is reflected, because the light coming from the air encounters a different, refractive medium (fig.1.2). Depending on the quality, on the material and on the coating of the lens, the reflectivity can change, but a good approximation for the commercial lenses is $\approx 1-5\%$ reflectance and $99-95\%$ transmittance. Ghosts are parasite effects of optical systems and astronomers typically want to reduce them, since are an obstacle for a correct observation, as shown in fig.1.1b. Considering an ideal spherical lens, without manufacturing residuals or wedge, the single reflection (1st generation) ghosts are focused along the optical axis of the lens, approximately at a distance equal to half of the curvature radius. The optical axis of the lens is the rotational symmetry line that crosses its center. However, there also exist multiple reflection

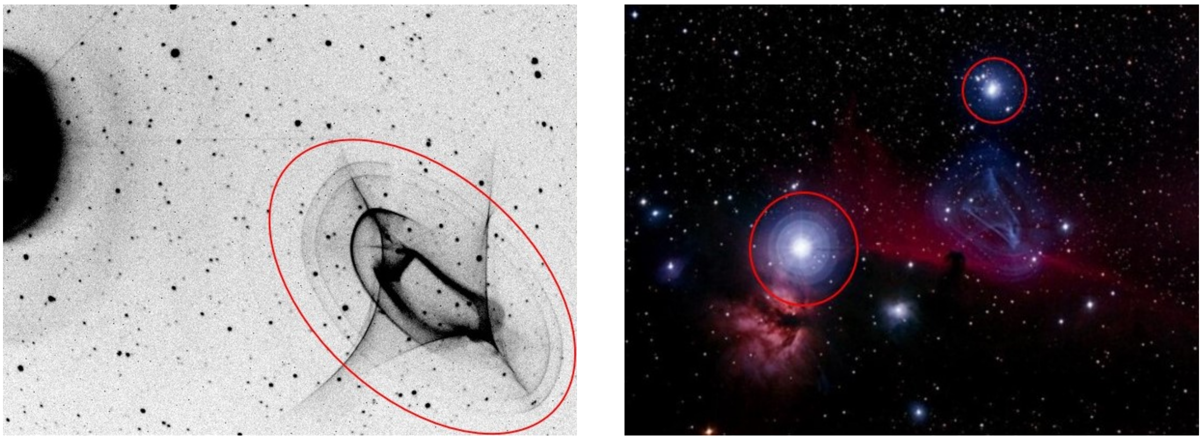
(a) (b)

Figure 1.1: Effect of the parasite ghost in 2 different astrophysics images: (a) raw (Credits: [6]) and (b) processed images (Credits: [7]). The ghosts are surrounded by a red circle.

ghosts, in which light is reflected by many surfaces of the same lens or by surfaces of different lenses. The wedge is the tilt between the mechanical axis, defined by the outer diameter of the lens, and the optical axis, which is defined by the optical surfaces of the lens. The surface of the lens is the area of contact between 2 different materials: in most cases, it is between the lens material and the air, but in the case of a double or triple lens, it is also where the single lenses are attached. During my thesis, I worked on the alignment of commercial lenses in order to characterize a possible workflow that could be applied to the LGSO alignment. Each lens I used was a doublet and produced at least 2 ghosts. Since the ghosts are focused on the axis crossing the center of the lens, the line between 2 ghosts from the same lens establishes the optical axis of the lens itself. Hence, the alignment of the 2 aforementioned ghosts to a reference implies the alignment of the optical axis of the lens to the same reference. The advantage of this technique is that it does not require any additional reference targets or any optomechanical crosshair, since the ghosts themselves act as optical targets, increasing the accuracy of the procedure.

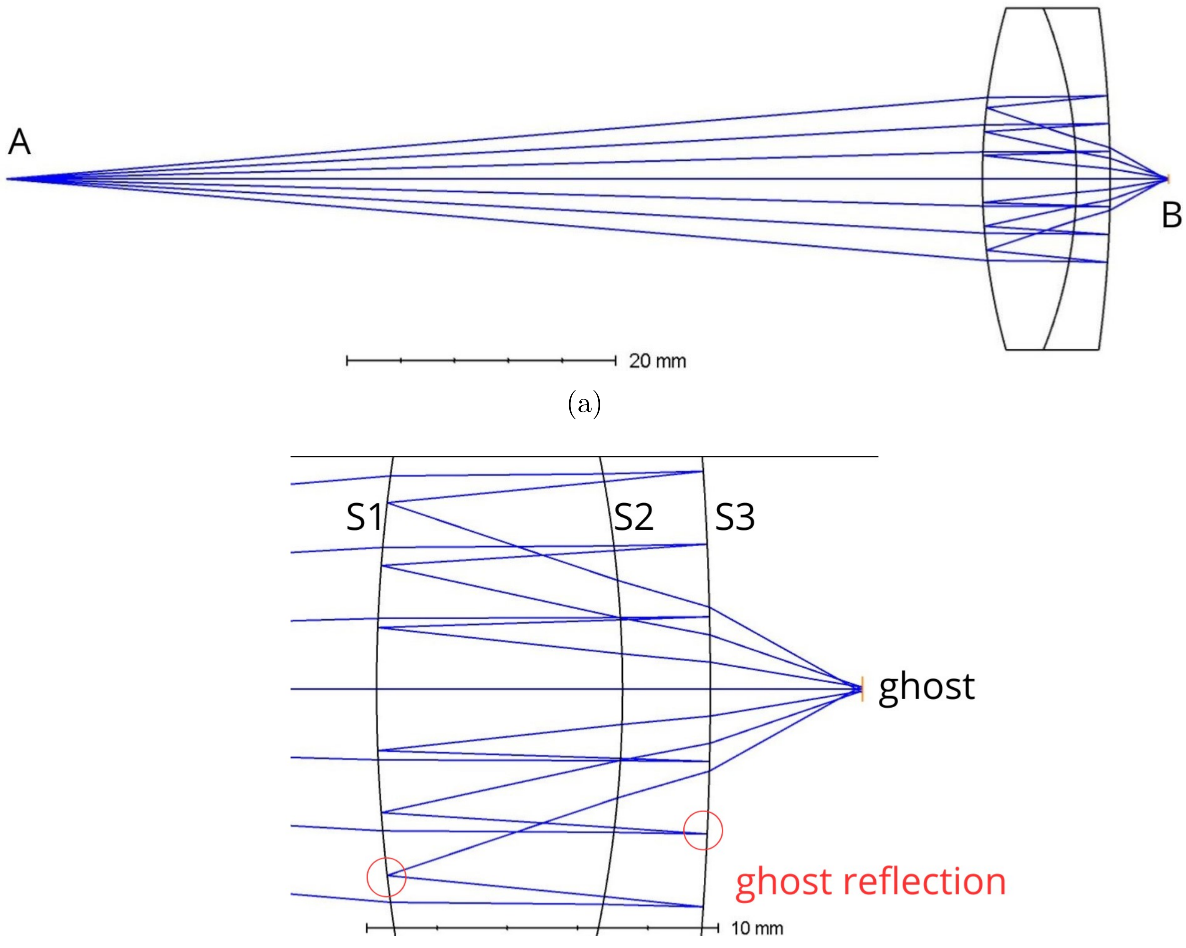

(a)

(b)

Figure 1.2: Zemax ghost analysis, in which the blue line represents light rays: (a) 2nd generation ghost originated by the multiple reflection in one of the commercial lenses of the lab prototype, in which A stands for the illumination source and B for the focus of the ghost. (b) Zoom on the lens that forms the ghost; the names of the surfaces are indicated with S1, S2 and S3, the reflections of the light on the surfaces are circled in red. The reflection on S3 is 1st generation, while on S2 is 2nd generation.

Chapter 2

Adaptive Optics

2.1 Atmospheric turbulence

In visible (VIS), near infrared (NIR), and (near) ultraviolet (UV) bands, the atmospheric turbulence and the telescopes' manufacturing errors perturb the Wavefront (WF) of the collected light, causing aberrations. Aberrations are changes of the position, shape, and dimension of the Point Spread Function (PSF) on the Focal Plane (FP). Aberrated wavefronts are decomposed using Zernike polynomials, which are orthonormal in a unit circle, so each of them has an independent and characteristic effect on the PSF. The first 13 modes of Zernike contain 95% of the turbulence aberration power spectrum; hence they have the strongest effect on the PSF. The impact given by the hardware of the telescope is dependent on manufacturing residuals (which do not change in time) and on the instantaneous instrument conditions (i.e., temperature and vibrations); the impact derived from the atmospheric conditions depends on the refractive index of the air, which follows the equation

$$n - 1 = \frac{77.6 \cdot 10^{-6}}{T}\left(1 + 7.52 \cdot 10^{-3}\lambda^{-2}\right)\left(p + 4810\frac{v}{T}\right) \tag{2.1}$$

where λ is the observation wavelength, T is the temperature, v is the water vapor pressure and p is the air pressure. Since the atmosphere can be considered as a superposition of turbulent layers, the flat wavefront coming from an infinite distance, experiences the sum of the effects of every layer. The ground layer is typically the one that provides the heaviest perturbations to the wavefront, while above 20 km of altitude, perturbations are negligible due to the very low air density. The turbulent layers are a few meters thick, so it is reasonable to assume that the atmospheric parameters of Eq.2.1 are constant within the same layer. They influence the coherence length r_0, the distance over which a wave maintains a constant phase shift, which is assumed to be the size of the atmospheric air bubbles. Moreover, $r_0 \propto \lambda^{6/5}$, so the longer wavelengths undergo less perturbation. If the ratio between the diameter of the telescope and r_0 is $\lesssim 5$, the main effect of the aberration is the decenter of the PSF on the focal plane, while if the ratio increases, the main effect is the speckle (jitter) of the image. In both cases, sampling with a short exposure time leads to the detection of the incorrect wavefront; hence, one of the solutions is to increase the exposure time. However, it increases the size of the PSF and, as a consequence, decreases the resolution of the system. For this reason, ground-based telescopes are limited by the atmosphere, known as seeing-limited telescopes. Another important feature is the isoplanatic angle, which is the maximum angular distance at which two sources are seen through the same air bubble, being affected by the same perturbations. It is defined in Eq.2.2, where h is the altitude of the turbulent layer.

$$\theta_0 \approx 0.6 \frac{r_0}{h} \tag{2.2}$$

The coherence time, which represents the timescale in which the perturbation is constant, depends on the wind velocity w and is calculated with the equation

$$\tau_0 \approx \frac{r_0}{w} \tag{2.3}$$

These quantities indicate that the wavefront correction must be calibrated and optimized for the wavelength of the observation and can be summarized and approximated as the values reported in Table 2.1.

Parameter	**Visible** (0.5 μm)	**IR** (2.2 μm)
Fried's parameter r_0 (m)	0.20	1.35
Seeing disk (arcsecond)	0.5	0.33
Coherence time τ_0 (ms)	10	50
Isoplanatic angle θ_0 (arcseconds)	2	10

Table 2.1: Atmospheric turbulence parameters at different wavelengths.

τ_0 is the reason behind the fact that the wavefront correction is applied mainly to NIR bands, while in VIS and UV, the correction systems still lack efficiency.

2.2 Correction techniques

To reduce the seeing in ground-based observation, new generation telescopes and especially the ELT, are build to minimize the turbulence in proximity to the collecting mirror. The observatory is built at Cerro Armazones, in the Atacama Desert, in Chile, a location chosen because of the negligible light pollution, dry climate, and high altitude (3046 m). Due to the altitude, the atmospheric thickness and density are reduced with respect of a lower altitude instrument, decreasing also the magnitude of the turbulence. Moreover, the Andes mountains are responsible for a quasi-permanent inversion layer located at a lower altitude than Cerro Armazones, which allows ELT to be in a relatively low-turbulence region. The dome is designed to let wind to pass through freely, minimizing the turbulence around the building. The dome is the biggest ever built for a telescope, ≈ 80 m high with a diameter ≈ 93 m; however, the ratio between its dimension and the telescope's one is smaller with respect to older generation instruments, which helps maintain a lower thermal gradient between the instrument and the atmosphere, thereby reducing the turbulence caused by the rise of warm air.

Adaptive Optics (AO) is a technology that aims to improve the quality of ground-based telescopes with a real-time correction of the incoming light beam. It represents a cheaper alternative to space-based telescopes, allowing the construction of resolved, large-aperture telescopes. The main parameters for a telescope are the etendue, which is the quantity of light captured by the instrument and scales as D^2, and the resolution, which is the minimum angular distance between 2 distinct sources. Space-based telescopes achieve diffraction-limited resolution, which follows the equation

$$Res \approx 1.22 \frac{\lambda}{D} \text{ [rad]} \tag{2.4}$$

since they are outside the atmosphere. Due to engineering and cost limitations, the biggest optical space-based telescope is the James Webb Space Telescope (JWST), whose primary mirror has D = 6.5 m, providing Res $\approx$ 0.04” at $\lambda = 1$ μm. The sensitivity of JWST is much lower than the sensitivity of ELT, in fact ELT observations at $\lambda \approx 10$ μm have a continuum sensitivity of ≈ 50 mJy, while at the same wavelength JWST continuum sensitivity drops to ≈ 0.01 mJy [8]. However, the atmospheric seeing reduces the resolution of ELT to ≈ 0.5”.
In order to correct the incoming wavefront, AO relies on three main instruments: Wavefront Sensors (WFS), Real-Time Computers (RTC), and Deformable Mirrors (DM)[9]. WFSs have the goal of detecting the change of the wavefront of a reference source; usually, the references are Natural Guide Stars (NGS) and/or Laser Guide Stars (LGS), which are well-studied, isolated, and luminous objects, whose non-aberrated wavefront is deeply known. Once the perturbed wavefront is observed, a correction matrix is computed and converted by the RTC into a mechanical command for the DM in a time shorter than τ_0, typically a few ms. DMs are made of hundreds or thousands of small actuators that can be lifted or lowered by necessity, at a frequency of $\sim 500-1000$ Hz, to provide wavefront correction within the coherence time, reshaping the light beam phase. The more actuators are present in a DM, the higher the number of modes of aberration that can be corrected by the mirror itself. Each DM works with 1 RTC and can be conjugated only to 1 atmospheric layer correction, hence the more DMs are present in a system, the more accurate is the computation of turbulence layers and their correction. The conjugation with the turbulence layers cannot be changed during the operational time of the AO system (it would be necessary to recalibrate the entire setup), so the study cases, the location, and the atmospheric features of the telescope are deeply studied and modeled before the instrument construction and regulation. To correct the wavefront, the DMs are shaped with a profile that is the negative of half of the measured aberrations, so every part of the wavefront impacts the following mirror within a shorter time range, behaving like a flatter wavefront. To understand the importance of AO, fig.2.1[10] shows the results of two sampling campaigns before and after the correction. There exist several AO systems[13], as shown in fig.2.2. The most common ones are the Single-Conjugated Adaptive Optics (SCAO), the Laser Tomography Adaptive Optics (LTAO), the Ground Layer Adaptive Optics (GLAO), and the Multi-Conjugate Adaptive Optics (MCAO); the MCAO is the configuration that provides the wider Field of View (FoV) and resolved PSF. SCAO is based on the reference of NGS, and the correction relies only on a single AO system; it is limited in the order of aberration that can be corrected and in the Strehl Ratio (SR), which is the ratio between the peak intensity achieved by the system and the diffraction-limited one. LTAO relies on the reference of LGS, performing high-order corrections, but is limited in the low-order ones; its performance is similar to that of an SCAO. MCAO relies on the reference of both NGS and LGS respectively for the low and high orders of aberrations, and the DMs are conjugated with several turbulent layers. GLAO is a setup optimized for wide FoV, in fact the reference are several NGS over a large portion of the sky. The LGS are a reflection in the upper atmosphere, caused by the LGS launchers firing a laser (at different wavelength) to stimulate the atmosphere in emitting back a collimated beam. In particular, the Na-layer LGS are originated by the excitation of a thin Sodium layer located at ~ 100 km altitude.

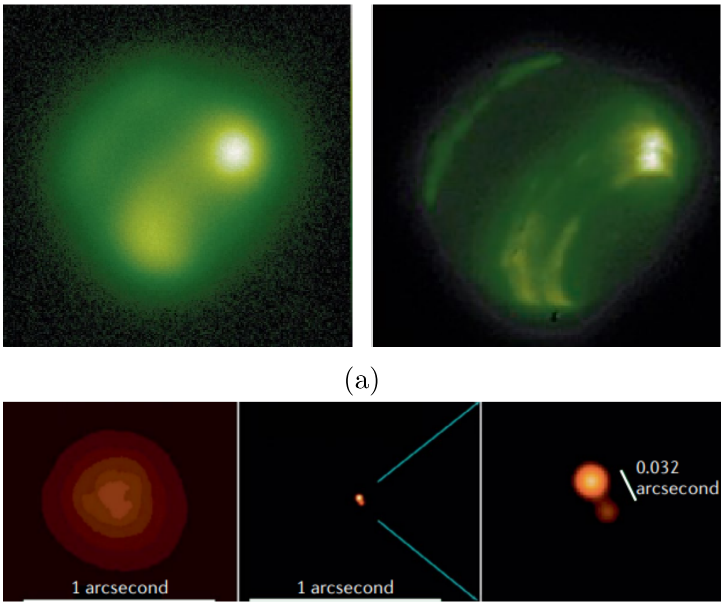

(a)

(b)

Figure 2.1: Examples of the impact of adaptive optics in planetary and stellar science. (a) Early Keck AO system[11] demonstrating the benefits in planetary science: Neptune is shown in a narrow filter at 1.17 μm, on the left is uncorrected in 0.4″ seeing, while on the right is seen with AO correction. (b) High-resolution AO in visible light on a 6.5 m telescope with Magellan AO (MagAO)[12], showing Theta 1 Ori C, a known tight binary. Left: AO off; middle: AO on (same field of view); right: zoom on the star, demonstrating large telescope AO resolution.

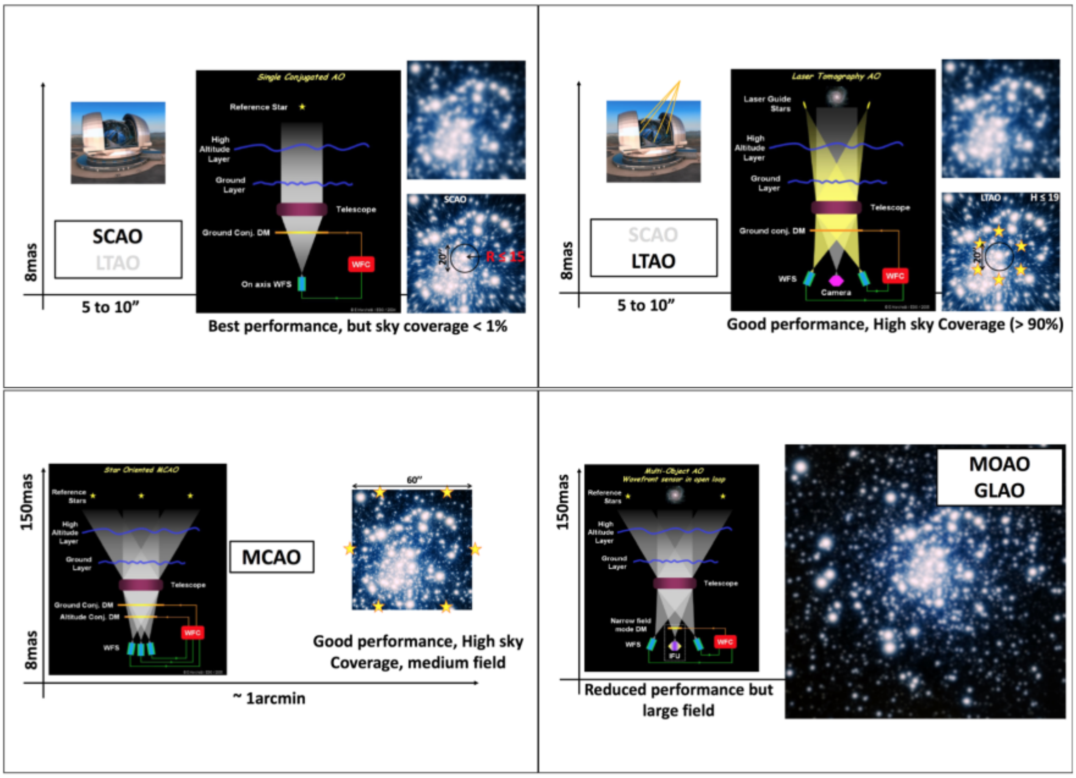

Figure 2.2: Different types of AO systems and the performance that they achieve. Credits: [1]

2.3 MORFEO

MORFEO[14] [15] is a ELT first-generation AO instrument that will be mounted on the ELT facility to compensate the distortion of the incoming light derived by the Earth's atmospheric turbulence, providing a diffraction limited correction (0.006" at $\lambda = 1\ \mu$m) over a 60" field to the the Multi-AO Imaging Camera for Deep Observations (MICADO). MORFEO, shown in Fig.2.3, is a post-focal instrument, made of 8 mirrors, whose positions are constantly monitored by a laser tracker, and eventually adjusted. The MORFEO science path[16] begins from the focal plane of the telescope, where light is reflected by the 8 mirrors until it arrives in the image plane, which corresponds to the focal plane of MICADO. MORFEO has a technical field of view of 160", although only the innermost 60" are for scientific purposes with a magnification of 1:1. The mirrors are named from M6 to M12 (from M1 to M5 are ELT mirrors); M9 and M10 are respectively called also DM1 and DM2 and are the two post-focal deformable mirrors of MORFEO. There is also a dichroic (DIC), which separates the incoming light into 2 different paths: VIS light is transmitted in the LGS path, while NIR light is reflected in the science path. VIS light coming from the LGS feeds the LGSO to be a reference for the atmospheric perturbation of the light. NIR light ($0.8 - 2.2\ \mu$m) feeds MICADO and the NGS-WFS, while VIS light is used by the LGS-WFS[17]. The choice to reflect the NIR light and to transmit the VIS bands is not casual: in fact, the reflection does not bring any aberrations, whereas the transmission through a dichroic (made of silica, a refractive material) introduces aberrations in the beam. Crossing a refractive medium, typically implies chromatism, which is the aberration caused by different wavelengths of light do not converge at a single point, leading to different focus positions depending on the wavelength. However, the LGS path is monochromatic, so the problem is basically negligible.

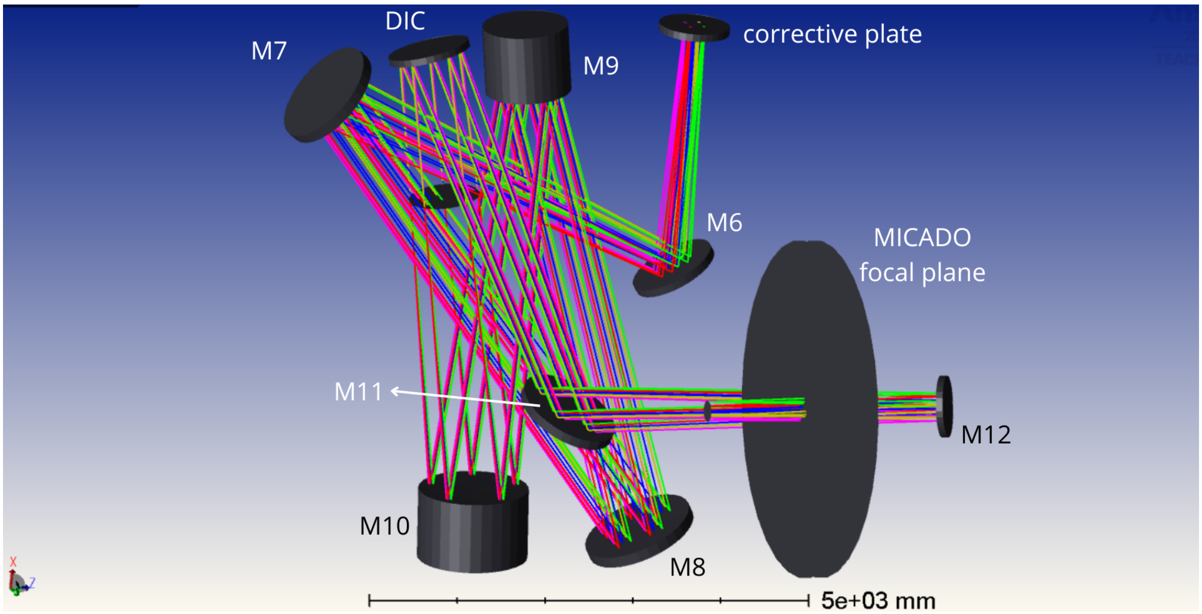

Figure 2.3: Zemax configuration of the scientific path of MORFEO; the light comes from the focal plane of ELT, and arrives in the MICADO FP. The rays are simulated with different colors to represent different fields (angle of incidence) of the arrival on ELT M1.

2.3.1 MORFEO's MCAO

MORFEO is an innovative system, especially for the MCAO technology, which expands the FoV of the correction with respect to other AO setups. Due to the complexity and the costs of the systems, even in the most advanced MCAO apparatus, MORFEO, only 3 turbulent layers are taken into account for the correction: the ground layer, close to the telescope aperture, and the other 2 higher layers. In other AO configurations, the NGS are used when their distance is within ≈ 30" from the target (θ_0 in NIR), while the LGS are used when no other available reference is located within θ_0. Instead, MORFEO relies on the reference of 3 NGS-WFS and 6 LGS-WFS at the same time. The NGS path and the LGS path work simultaneously to investigate slightly different regions of the sky: both are detected in the area centered on the target, the LGS within a diameter of 60", whereas the NGS are detected in an annulus between 60" $-$ 160" diameter, using pick-off mirrors to capture their light. The NGS-WFS are part of MICADO module, and their goal is to give data to the Low Order and Reference (LOR) sensor, while the Na-layer LGS launchers are part of the telescope module and the LGS ($\lambda = 589$ nm) provide a Higher Order (HO) correction in comparison to the NGS. The LGS undergoes the same high order perturbation of the target, while the NGS undergoes a slightly different turbulence path. In fact, the LGS are subject to the same vibration occurring in the telescope, which are low order aberrations. Low order modes of aberration are Piston and Tip-Tilt (TT), which respectively influence the wavefront position along the optical axis and the position of the PSF on the focal plane; high order modes are those above the 4th mode and change the shape of the PSF. Each NGS has 2 WFS: a LO-WFS that is a 2x2 Shack-Hartmann (SH), with the goal of measuring 5 modes of aberration (piston, TT, focus, and astigmatism) at $100 - 1000$ Hz and a 10x10 SH reference WFS that measures 60 modes at $0.1 - 10$ Hz. The LGS WFSs are 68×68 sub-aperture SHWFS with a field of view of 16.2" to minimize the truncation errors; the module has focus adjustment and a derotation device to compensate for sodium altitude variations and track telescope pointing elevation. From the FoV of the WFSs, it is understandable that the difference between the FoV of MORFEO and the area in which the correction is applied: the reconstruction of the perturbation is a combination of the turbulence at high order, close to the target, and an approximation of the low order, slightly farther from the target. The control strategy is based on tomographic reconstruction through the Minimum Mean Square Error (MMSE) estimator, Pseudo-Open Loop Control (POLC), split tomography and noise priors and it is implemented in MORFEO RTC. SHWFS[18] are optical components made of an array of lenses, (called lenslets) having the same focal length and focusing on a photon sensor. As shown in fig.2.4, if the wavefront is flat, the SHWFS is uniformly illuminated and each lens focuses the light in an equally spaced pattern, instead if the wavefront is perturbed, the focuses of the lenslet are in a different pattern, from which it is possible to reconstruct the incoming aberrations. For the actuators of the DMs, the design of the Voice Coil Motors (VCM) is composed of a magnet facing a coil mounted on a cold-finger clamped in a cold-plate; in the cold-finger a permanent magnet is installed to provide a restraining force when the system is powered off. On top of the magnets, a reflective membrane (mirror) is glued, so it can be deformed without discontinuities and with ~ 30 nm accuracy. DM1 and DM2 have, respectively, 1026 and 1147 actuators, equally spaced on the mirror's surface and able to perform, respectively, 918 and 1027 available modes for active correction of shape. However, ELT also uses the other 2 mirrors to correct the wavefront: M4 and M5, which are not part of MORFEO, but are located downstream of the primary mirror (M1). M4 is a DM, made of 5316 VCM actuators moving at 1000 Hz frequency, while M5 can be only fast tip-tilted (at 100 Hz). The 4 corrective mirrors have different roles

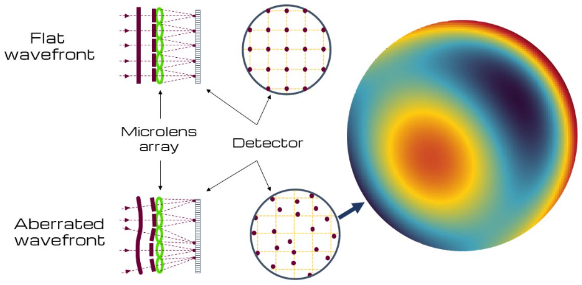

Figure 2.4: Schematic of the SHWFS operation: the wavefront is split by the lenslets and several focuses appear on the detector. Depending on their position, the RTC is able to reconstruct the incoming WF phase and its error. Credits: [18].

and are located in different structures to improve the management and the capability of correction. M4 and M5 are the components of the Woofer-Tweeter dual DMs, hence M4 (Tweeter) is used to compensate the high-frequency-low-amplitude aberrations derived from both law order and high order coming from the ground layer of turbulence. M5 (Woofer) is used to correct the low-frequency-high-amplitude aberrations to stabilize the image at low frequency. The MORFEO post focal DMs are compensators for high order modes, conjugated to higher atmosphere layers at 5 and 12 km.

2.4 Laser Guide Stars Objective

The MORFEO LGS channel is composed of two subsystems: an objective to materialize a monochromatic focal plane, optically conjugated at the sodium layer (the LGSO)[19][20] and the LGS wavefront sensor system (LGS-WFS). The apparent altitude of the Na-LGS, and as a consequence the conjugate altitudes of the LGS-WFS are 84, 100 and 180 km above the entrance pupil. The LGSO, shown in fig.2.5, begins after the dichroic, when the light coming from the 6 LGS, at monochromatic $\lambda = 589$ nm is transmitted into the path, ending in the SH-WFSs. The LGSO is a compact relay objective that reshapes the LGS light for the WFS. It reduces the beam focal number, defined in eq.2.5, from $F/\# = 17.755$ of the main path to $F/\# = 5.025$ of the LGS path

$$F/\# = \frac{f}{D} \tag{2.5}$$

where f is the focal length and D the pupil diameter. As a consequence, it folds the path to fit the instrument, and provides a telecentric, gravity-invariant focus, so that LGS images stay at fixed positions on the focal plane regardless of telescope pointing or sodium layer height; only refocusing is required. In fact, the LGS asterism required by MORFEO is fixed to a angular distance of 45" from the target, and even if the ELT pointing angle varies (Zenith angle $0-60°$), the LGS launchers maintain the LGS asterism on the sodium layer. Thanks to the telecentric beam and the constant F/# delivered by the LGSO, the radial coordinate of the LGS images on the LGSO focal plane does not change, independently of the apparent altitude of the sodium layer. In this way, the LGS module just needs to rotate around its central axis, to compensate for the rotation of the ELT pointing, and to move up and down along the gravity direction to compensate for different Na-layer altitude, in order to correctly refocus at the conjugate distance.

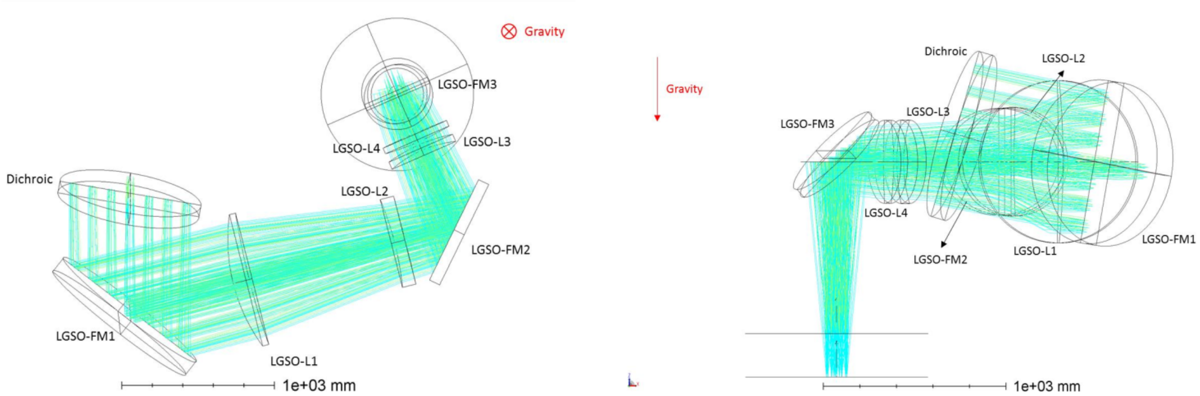

Figure 2.5: Optical path of the LGSO from top-view (left panel) and side-view (right panel). Lenses are named L+number, while the flat, Folding Mirrors are named FM+number. Light enters the LGSO from the dichroic, which reflects the NIR wavelengths and transmits the VIS band, originating from the monochromatic Na-layer LGS. Credits: [19].

The design foresees 4 lenses, plus 3 flat mirrors to fold the beam compatibly with the allowed volume; the specifications of the lenses are summarized in Table 2.2.

Lens	**Thickness [mm]**	**Radii [mm]**	**Diameter [mm]**	**Distance [mm]**
L1	108	+1210.00, −5621.00	838	984
L2	70	−2077.00, ∞	564	890
L3	40	−746.70, +1031.50	436	20
L4	60	+1831.50, +4943.00	434	variable

Table 2.2: Optical parameters of the lenses L1–L4. The thickness is measured at the center of the lens. Since all the lenses are singlets, each is characterized by two surfaces; positive radii denote convex surfaces, negative radii denote concave surfaces, and ∞ indicates a flat surface. The first radius refers to the surface closer to the DIC, while the second refers to the surface closer to the LSO-WFS. The distance is measured between the lens and the following one; the distance between L4 and the LGSO focal plane varies between 1177.84, 1106.60, and 940.38 mm depending on the conjugation altitude.

Every lens is made of coated silica; however, the features of the coating are still under discussion. The required tolerance values for the LGSO lenses are shown in Table 2.3.

Thickness	**Radii**	**Positioning**	**Wedge**	**Refraction index**	**WFE**
1 mm	0.1 / 0.05 %	100 μm	$6 \cdot 10^{-3}$ deg	$5 \cdot 10^{-4}$	50 nm

Table 2.3: Optical tolerances required for the LGSO lenses. All listed values are technical requirements, except the WFE tolerance, which is the performance requirement driving the others.

2.5 MORFEO science cases

The innovative performance of MORFEO, makes it suitable for in-depth analysis and observations of new astrophysical topics for a ground-based telescope. In particular, the MORFEO consortium divided them into 4 categories: IMA - standard imaging; SPEC - standard spectroscopy; IMA/ASTR - imaging with the final goal of high spatial resolution astrometry; IMA/SPEC - combination of imaging and spectroscopy required for some particular science cases [21]. The target of the observations can be summarized in:

- Planetary science
    - This topic is related to the study of the formation mechanism of the Solar Systems, starting from the effect of the proto-star jet launching mechanism and its feedback on the planetary disk. Directly linked to this topic, an argument of observation will be the formation of the proto-planets and the causes that lead to the formation of massive planets, and the relative timescale. Another crucial argument will be the search and chemical characterization of sub-stellar objects (exoplanets and brown dwarfs). Finally, a study of our Solar system minor bodies, like comets and asteroids, is planned; the goal is to study their orbits and shape, both for science and safety reasons, but also their chemical composition, which is an indicator of the early Sun forming cloud chemistry. In any of these study cases, one of the matters of chemical tracking is the search for water and complex organic molecules; the obvious reason is the possibility of finding habitable and stable environments that could host life, since the increase in the complexity of the molecular structure is related to the stability of the habitat.
      These observations require a high angular resolution and a high Strehl ratio. Within distances of ≈ 10 pc, it is expected to recover stellar jets proper motions, hence to study the jet dynamics on very small scales of $\approx 10 - 50$ μas.

- Nearby stellar systems
    - This term indicates the study of the stellar populations within the Milky Way and its satellite galaxies, being a benchmark for developing and testing stellar evolution, population synthesis, and dynamical models. The research activity related to the observation of the nearby stars is mainly focused on the Stellar Formation (SF) in different environments, and on galactic archaeology, which is the discipline used to understand the formation of galaxies. These topics are related, and both are studied using 2 main features of the stellar populations: the kinematic and the chemical composition. In fact, galactic archaeology is based on the theory of hierarchical accretion, which means that bigger structures, like galaxies, are accreted over a long time due to the mergers (capture) of minor structures, like dwarf galaxies or stellar populations. The chemical composition of the population is strongly connected to the environment in which it was formed and can be used to estimate the Star Formation Rate (SFR) and the Initial Mass Function (IMF), which are 2 main features to model the dimension and the features of the birth environment. The easiest time to determine the IMF is early in the life of a stellar cluster, before high-mass stars burn out and dynamical friction segregates masses and lower mass systems are ejected. The kinematics of a population is made of the 2 integrals of motion of the stars, the energy, and the angular momentum (or one of its components), and are

characteristic of the original birthplace of the population. From the combination of kinematic and chemical abundance, compared with the Milky Way ones, we can suggest that a certain group of stars is not native to the galaxy and, hence, accreted. The chemical abundances are studied with the ground-based telescope spectroscopy, while the 3D motion of the stellar flows so far has been mainly studied by space-based astrometry telescopes like the GAIA satellite[22]. ELT will also be used to understand the galactic environment, in order to study the features of the population coming from the densest part of the galaxy (the bulge) and the relatively young stars. Moreover, since both the SFR and the IMF depend on the metallicity, ELT will observe the metal-poor populations, mainly in the galactic halo. So far, only a fraction of their stellar population has been accessible by observational facilities due to the intrinsic faint magnitude of the least massive stars in their main sequence and the prohibitive crowding conditions occurring in the core of these stellar systems, but with the diffraction limited AO correction of MORFEO and the high sensitivity of ELT, these compact and faint objects will become observable. The kinematic is traced from the difference between the position of the stars observed typically at 1 yr distance (measuring the proper motion), and from the redshift, which measures the component of the motion along the observation axis. The typical accuracy required to investigate the internal kinematics of globular clusters is of a few km/s, since this corresponds to the typical velocity dispersion of these systems. What is expected within the limit of ≈ 10 kpc in the nearby universe is to obtain proper motion ≈ 0.10 mas/yr. The performance of MORFEO will provide positional measurements as accurate as 0.05 mas to the astrometric measurements carried out with MICADO; which is a huge improvement with respect to the Hubble Space Telescope (HST) and JWST, that cannot penetrate the inner part of the globular clusters, since their resolution is respectively ≈ 50 mas and ≈ 30 mas.

- Local universe
  - The study of the cluster of galaxies containing the Milky Way is based on the observations of the composition of the structures close to our galaxy. Continuing the chemical archaeology flow, it will be observed the composition of the nearby galaxies (like Virgo) and of the planetary nebula of the nearby globular clusters, in order to expand the knowledge and improve the models about the SFR and the IMF. Another reason is that the dust extinction makes the Milky Way nucleus extremely difficult to observe, hence we need to rely on other galaxies to know how the star formation changes in such a dense, metal-enriched environment, like in the nuclear star cluster, which are groups of star-forming in the inner regions of the galaxies (shown in fig.2.6). Another interesting theme is whether the massive globular clusters are groups of stars formed singularly, in some way that we still do not understand (according to the models, there should exist a mass threshold), or if these structures are what remains of the nucleus of a dwarf galaxy after the outer regions have been tidally stripped away during the merger with a bigger structure. In both cases, these massive globular clusters could be the places in which Intermediate Mass Black Holes (IMBH) are located; however, their existence is still uncertain, as the mechanism of their formation and accretion is. Finally, cosmological studies will be perpetuated in the observation of the Local universe, in particular, about the measurement of the cosmological constant through the measurement of the surface brightness fluctuation of distant supernovae.

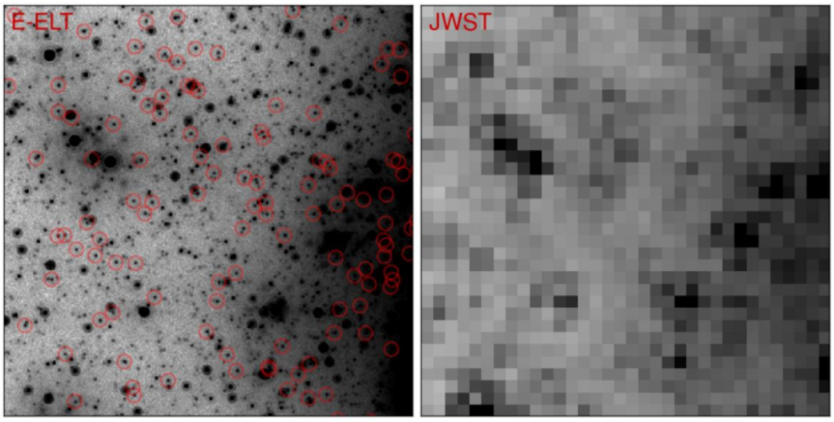

Figure 2.6: Comparison of the simulated observation of the same nuclear star cluster at distance ≈ 2Mpc with ELT+MORFEO and JWST. Credits: [23]

- High redshift universe
  - Finally, the last macro-topics of the MORFEO study cases are related to cosmology, the biggest structures in the universe, and the Active Galactic Nuclei (AGN). The exploration of the distant universe will be performed beginning with the central region of $z \approx 1.5$ galaxies and the detection of the evolution of its stellar mass. It will then proceed with the observation of resolved, lensed galaxies and globular clusters at redshift $z = 2 - 4$, which represent a crucial age for the evolution of the universe: Globular clusters in the early universe are thought to be responsible of the re-ionization. Going even further, ELT will observe the gamma ray bursts coming from still uncertain sources at $z = 6 - 12$ and the Lyman Bright Galaxies at $z > 13$, to improve the knowledge about primordial galaxy formation and evolution. This information is used to confute and test the models about the evolution of the universe, the ΛCDM at first; they represent the proof or refutation of the cosmological models that we have built over the past decades. About the AGN, ELT will be used to observe them in the early universe, to understand the formation and feedback mechanism of the Super Massive Black Holes (SMBHs) and the nearby region. At first, researchers will study the mass of the central black holes, using the velocity of the closest orbiting object as a measurement, later they will model the impact of the warm dust cloud on the evolution of the host galaxy. Finally, BH and SMBH will be studied in their dual configuration (BH+BH or neutron star) and SMBH+SMBH; it is a new frontier of multi-messenger astrophysics and a boost for the understanding of gravitational waves and general relativity theory.

Especially for the Local universe and high redshift universe observations, the sensitivity of ELT and the resolution provided by MORFEO are crucial for the goodness of the samples and the achievement of the purposes. It will be possible to observe extremely faint objects using integrations times of several hours and signal to noise ratio between 3 and 20; the most remarkable magnitudes planned to be observed are: I ≈ 29.5 and J ≈ 28 for extragalactic resolved stellar populations (mainly in Virgo cluster), H ≈ 28 − 29 for primordial galaxy imaging and K ≈ 29 for high redshift galaxies.

Chapter 3

Testing the ghost alignment technique on the lab prototype

3.1 Micro Alignment Telescope

The Micro Alignment Telescope (MAT)[24], shown in fig.3.1, is an extremely accurate instrument, used for several industrial and scientific applications in the alignment field. It is made of a rigid cylindrical support, which holds the inner lens system, an eyepiece, a focus knob, and 2 micro-metric knobs, one for the vertical movement (Y axis), one for horizontal movement (X axis) of the target. The focus knob is unmarked, with the exception of 2 ticks marked 0 and ∞ distant 90° from each other, but it has 160 equidistant grooves that can be used as coarse reference; each groove has a tolerance of ±10%. The focus adjust can be turned 1.75 times, corresponding to a non linear focus response: the first turn changes the focus from 25 mm to ≈ 300 mm, while the remaining 0.75 turn arrive until infinite focus, to observe objects at almost any possible distance (shown in fig.3.2). The MAT is mainly used for industrial applications, in which an auto-collimated reflective surface is located at tens of meters from the instrument, and the operator only needs to find the reflection; in this application, the MAT is set to the proper distance only once and is no longer moved. For this reason, the MAT can also be used for centering purposes, establishing the axis of the system, and moving the target object until it reaches the desired position. The FoV of the MAT depends on the focal length at which the telescope is set, and according to the guide of the MAT, I performed

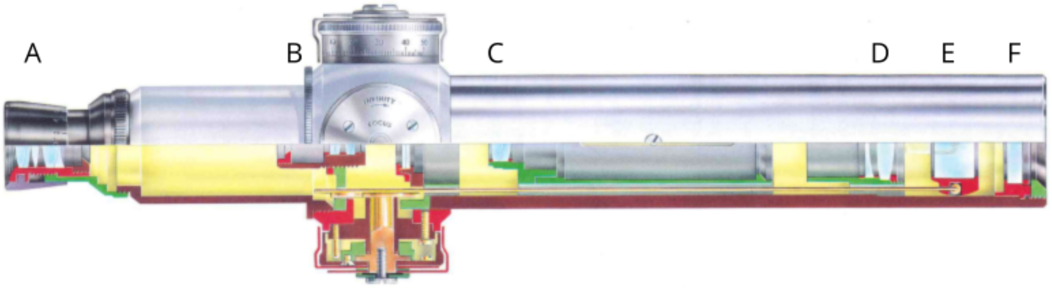

Figure 3.1: Draw of the inside of the MAT. A: eyepiece; B: erector lens; C: focusing lens; D: objective lens; E: micrometer block; E: cover glass. Credits: [25].

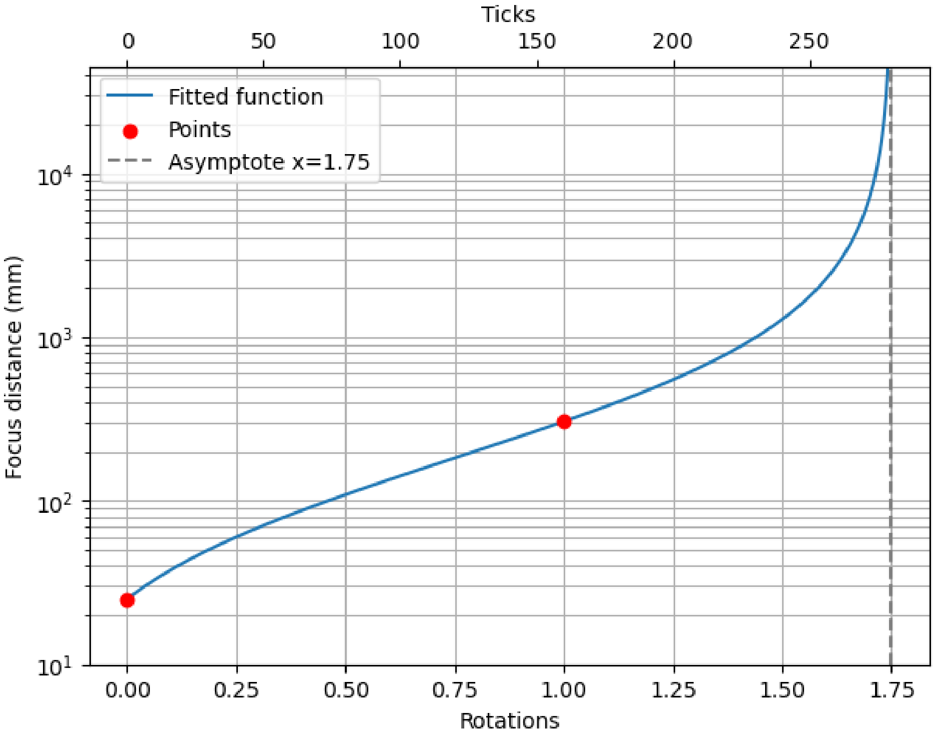

Figure 3.2: Coarse fit of the focal length of the MAT with respect to the rotations of the knob and on the ticks on the knob. The fit has been performed using the data given by the guide of the instrument.

a linear fit on this relation, as shown in fig.3.3 The micrometers drums are graduated at intervals of 0.02 mm, and have maximum range of ±1.2 mm. I used the MAT with its CMOS (Complementary Metal-Oxide-Semiconductor) camera (the other option was an ocular) to have the possibility to capture snapshots and conduct image analysis. I used IDS Paeck Cockpit software to visualize the MAT sight on a computer, to take pictures and perform preliminary analysis (i.e. the saturation of the images).
The MAT can be equipped with a green lamp house that provides the illumination of a milli-metric target (fig.3.4) and projects it on a reflective surface. The circular target serves as a reference scale: the center of the inner circle marks the target position for the object observed with the MAT, and the distance from this point to the object being aligned can be measured precisely.

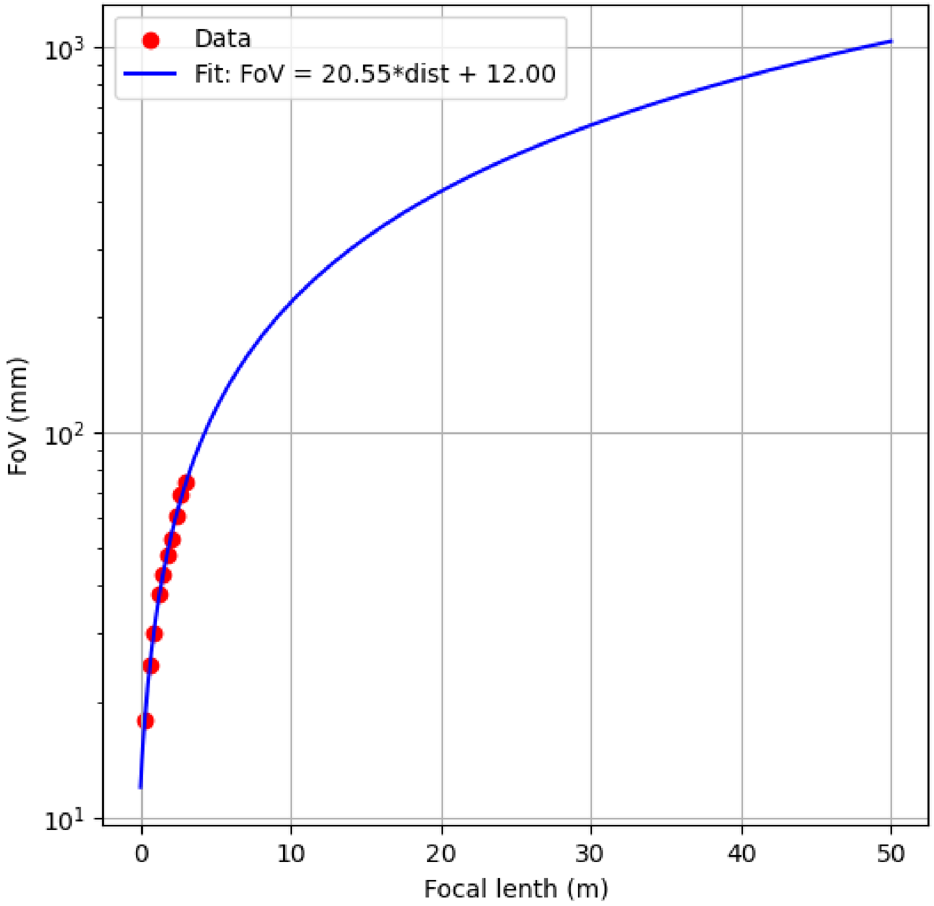

Figure 3.3: Coarse fit of the FoV of the MAT with respect to the rotations of its focal length. The fit has been performed using the data given by the guide of the instrument.

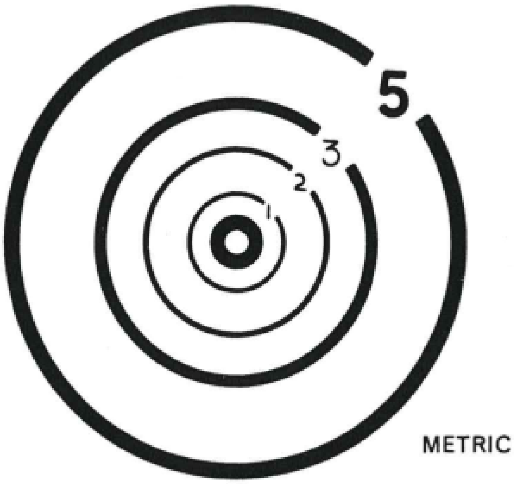

Figure 3.4: Draw of the metric target of the MAT. The numbers represent the diameter of the black circles in mm, calculated in half. The inner, un-numbered circle has an inner diameter of 0.25 mm and an outer diameter of 0.5 mm. Credits: [25].

The MAT has the possibility to insert a laser after the cover glass, in order to conduct a coarse, initial alignment. However, it has an extremely high tilt that makes it unsuitable for the purpose of this experiment. In the next paragraph there will be the explanation of the calibration of the auto-collimated mirror that I used to measure the tilt of the laser, shown in fig.3.5. Following eq.1.1, in the laser case $\Delta x \approx 10^{-2}$ m, while the $L = 3.290$ m (twice the distance between the MAT and an auto-collimated mirror), hence $\Delta\theta > 10'$.

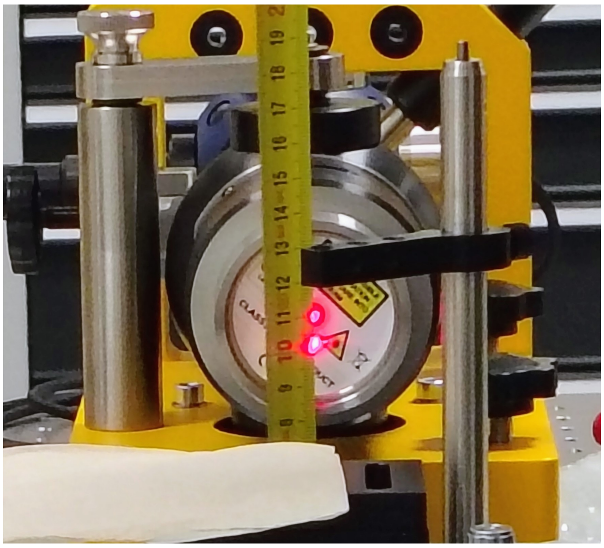

Figure 3.5: Picture of the laser aperture and laser beam after being reflected by the auto-collimation mirror. The upper red spot is the fired laser, while the lower one is the reflected beam; their distance is $\approx$ 10 mm, measured with a meter.

The optical system of the MAT began in correspondence with the mark E in fig.3.1 and on the external part of the instrument there was a screw to indicate the reference of the location. Hence, every distance from the MAT to any other component was calculated from that screw. Every MAT has the same structure and working path, except some slight differences of internal component and performance. During the experiment, I used a metric MAT, produced by Taylor Hobson, identified by the code 112/2582 (metric telescope).

3.2 Lab prototype planning

It was assumed that a white paper was needed to locate the ghost positions along the optical axis, due to the faintness of the ghosts and the difficulty of detecting them in terms of brightness, position, and size. Every reflection implies a factor $\sim 1/20 - 1/100$ for the intensity of the focus of the ghost with respect to the real PSF of the illuminating source. It was expected that a non-aligned lens had focused the ghost far from the optical axis, making it impossible to see with the MAT. Finally, the dimension of the focus (RMS radius, R_{80} or Full Width Half Maximum (FWHM)) was crucial for the identification: a faint beam with a relatively large size was not visible or could be mistaken for background noise, while a faint beam with a relatively small size could be detected. For this reason, the workflow is to simulate some systems in Zemax (fig.1.2), trying different types of lenses and configurations; since usually the ghosts are parasite effects for the observations, shown in (fig.1.1), in the sequential mode there is no specific command on the optimization tool to obtain a system producing 2 or more observable and useful ghosts per lens, so the search is conducted simulation by simulation. Zemax results shows that typically the longer the focal length is, the smaller is the PSF size. In my particular case, I had to impose the physical constraint of ≈ 1.3 m long system, which could not be exceeded. It derived from the portion of the optical table available for the experiment, considering the area occupied by the MAT and other components necessary for the project. I imposed the system not to vignette the light, especially on the frame of the lenses, in order to focus the ghosts with the maximum possible intensity. Initially I simulated some random system in Zemax, to search for suitable ghost; I was using long focal length lenses ($f > 200$ mm), and optimizing the position of the lenses according to the constraints I had. I found out that a $f = 750$ mm lens, positioned 50 mm after the Point-Image-Point (PIP) produces excellent ghosts, but I could not find any other usable lens for the focused and ghosted setup. Thus, I changed my approach and investigated typical optic systems layouts. At the beginning I planned a double $2f$ system made of 2 lenses, L1 and L2, with focal length respectively f_1 and f_2 (fig.3.6a). L1 was located $2f_1$ after the illumination source, the image of L1 was $2f_1$ after the lens, L2 was placed $2f_2$ after it, and finally, the image of the entire system $2f_2$ after L2. I also planned to insert a filter, mounting it approximately halfway between one of the lenses and the image, with the converging rays. Since the available filter was a plane window, it would have ensured a suitable number of useful ghosts, both from single and multiple reflections. However, there is no filter in the LGSO, and any component increased the complexity of the final system, and since it was used only to form the ghosts, I decided not to add it to the system. Moreover the presence of a filter positioned in a converging (but also diverging) beam, would have introduced aberrations, mainly astigmatism due to the wedge, and the refraction with silica would have increased the chromatism on the focus derived from the polychromatic illumination source. The final and definitive setup was a collimated+converging system (fig.3.6b): the first lens (L1) was located at distance f_1 from the source, in order to be a collimator lens, then L2 was placed at distance f_1 from L1 and focusing the ray after distance f_2. I noted that a collimated ray produced better ghosts than the previous system, so I proceeded to replicate it in the laboratory.

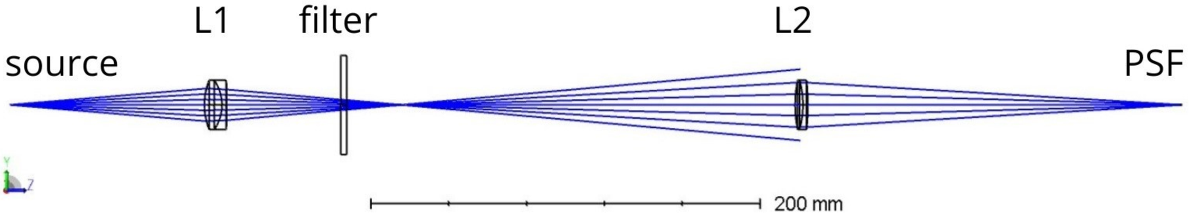

(a)

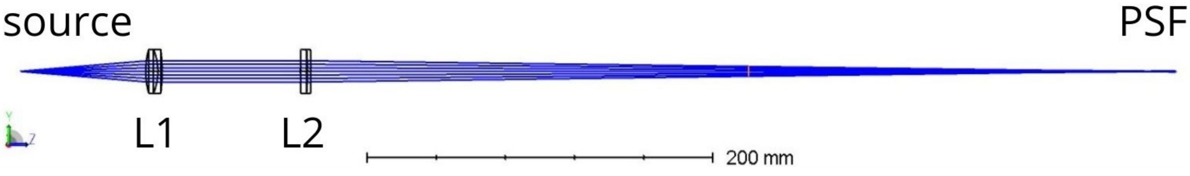

(b)

Figure 3.6: Zemax drawings of (a) firstly proposed setup with $f_1 = 50$ mm lens, filter and $f_2 = 75$ mm lens in 2f configuration; the beam is vignetted at the second lens. (b) Final letup with a $f_1 = 75$ mm focus collimating lens and a $f_2 = 500$ mm.

3.3 Experimental setup

I tested the alignment procedure of the LGSO, for MORFEO consortium, based on the observation of the ghost reflections of the lenses. I built a PIP (a point-like source of polychromatic light) as a source of illumination of the prototype, and I used the MAT to perform the alignment, pointing the camera objective at the targets. Each picture was saved in the format TIFF (Tagged Image File Format), which offers several advantages for research purposes: the preservation of information, the metadata log, and accessibility from different platforms. In fact, I saved the TIFF files without any compression and information loss, using 16-bit image depth for black and white samplings, allowing $2^{16} = 65536$ levels of gray before saturation. TIFF format saved the specification of the cameras at the time of the sample and is compatible with the software that I used, allowing transfers between platforms without any conversion. I used 3 different cameras during the experiment, each one of which was a CMOS camera. The MAT was equipped with a iDS U3-3680XLE Rev.1.2 camera[26] having pixel size $= 2.2\ \mu$m, while the other 2 cameras, which I used to move on the optical table wherever I needed a sample, were an Allied Vision Alvium 1800 U-2050 camera[27] with pixel size $= 2.4\ \mu$m and a FLIR BFS-U3-200S6 camera[26] with pixel size $= 2.4\ \mu$m. The CMOS cameras have an optimal working range $\lambda = 300-700$ nm, hence for my necessities they represented the best trade-off between cost and performance, offering low readout noise, relatively high quantum efficiency also in low light samples, and high speed readout also for high dynamical ranges. I performed error analysis using Python code and AstroimageJ software.

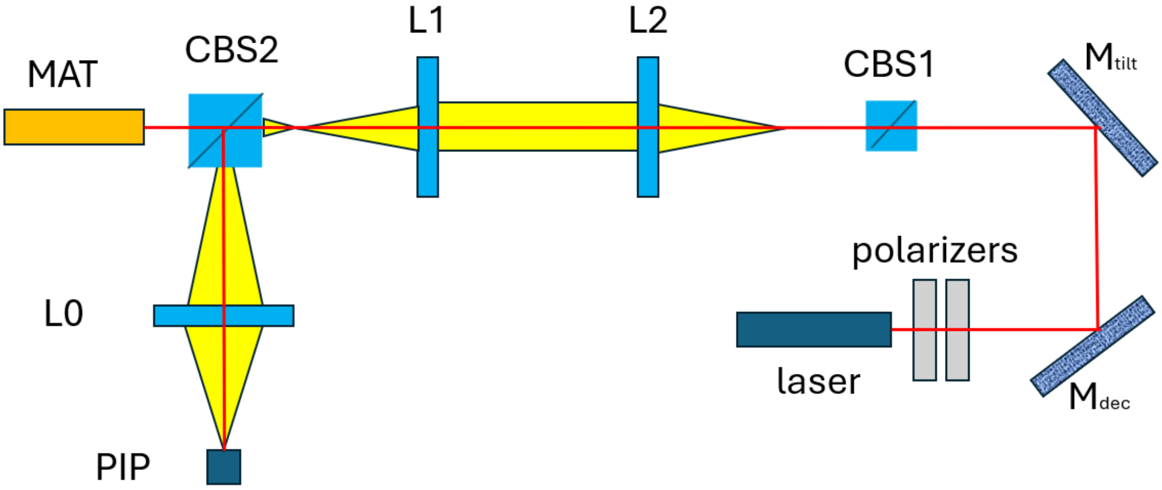

Figure 3.7: Simplified scheme of the setup and the optical components; the yellow beam represents the light originated by the PIP, while the red line represents the laser.

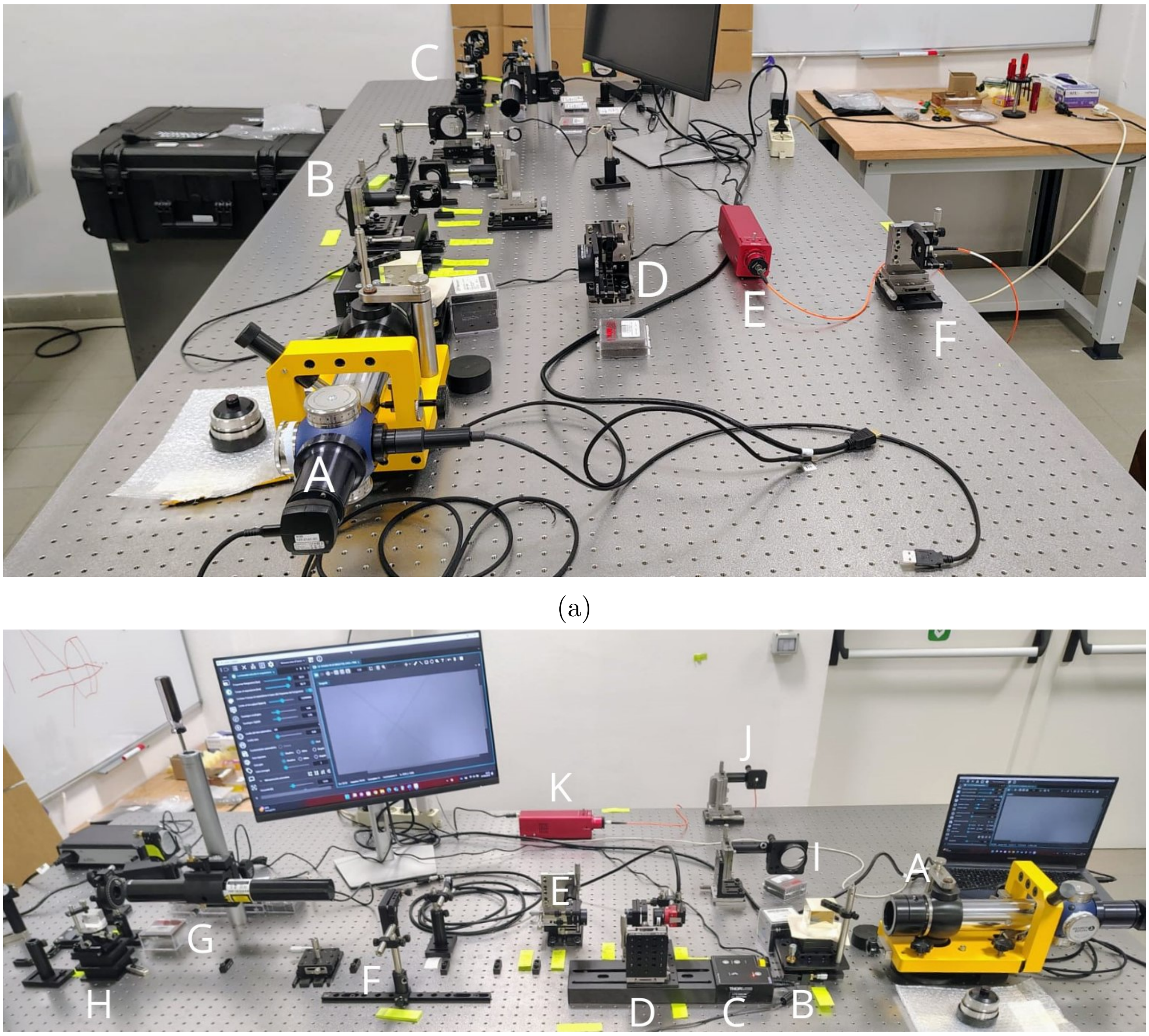

(a)

(b)

Figure 3.8: Photographs of the complete experimental setup. In the picture (a), top-view sight, the components are marked as: A) MAT; B) lens prototype system; C) laser setup; D) L0; E) PIP lamp; F) PIP aperture.
In the picture (b), the side-view sight, the components are marked as: A) MAT; B) CBS2; C) automatic rail; D) L1; E) L2; F) MTF plate; G) laser setup; H) CBS1; I) L0; J) PIP aperture; K) PIP lamp.

The system was made of: the PIP setup, a Cubic Beam Splitter (CBS), the MAT, the effective lenses system, an auto-collimation mirror, and a laser setup. A picture of the setup is fig.3.8, while a simplified scheme of the opics and light paths is fig.3.7. Every double axis decentring support was crafted like the one in fig.3.9a, made of 2 Newport M-SDS65 manual linear stages with 25 mm ride; these supports offer 2 degrees of freedom (d.o.f.) along 2 of the cartesian axes of the setup (fig.3.11a). In every case, one of the d.o.f. was along the gravity axis, so that I could adjust the height of the component; the other d.o.f. was chosen on the basis of necessity because for each component, the position in one of the axes was irrelevant. The lens frames where ThorLabs KM100T - SM1-threaded kinematic mount (or KM200T - SM2 if the lenses were 2-inch instead of 1-inch diameter) are shown in fig.3.9b. Every component was firmly screwed in the holder: in fact, for the lens frames, I often used the lever offered by a metallic screwdriver to secure the lock in the support. Every post-holder had a magnetic base, which guaranteed more stability and protection from involuntary touches, and in turn, it was secured, screwed with a fork, on the table.

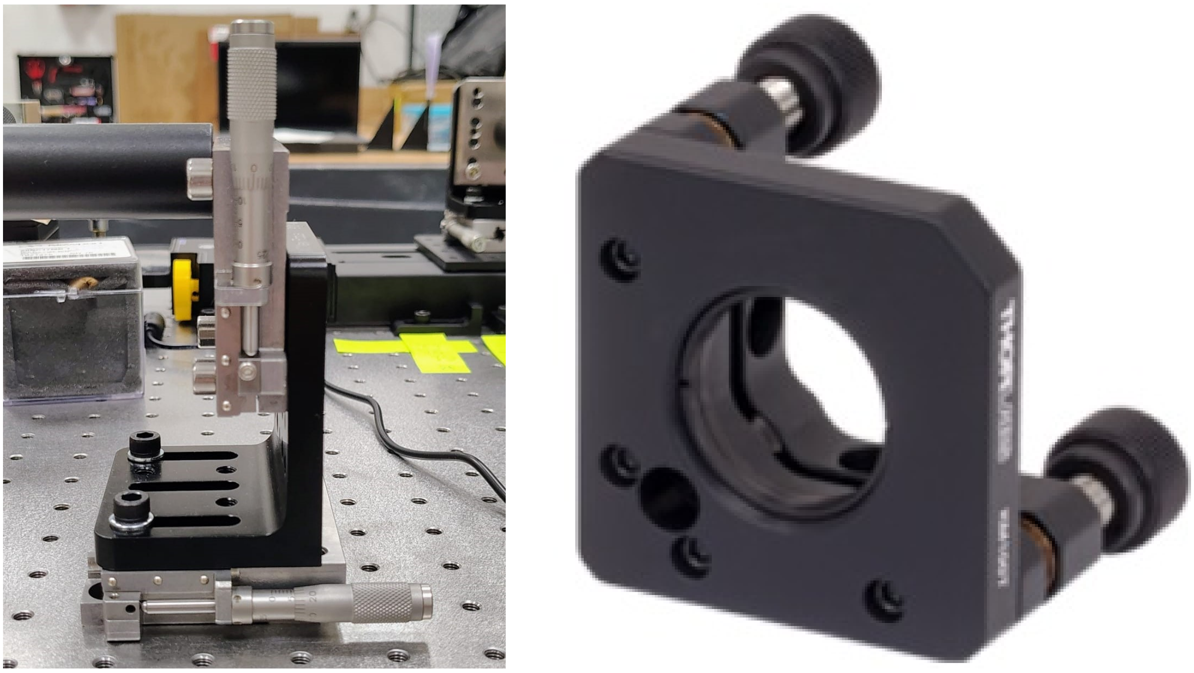

(a) (b)

Figure 3.9: (a) coupled translators to decenter on 2 axes independently. (b) Lens frame to tilt the lens.

3.3.1 Error calculation

The scientifically relevant measurements and calculations that I made were about the misalignment of the optical components, in particular the decenter and the tilt with respect to a target position and axis. In this experiment, the repeatability and the error are different: the repeatability is based on the hardware used and on the ability of the operator, instead the errors depend on the accuracy of the methods used in the Python scripts. In the case of the decenter, which relies on the micro-movement of the translators, the repeatability could be determined in 2 different ways: the accuracy of the translators themselves and the average human eye response. Considering the mechanical component, its sensitivity is 0.02 mm, which is the minimum distance between the ticks of the micrometer. However, the spatial scale of the translator is different from the spatial scale of the camera, so I sampled 9 images of the centroid of the PIP changing the distances of L0 micrometers for each one. For every image, I found the centroid using a Python script and produced the graph shown in fig.3.10. Since it showed a linear correspondence, fitted as $d_{cam} = 281 \cdot d_{tra} + k$, where k is a constant, I calculated the projected sensitivity of the camera as $d_{cam} = 0.02\text{ mm} \cdot 281\text{ px/mm} \cdot 2.2\ \mu\text{m/px} = 12\ \mu\text{m}$. The software I used to visualize the camera output on the computer could zoom the images up to 24 times, so I could clearly observe the separation between the pixels. I suppose that, paying attention after gaining some experience, the visual repeatability of an alignment observed with the MAT could be $\sim 5 - 10$ px, which is consistent with the order of magnitude of the result obtained using the micrometer. A support to this hypothesis is the misalignment of the mirror and the laser, which is explained in the

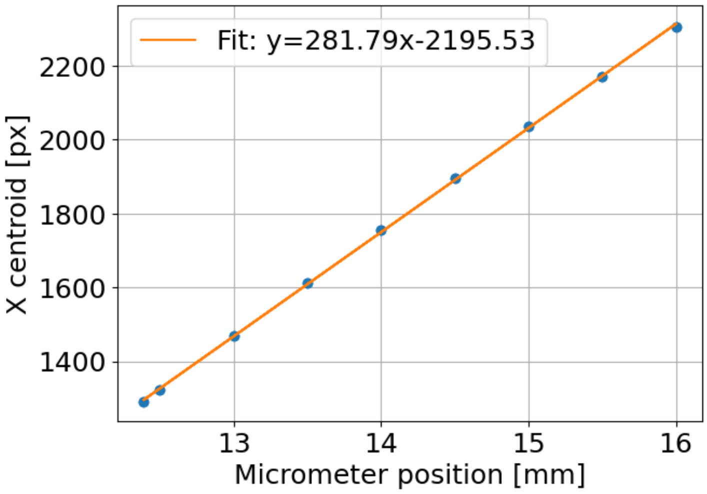

Figure 3.10: Fit of the response of the camera to the movement of the translators.

next chapter, in which all the alignments have been performed by observing the zoomed output of the camera. About the tilt of the frame, it is reasonable to assume that the repeatability of the turn of knob is approximately 1/8 of a full rotation; in the case of the 1 inch frame, 1 turn corresponds to 8 mrad, hence the manual repeatability to 1 mrad $\approx$ 206", which seems overestimated. Referring to my ability in the alignment, I can assume to have performed a tilt operation at the same scale of a decenter operation, so around 10 px = 22 μm, at a maximum distance of 1805 mm, which implies a tilt and a repeatability of $\approx$ 2.5".
I calculated the errors using the method explained in the following paragraph, which had in common the use of a Python code. I calculated the error on the position of the ghosts, summing in quadrature

$$\Delta_{tot} = \sqrt{\sum \Delta_i^2} \tag{3.1}$$

the error of the position on the centroid of the ghost and on the error of the position of the center of the cross of the MAT. I used eq.3.1 because the errors are independent from each other; I applied the standard error propagation to compute the misalignment accuracy of the lenses. Every component of the setup was fixed to an optical table equipped with 4 Gimbal Piston – Air Vibration Isolation System[28], providing an excellent vibration and motion absorption, which allowed the neglect of vibration errors. A summary of the the sensitivity is shown in tab.3.1

Operation	**Instrument**	**Sensitivity**
Decenter	micro-meter	10-20 μm
Tilt	knob	2.5"

Table 3.1: Visual sensitivity of the instrumentation for tilt and decenter operations.

3.3.2 References

As general nomenclature, positioning an observer on the side of the table to observe into the MAT, I will refer to the X axis as the one of the side of the table, positive in the right verse, to the Z axis as the line of sight of the MAT, positive toward the system of lenses, and the Y axis as the gravity one, positive in toward the roof, as shown in fig.3.11a. Referring to fig.3.11b, the angles set by a straight line (black line) in the Cartesian plane are Ψ and φ. Ψ is between the projection of the line and the Z axis on the YZ plane, while φ refers to the angle between the projection of the line and the Z axis on the XZ plane. I will denote Ψ by θ_y, which is considered positive when, at infinity, the distance between a point on the line and the Z axis is $y = +\infty$. Similarly, I will denote φ by θ_x, which is considered positive when, at infinity, the distance between a point on the line and the Z axis is $x = +\infty$

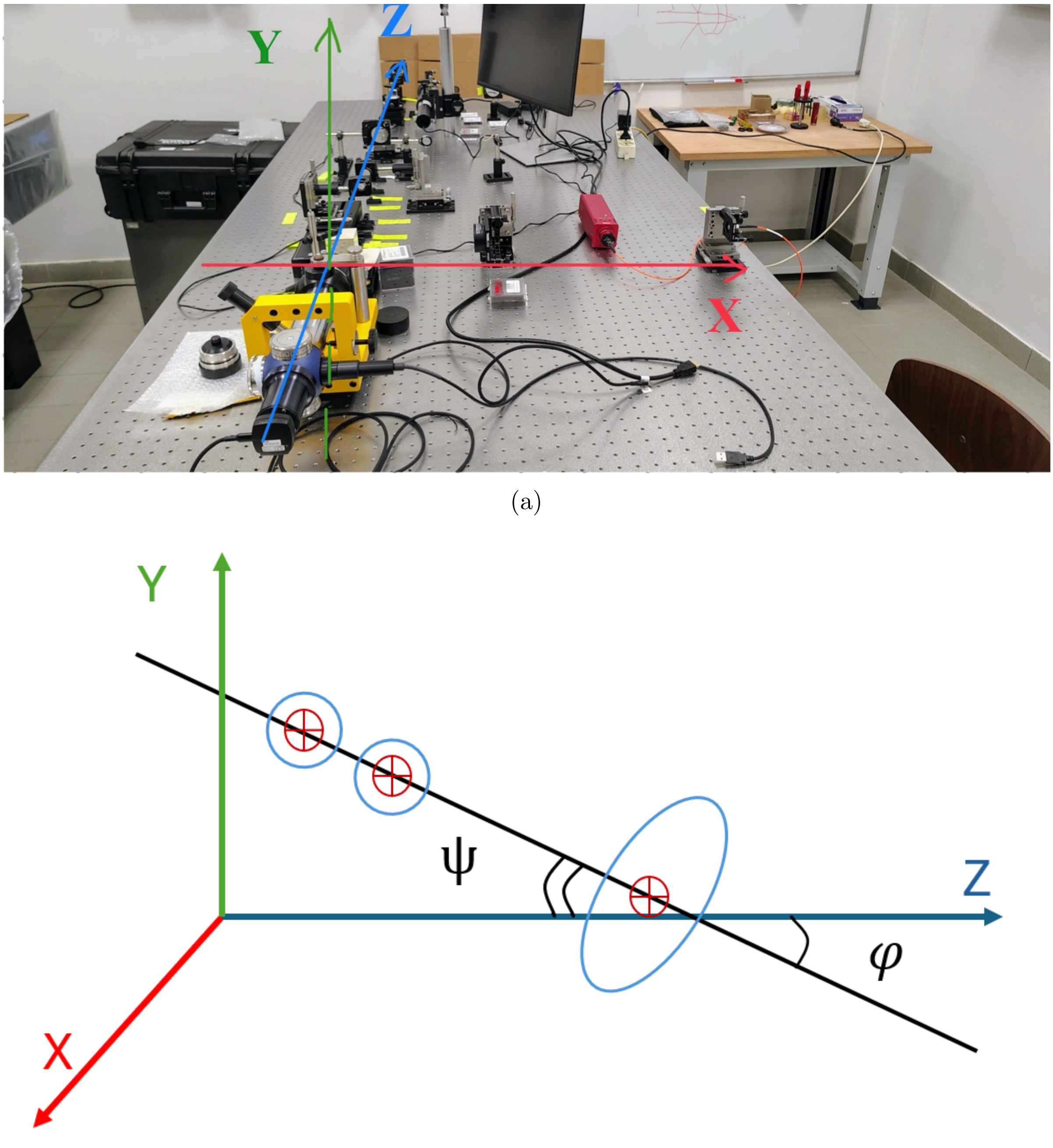

(a)

(b)

Figure 3.11: Laboratory setup with the reference axes; the arrows indicate the positive directions. (b) Definition of the angles between the projection on the aligned axis and the Cartesian axes. The cyan circles represent the ghosts of the lens (the oblate, cyan shape), and the red crosses represent their centroids.

During the conducted with the MAT, I used to vary the focus position along the Z axis,

whose origin is defined at the beginning of the lens array, and I used to observe the XY plane, for which I set the origin on the center of the reference; for the Y axis, the positive verse is opposite gravity and for the X axis is the verse on the right of the MAT, like in the 3D space.
The MAT was already screwed and fixed to the optical table, following the hole of the table in straight line along the Z axis, close to its edge to increase the usable portion of space; moreover it had a clamp to lock it in the stablest way to its mechanical support and the table, thus I assumed that the references axes did not aried during the trial.

Crosshair of the MAT

The reference, target position was the cross of the MAT (fig.3.12a), an internal reference that helps for the calibration and the measures. Since the cross is a few pixels thick, I found its center using different Python scripts, performing 3 different operations: finding the barycenter of the black pixels, fitting the profile of the cross, and finding the intersection of the two arms of the cross. For the first two methods, I cleaned the image by removing the background, cropped the image around the center of the cross, and applied the methods. The image cleaning consisted of the background subtraction of the median value (less sensitive to local variation than the mean), deleted pixels further than 3σ RMS from the average of the bordering ones, and removed of negative pixels; the crop operation, performed in a 20×20 px square visually centered with the cross, was necessary to impose a restricted area of acceptability of the results. Finally, the barycenter of the black pixels and the 1D Gaussian fit were obtained both on X and Y axis. The third technique was based on the assumption of straight arms and on the minimization of the errors due to the long lever of the arms. The arms were tracked looking for pixels with a gray scale level below 0.1% of the maximum, which means the blackest ones, thus the actual central line of the arms. From eye-observation and error analysis considerations, the method of the intersection between the fit of the arms seemed more accurate (fig.3.13), so I decided to take it as a constant reference, assuming it did not change during the time of the experiment. I ran the code a few times and the result was always the same, so I calculated the error of the center position using a Python code that firstly calculated the errors on each fit and after propagated the errors on their intersection, which resulted ± 0.36 px $= \pm 0.8$ μm. Anyway, all three methods differ up to 4.0 μm (fig.3.12b), thus can be considered reliable. The Python scripts mirror the images along the center of the Y axis; however, since this is valid for all the pictures and all the scripts, the effect was null. In order to keep the reference of the axis constant, for every calculation involving the Y axis, I used a factor of -1 to compensate for the mirroring of the images.

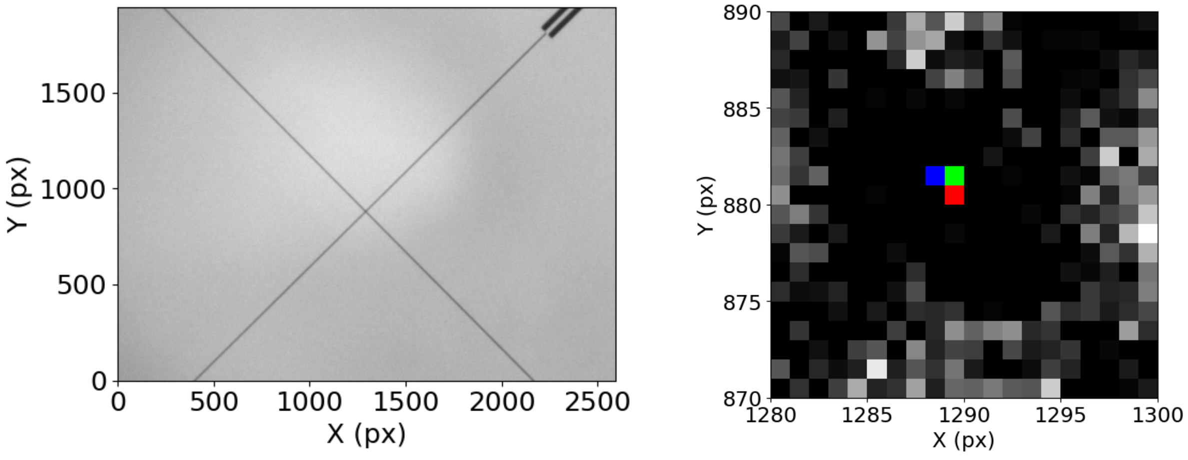

(a) (b)

Figure 3.12: a) Original image of the cross-shaped reference of the MAT. b) Cropped image of the center of the cross, the blue pixel represents the pixel of the center found with 1D fit, the red one is found with the barycenter of the black pixels, the green one is found with the intersection of the fits of the arms.

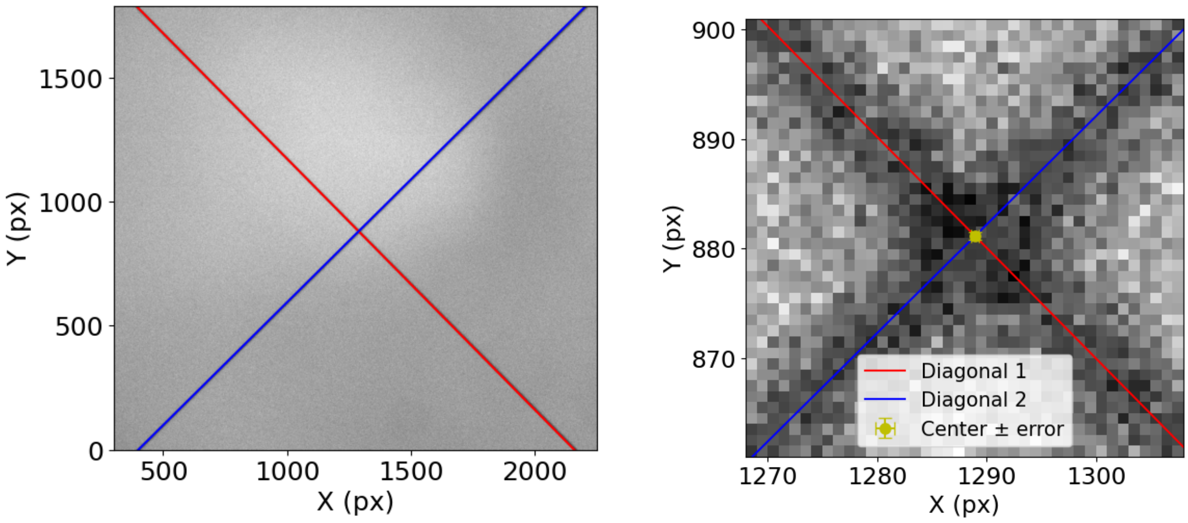

(a) (b)

Figure 3.13: (a) Fit of the diagonal arms of the cross reference of the MAT; (b) center of the cross of the MAT and relative error found using the intersection of the fit diagonals.

Autocollimated mirror

After that, I imposed the MAT in auto-collimation with a flat, 2-inch, $\lambda/10$ mirror (M0), located at the opposite part of the table with respect to the MAT. The distance between M0 and the MAT was $d_{MAT-M0} = 1645 \pm 1$ mm. In the auto-collimation case, the guide of the MAT suggests calculating the misalignment error using the micrometer drum and the metric target; however, I worked in a case in which I could move the mirror in the 3 spatial axes and tilt it, to locate M0 in the best position for auto-collimation.

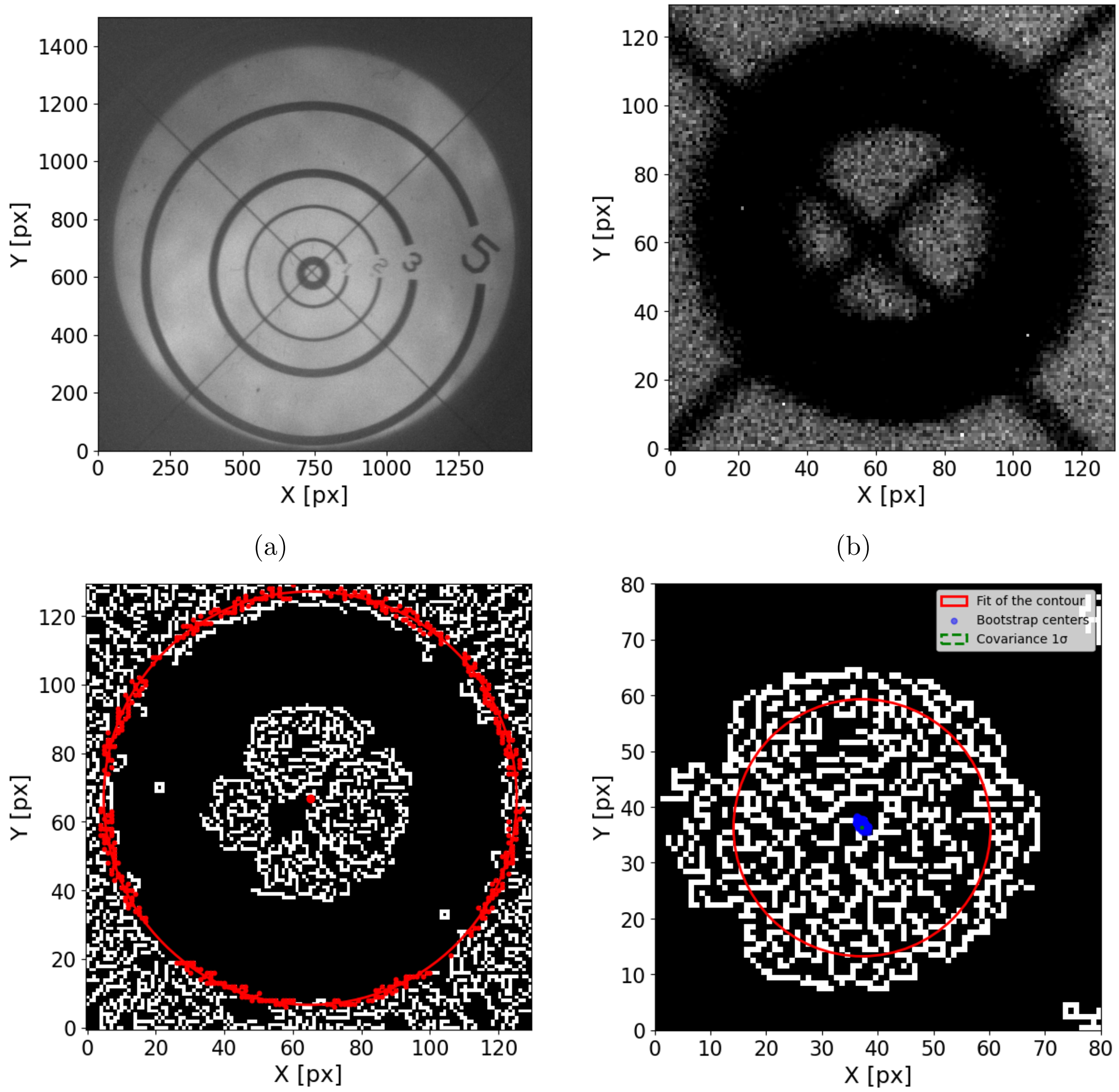

(a) (b)

(c) (d)

Figure 3.14: a) Full image of the target reflected in the auto-collimated mirror. b) Cropped and cleaned image of the center of the target. c) Fit of the external contour of the circle. d) Zoom and fit of the inner contour of the circle and the relative error obtained by the bootstrap method.

Hence, the smallest micro-movement of the knob was too high and the error calculation relied on the eq.1.1. I measured the error of auto-collimation of M0, switching on the lamp house to project the target on the mirror to find the spatial difference between its center and the center of the cross. I wrote a Python script that loaded the image of the target (fig.3.14a), cleaned it in the same way as the cross-center research, and cropped the image close to the region of interest (fig.3.14b). Then, it found the contours of the circles in order to mitigate the effect of the parasite cross (the reference of the MAT, impossible to remove) and finally fitted both the inner (fig.3.14c) and outer (fig.3.14d) circles, finding their centers. The difference between the positions of the 2 centers was 3.10 px = 6.82 μm. However, I considered the center position found with the internal circle fit as more accurate, since the fit was closer to the actual borders and, being a smaller target, it was less prone to image distortion. Initially, the error was calculated with 1σ confidence level of the fit, but I noticed that, running the code several times, the results were different in ≈ 1.2 px range and the error was only ± 0.3 px. As a consequence, I changed the method of search, using the Bootstrap method; it consisted of conducting a statistical analysis on the search for the center of the fit, performed 1000 times. I chose the mean of the center positions as the most likely value and final result, then I used the covariance of 1σ for the uncertainty, resulting $\sigma_x \approx \sigma_y \sim 0.4\text{px} = 0.9\mu\text{m}$.

Laser

The final reference that I used was a red 632.8 nm central wavelength laser, produced by ThorLabs[29]. At first, I tried to align the laser using 2 Cubic Beam Splitters (CBS), making it reflect in M0 back to the MAT, however this technique was introducing many errors, given by the misalignment of the components, and introduced a higher level of difficulty for the building of the system. After having positioned the 2-inch CBS, I aligned the laser using 2 alignment mirrors to reflect the beam in the center of the MAT. The distance between the MAT and the laser aperture was $d_{MAT-laser} = 2205 \pm 2$ mm, divided in $d_{MAT-M_{tilt}} = 1805 \pm 1$ mm, $d_{M_{tilt}-M_{dec}} = 130 \pm 1$ mm and $d_{M_{dec}-laser} = 270 \pm$ mm (the reference laser setup is shown in fig.3.15c). I assumed the 3 measures and corresponding errors were independent, so I calculated the error on the total distance as the sum in quadrature. The mirror closer to the aperture was used for decentering, while the farther one was used for tilt alignment due to its optical lever. The observable of the decenter was the centroid of the laser spot with respect to the cross reference, while the observable of the tilt was the appearance of the Newton rings produced by the interference of the laser with the lenses inside the MAT. In this case, Newton rings originate when the laser is close to the null-tilt condition with respect to the MAT, because the lenses of the MAT inevitably exhibit some imperfections, which generate the interference pattern. The tilt is considered null if the Newton rings are round-shaped, concentric to the laser spot, and uniformly illuminated. These observables suffered the error introduced by crossing the CBS, although I aligned the laser using the cross of the MAT as reference. The laser system was equipped with 2 polarizers, since the laser was not polarized, in order to decrease its intensity and not to cover other sources of lights: one was a fixed polarizer and the other one was variable. However, the presence of polarizers introduce aberrations and also moves the laser beam when the variable polarizer is turned, hence I left it in a constant position and put the other one on a magnetic support, so I could take it on and off always in the same position. I performed the laser alignment with both polarizers mounted and without turning the knob of the variable one. The Python script to find the center of the laser worked in the same way as the one used for the centering of the mirror in auto-collimated, assuming the most likely value as the mean of the results found with a 1000 iteration Bootstrap method and the error as 1σ of covariance. The resulted uncertainties were $\sigma_x = 0.75$ px and $\sigma_y = 0.56$ px. I could not use the M0 reference and the laser reference simultaneously, because M0 was positioned in a way that blocked the laser beam: I screwed a guide to the table to be able to insert and remove M0 and its support. Performing a visual repeatability test, inserting and removing M0 several times, and observing the reflected target of the MAT, I concluded that the mechanical guide ensured the position of M0 in a constant location. The results of the aforementioned analysis of the reference are resumed in tab.3.2 and tab.3.3.

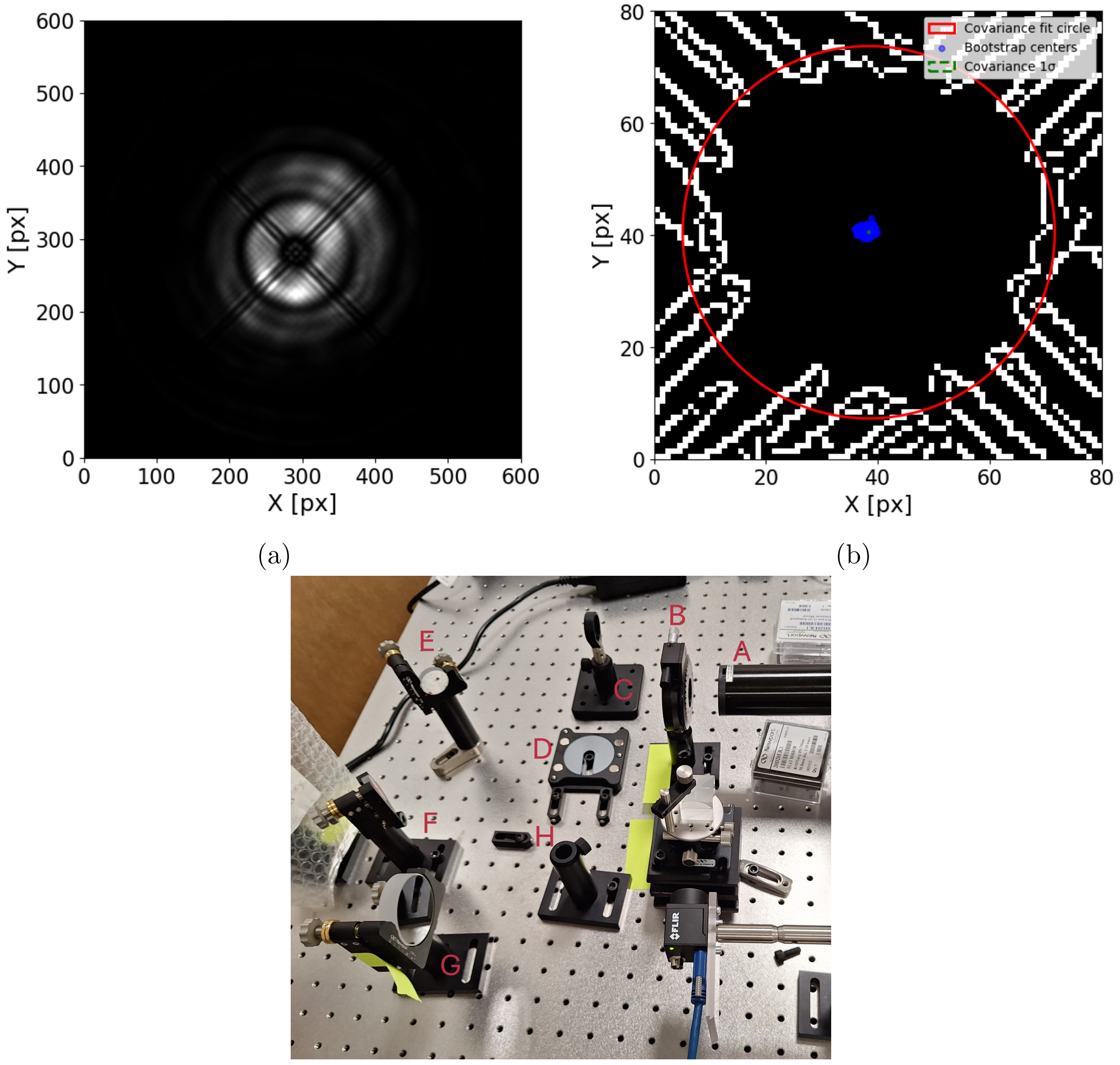

(a)

(b)

(c)

Figure 3.15: a) Full image of the laser beam seen using the MAT. b) Fit of the contours of the laser spot, center and relative error calculated using the Bootstrap method. c) Setup of the laser (A), with variable polarizer (B), fixed polarizer (C), and its magnetic base (D), decentering mirror (E), tilting mirror (F), and M0 (G). In the auto-collimation of M0, the mirror is positioned in (H), occluding the laser.

Target	**Method**	Δx (μm)	Δy (μm)	L **(mm)**	$\Delta\theta_x$ **(")**	$\Delta\theta_y$ **(")**
Cross	Fit intersection	0	0	0	n.a	n.a
Cross	Pixels barycenter	0.7	3.3	0	n.a	n.a
Cross	1D gaussian fit	-1.5	1.2	0	n.a.	n.a
M0	External fit	13.1	-16.7	1645	1.6	-2.1
M0	Bootstrap	18.0	-12.3	1645	2.3	-1.5
Laser	Bootstrap	-1.8	1.1	2205	-0.2	0.1

Table 3.2: Preliminary analysis of the position of the references. For every component of the reference of the method used to locate its center, the distance from the target position, the distance from the MAT and the misalignment.

Target	**Method**	Δx (μm)	Δy (μm)	L **(mm)**	$\Delta\theta_x$ (")	$\Delta\theta_y$ (")
Cross	Intersection	0.0 ± 0.8	0.0 ± 0.8	0	n.a	n.a
M0	Bootstrap	18 ± 1	-12 ± 1	1645 ± 1	2.3 ± 0.1	-1.5 ± 0.1
Laser	Bootstrap	-2 ± 2	1 ± 1	2205 ± 1	-0.2 ± 0.2	0.1 ± 0.1

Table 3.3: In-depth analysis of the used references, relative errors and misalignment with respect to the high-precision reference of the cross of the MAT.

The residual tilt shown in Table 3.2 and 3.3 have been calculated using eq.1.1, in which Δx was the distance between the observed position of the references and the crosshair of the MAT, and L was the distance between the references and the MAT.

3.3.3 PIP setup

Two arms setup

The illumination of the system could not be provided by a source located between the MAT and the prototype lens system because it would have introduced visibility issues. If the hardware of the source were located on the optical axis, it would have partially blocked the sight of the MAT; while if it were off-axis, the illumination would have been tilted. I planned to build a system with 2 arms (fig.3.11a), in a way that the light coming from the source along the X axis could be directed in the MAT arm (along Z axis). To do so, the first optical component that I introduced in the system was the 2-inch non-polarizing CBS (CBS2)[30], mounted on a rotative, tilt-adjustable support.

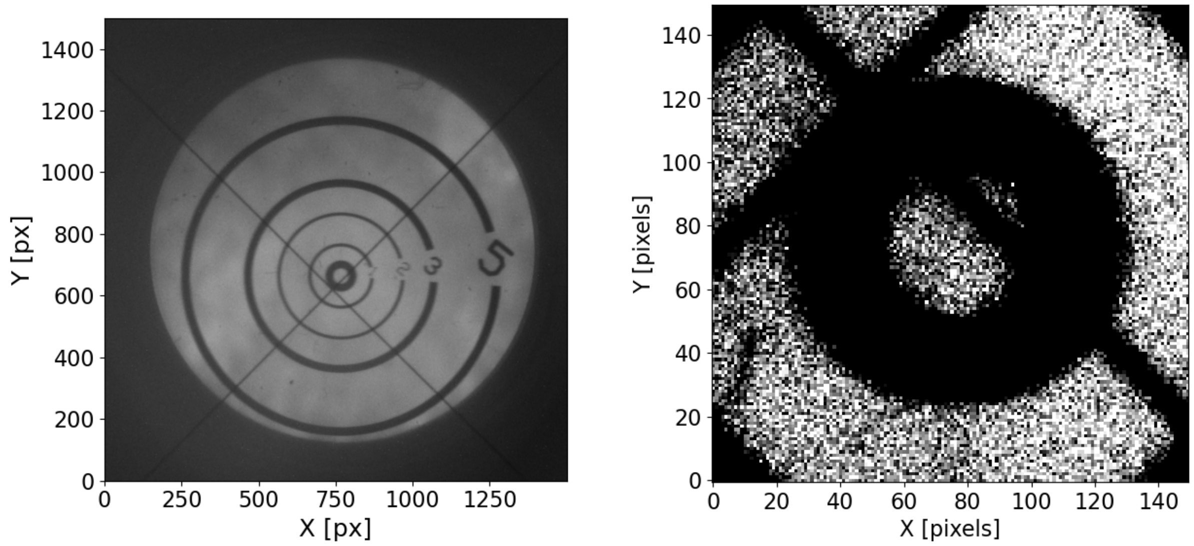

(a) (b)

Figure 3.16: a) Full image of the target reflected on M0 viewed from the MAT. b) Cropped image of the central region, in order to calculate the misalignment (mirrored upside-down by the Python code).

I aligned the CBS2 using a level to set its faces as parallel as possible to the optical table, then I aligned the remaining 2 directions using the MAT laser as an instrument for the coarse alignment and the side of the CBS2 itself as a reference for the fine adjustment. The goal of the laser was to adjust the CBS2 so that both the transmitted and reflected beams were as collimated with the table as possible. I used 2 reference targets, positioned and marked before the insertion of the CBS2 and neglected the tilt of the laser, since I only needed a rough alignment. The fine alignment, instead, was based on the observation of the glass surface of the CBS2, and the procedure was to rotate it to make the interference fringes visible on both the closer and further side, changing the focus of the MAT. I calculated the misalignment introduced by the CBS2, looking at the reflection of the target on M0, shown in fig.3.16, using the formula 1.1. To calculate the CBS2 alignment residual error, I could not use the Python script wrote for the same purpose of M0, because the shadow of the cross was impeding a correct operation and a sub-pixel accuracy, hence I considered the visual approximation of $\Delta x = 0.5$ mm and $L = 1645$ mm. I divided the obtained result by 2, since the CBS2 was crossed twice. The estimated total wedge of the sides was $\Delta\theta \approx 1'$, which was better than the $5'$ declared by the constructor.

Illumination source

I needed the illumination to be provided by a point-like source. I could not use the lamp house of the MAT, because of its large aperture and wide divergence; I could not use a laser because of its large aperture (1 mm) and because its monochromatic wavelength, which would have caused interference between the beam and the optical components. In addition, I tested a setup similar to the one that will be used for the LGSO alignment, which will not use a laser due the large spot on the LGSO lenses originated by the divergence. I chose to build a PIP (fig.3.17b), which is a system able to simulate a polychromatic point-like source. The PIP setup was made of a halogen lamp and an M122L01 ThorLabs glass optical fiber with diameter = 200 μm [31], located in the axis normal to the optical axis, on the right of the MAT and directed in the Z axis by the CBS2. I used a 200 μm optic fiber because it was the best trade-off between the simplicity of its alignment and the performance required for the experiment. The Tungsten-Halogen Light Source [32] is produced by ThorLabs and has an emitting range of $360 - 2600$ nm. I did not equip the lamp with any filters to keep the power unchanged. Light was collected into the optical fiber, which terminated on a support that could be tip-tilted, mounted on 2 translators that could be decentered on the Y and Z axes. Since the beam was diverging, I introduced a focusing achromatic doublet $f = 250$ mm lens between the PIP and CBS2 to focus the PIP after the CBS2, re-imaging the fiber head, projecting the light-source along the optical axis of the MAT. Moreover, the position of the lens prevented vignetting both on the lens itself and on the CBS2, in order to transmit all the light from the lamp, without any loss. This lens (L0)[33], was also mounted on a tip-tilt support, mounted on 2D Y and Z translators. L0 was distant ≈ 475 mm from the fiber aperture and ≈ 245 mm from the right side CBS2, and focused the PIP ≈ 475 mm after the MAT, ≈ 250 mm after the second surface of the CBS2 along the Z axis.

PIP alignment

For the coarse alignment of L0 and the fiber, I used the reference laser. At first I injected light into the PIP optical fiber, removing the other end from the lamp and pointing it at a piece of white paper, decentering the frame to find the position in which the laser brightness was maximum (fig.3.17a). Later, I coarsely aligned the lens decentering it in order to make the laser cross the center of L0 and point to the fiber head, in the same way as before; I set the center of L0 and the PIP aperture at the same height. I also used a white paper sheet with a small hole to make the ray pass and observe the back-reflection of the lens, setting it centered with the hole. This second method is based on the reflection of the glass, which causes the formation of a diverging reflected beam; if the lens is aligned, it is concentric to the original laser. It is essentially the same technique as the ghost alignment, but the beam diverges instead of converging, and the expected error on the alignment is higher. The error on the ghost is smaller because the beam on which to find the centroid is compact and relatively luminous, whereas the error on the back-reflection is higher because the beam on which to find the centroid is fainter and orders of magnitude bigger. The photon budget of the 2 methods is the same, since both the reflections originate from the same surface.

I finely aligned the PIP system using the cross of the MAT as a reference, centering the 2 foci of the PIP in the cross. The close focus (f_c) was the one 475 ± 1 mm after the MAT (it was the focus of the PIP after L0), while the far focus (f_f) was at 2815 ± 1 mm after the MAT. I found out that f_f was in the same position as f_c; the only difference was that it was seen by the other verse of the Z axis, thanks to the reflection of M0; they both were a re-imaging of the PIP. For the fine alignment, I used the near focus as a reference for the decenter, while the far focus as a reference for the tilt; this means that I centered the close focus using the micrometers of the translators, and the far focus using the tilt knobs of the lens frames, operating similarly to what I did for the reference laser. In fact, typically the close reference is more sensitive to the decenter, while the far reference to the tilt (due to the optical lever). However, there were two issues: the focus positions were insensitive to the tilt of the PIP, and there were 2 different components to move, the PIP and L0. It is understandable that, since the PIP is a point-like source, a small angular deviation did not change the outgoing light direction, so I set the PIP frame as perpendicular as possible to the table using a mechanical, straight tool, and then I used the tilt of L0 for the alignment. About the decenter procedure, I moved half of the PIP translators micrometers and half of L0 translators micrometers, essentially keeping the center of L0 and the PIP aperture at the same height. In an iterative process, I shifted back and forth between the positions of the foci using the MAT and positioned the foci themselves in the center of the cross using the chosen method; every time I centered the focus, the other one was off-axis but repeating the correct technique with the exact reference, the amplitude of the offset decreased time by time. Finally, after about 10 iterations, I found the best achievable position for both the foci, corresponding to the situation in which both the images were visually aligned.

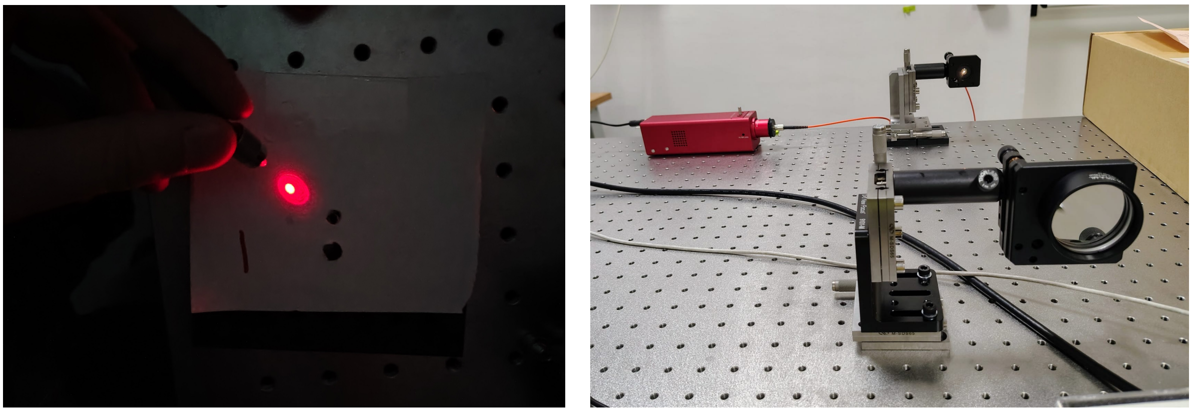

(a) (b)

Figure 3.17: (a) Method of the coarse alignment, in which the laser is injected in one head of the fiber and exits from the other one. (b) PIP setup, made of the halogen lamp, the fiber mounted in the frame and L0.

PIP alignment error

After finding the best trade-off between the position of the 2 foci, I saved a snapshot of them and written a Python script to calculate the alignment residual error. In particular, the code operates in the following step (shown in fig.3.18):

- Initially, the script loads the image, and find the non-isolated, maximum intensity (I_{peak}) pixel. The requirement of a non-isolated pixel is due to the possibility to have broken pixel, marking a single, high luminosity pixel. After that, the code crops the Region Of Interest (ROI) centering the most luminous pixel in the center of a 256 × 256 px square, in which is located the entire PSF of the PIP.

- The following step is necessary to erase the effect of shadowing caused by the cross of the MAT. The PSF has a Gaussian profile, while the cross has an "X" profile; the scrip performs a Fourier Transform (FFT) of the ROI because the Gaussian profile is invariant for FFT, hence the PSF is unchanged, while the cross can be erased. To do so, a mask shaped as the profile of the portion of the ROI in which the intensity $\mathrm{I} > \mathrm{I_{peak}}/\mathrm{e}^2$ is applied on the PSF, and whatever is out of the mask is erased. Finally, the code performs the inverse Fourier Transform (FFT^{-1}) to give in output the filtered Gaussian profile PSF.

- Finally the Gaussian is fit with 1D and 2D methods. The 1D fit is performed on both X and Y axis in the same method: the pixel grid is expressed by the matrix

  $$\begin{bmatrix} (x_1, y_1) & (x_2, y_1) & \cdots & (x_n, y_1) \\ (x_1, y_2) & (x_2, y_2) & \cdots & (x_n, y_2) \\ \vdots & \vdots & \ddots & \vdots \\ (x_1, y_n) & (x_2, y_n) & \cdots & (x_n, y_n) \end{bmatrix}$$

  where each element corresponds to a pixel position in the image, and each of them has a photon count. The 1D profile along the X axis is obtained by integrated intensity along the row corresponding to c_k:

  $$C_k = \sum_{i=1}^{n} c(x_k, y_l) \tag{3.2}$$

The 1D profile along the Y axis is performed in the same way, but the counts are along y_l. The fit minimizes the residuals ($r_i = y_{data,i} - y_{model,i}$) and for every parameter p, the Jacobian matrix is computed as:

$$J_{ij} = \frac{\partial f(x_i, \mathrm{p})}{\partial p_j} \tag{3.3}$$

where $f(x_i, \mathrm{p})$ is the model prediction. The covariance of p is calculated as:

$$\mathrm{Cov}(\mathrm{p}) = (J^T J)^{-1}\sigma^2 \tag{3.4}$$

where σ is the variance of the residuals. The 1σ uncertainty for each parameter p_i is given by:

$$\sigma_{p_i} = \sqrt{\mathrm{Cov}(\mathrm{p})_{ii}} \tag{3.5}$$

The 2D Gaussian is performed with the residual minimization method, so the error is calculated in the same way. The difference between the 1D and 2D fit, is that the 1D is an approximation of the 2D fit, so I expected that it provided larger errors and less accuracy.

The error calculated as 1σ uncertainty on the 1D fit was ~ 0.12 px $= 0.3$ μm, whereas on the 2D fit was ~ 0.01 px $= 0.02$ μm. I calculated the error as 1σ tolerance, because after running several times and noticing that the values of both the fit and the associated error were unchanged, I assumed the chosen tolerance was enough. The results of the alignment of the close focus are shown in fig.3.18 and in tab.3.4, The results of the alignment of the far focus are shown in Table 3.4

Target	**Gaussian fit**	Δx (μm)	Δy (μm)	**L (mm)**
Close focus	1D	4.3 ± 0.8	14.0 ± 0.8	475 ± 1
Close focus	2D	4.1 ± 0.8	14.8 ± 0.8	475 ± 1
Far focus	1D	12.0 ± 0.9	-10.2 ± 0.9	2815 ± 1
Far focus	2D	13.4 ± 0.8	-11.5 ± 0.8	2815 ± 1

Table 3.4: Table of the different methods to find the center of the PIP, for both close and far foci, for different methods of fitting, and the distance from the cross reference on the X and Y axis. The errors on the fit are measured as 1σ uncertainty of the fit, while the errors on the decenter are calculated as the sum in quadrature between the error of the fit and the error of the cross of the MAT.

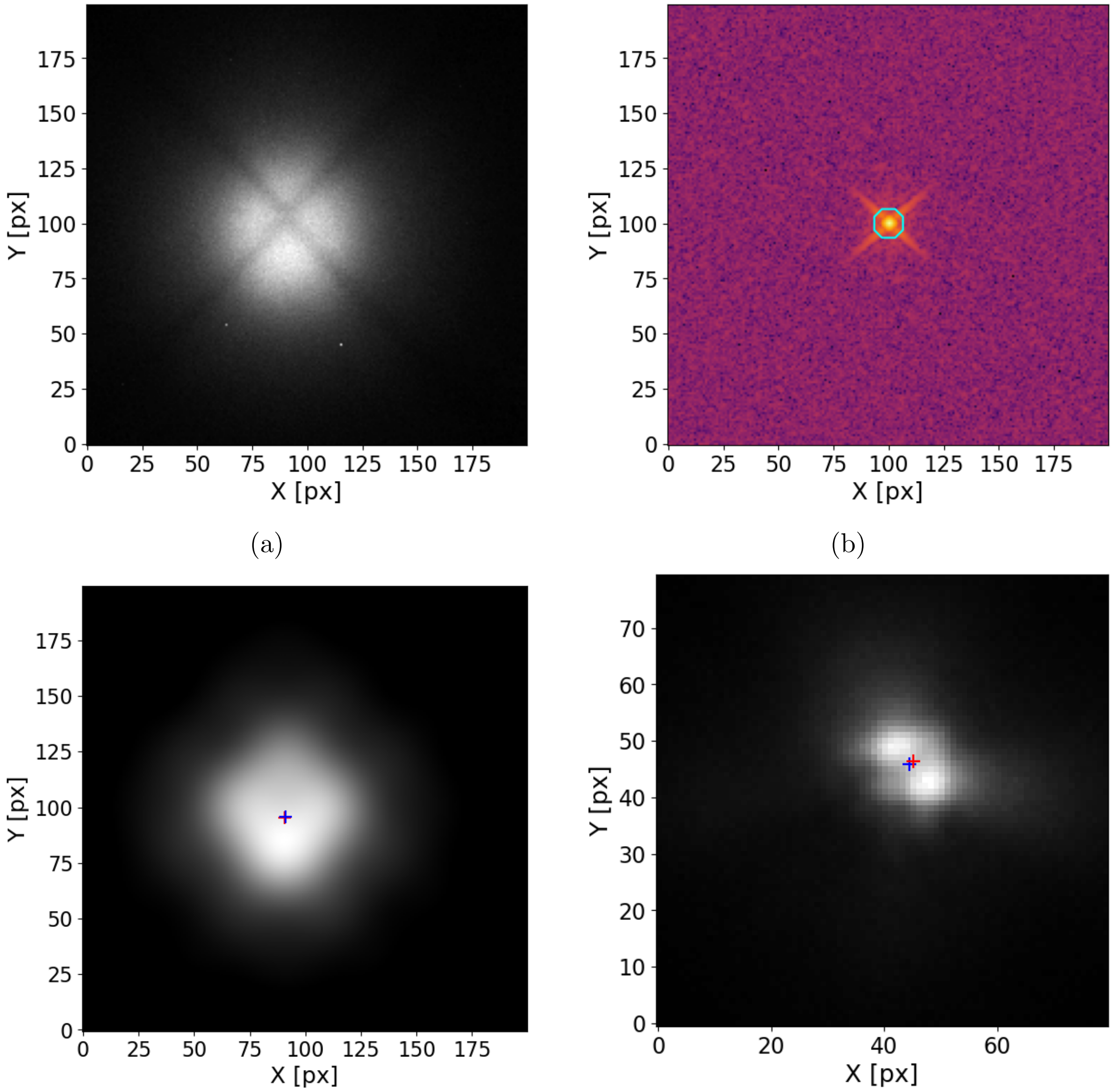

(a) (b) (c) (d)

Figure 3.18: The images in this mosaic are cropped in frames smaller than 256 px for clarity purpose. a) PSF othe PIP cropped around the luminosity peak pixe; the cross of the MAT is shadowing the PSF. b) FFT of the image and (cyan) mask; counts map is in log scale. c) Result of the 1D fit (blue) and 2D fit (red) applied on the FFT^{-1} of the filtered PSF of the close focus. d) Result of the 1D fit (blue) and 2D fit (red) applied on the original image of the far focus (the method did not change).

I calculated the decenter as f_c one and the tilt as the angle between f_c and f_f using eq.1.1, where the $L = (2815 - 475)$ mm $= 2340$ mm, which is the distance between the foci, and Δx and Δy are the difference in the x and y positions of the foci. Finally, the PIP residual error is:

- Decenter:
  - X axis: 4.1 ± 0.8 μm
  - Y axis: 14.8 ± 0.8 μm
- Tilt

- X axis: 0.8 ± 0.1”
- Y axis: -2.3 ± 0.1”

Since I used the PIP as a point-like source of illumination and it was separated from the rest of the setup, the decenter should be its effective error (error of the PIP image, which was the projection on the aperture in the close focus). The tilt, instead, referred to the angular distance from the close and far focuses of the PIP, but should not influence the error. However, since the point-like source was formed by the convergence of a beam from the optical fiber and subsequently diverged with the same angle, the tilt corresponded to the offset angle of inclination. In order to simulate the system in Zemax, I calculated the Numerical Aperture (NA) of the PIP system (PIP+L0) using the equation

$$NA = \frac{1}{2 \cdot F/\#} \tag{3.6}$$

I found the F/# using eq.2.5, applied when the beam was projected at a distance f from the focus and had a diameter D. I measured $f = 20.6 \pm 0.1$ mm using a caliper, and measured $D = 3.41 \pm 0.03$ mm using a CMOS camera with pixel size $= 2.4$ μm (considering an error of 10 px). I calculated $F/\# = 6.0 \pm 0.1$.

3.3.4 L1 alignment

XY plane alignment

I chose the collimator lens, L1[34], to be a $f = 75$ mm achromatic doublet (shown in fig.3.34), which was the longest focal length lens to avoid vignetting. At the beginning, I aligned it purely by eye at a distance from the PIP focus ≈ 75 mm. I observed L1 using the MAT and, varying the focus, I found 2 well-visible ghosts and 1 smaller and fainter. There were also many parasite reflections, probably caused by the CBS2 and the lens, but the ghosts were recognizable by moving L1. I tested the reproducibility of the trial, assuming an extremely lucky first-sight alignment; however, simply inserting the lens apparently in the correct position, even without using a mechanical guide to put it normal to the table, the 2 main ghosts were always in the FoV of the MAT. The possibility of observing the ghosts just with a visual lens alignment was also valid for other lenses that I used as collimators during the several trials I conducted. I proceeded with the alignment, taking as references the bright ghost closer to the MAT (L1-G1) and the bright ghost farther from the MAT (L1-G3). I used the faint ghost (L1-G2) as an additional indicator, but never as a reference, due the difficulty in its characterization; from the MAT FoV it appeared to be in the middle of L1-G1 and L1-G3, but considering the Zemax simulation it was the farther one from the MAT. L1-G1 and L1-G3 were visible in a relatively wide range of focus points; however, I referred to them as closer and farther, indicating the position of their best focus. L1 was mounted on a tip-tilt frame, mounted on 2 translators: one for X-axis micro-movement and one for Y-axis micro-movement. It was all settled on a computerized stage, to be able to move in the Z axis direction; however, I let it steady, for the moment. Initially, I used L1-G1 as an indicator for the decenter and L1-G3 as an indicator for the tilt, but an alignment trade-off was difficult to find, because L1-G1 was almost insensitive to the decenter. So, I changed strategy and assigned the tilt to L1-G1 and the decenter to L1-G3: using these references, I was able to align L1 in about $10 - 15$ min, after ten iterations.

Collimation

The next step was to verify that L1 was actually a collimating lens, because I finely aligned L1 only on the XY plane, but only approximately along the Z axis, which was the crucial one for the collimation; in fact, the MAT is insensitive to the Z axis and can perform alignment only on the XY plane. The collimation process had to take place after the alignment on the XY plane, because otherwise the lens could appear not collimated due to its tilt, and not its position. I used a rudimentary hole mask (fig.3.19), located ≈ 80 mm after L1, made of an opaque adhesive tape stripe (with 3 holes) mounted on a frame, to let light pass only through the holes. I was forced to adopt this solution because the available hole masks were too big for the support, or the holes were too distant. The holes were disposed at the vertices of a triangle, having a side approximately twice as big as the other one; the goal was to have the possibility to choose the longer distance if both the holes were seen by the camera, or the shorter one in the opposite case. To verify the error and acceptability of the collimation, I used a CMOS camera located in 2 fixed reference locations along the Z axis, in which 2 mechanical references marked their position, distant ≈ 150 mm from each other. L1 was positioned on a ThorLabs 300 mm range Linear Translation Stage with Integrated Controller, Stepper Motor rail[35]. The procedure was to iteratively sample the distance between the holes projection in the 2 reference positions, shown in fig.3.20, until they were almost the same, achieving a satisfying accuracy of the collimation. I used the AstroImageJ tool capable of detecting the centroids of 2 sources and computing their radial distance; at the beginning the distances differed by $> 1'$ and I was moving the stage on the rail by 500 μm each time, but after a few iterations, when the difference was $< 0.1'$, I started moving the automatic stage by $50 - 100$ μm each time. I found the best collimating position with an alignment error found by the difference between the radial distances in the reference points; $\Delta\theta = 5.550' - 5.551' = 0.06"$ of diverging beam.

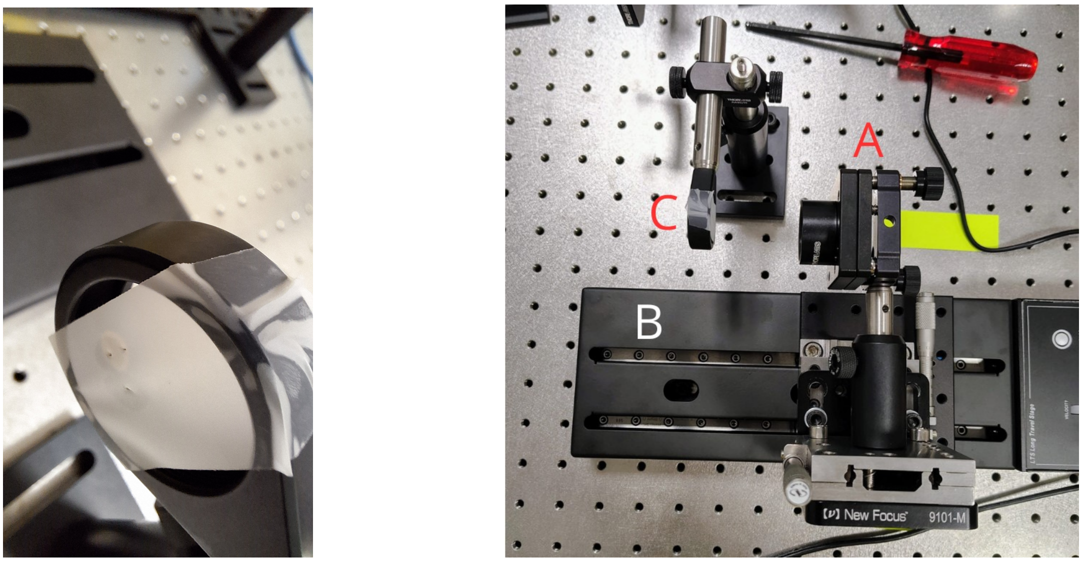

(a) (b)

Figure 3.19: (a) Hole mask. (b) L1 (A) mounted on a rail (B), facing the hole mask (C).

Best focus position of the PIP

I calculated the distance between the PIP focus and the first surface of L1, conducting a sweep in focus of the image of the PIP. I removed L1 and mounted a CMOS camera on a micro-metric translator and sampled the PIP in the distance range $73.0 - 78.0$ mm from the aligned position of L1 at 0.1 mm steps and a dark (background) image. I developed a Python script that analyzed the images, performing the sweep in focus and the search for the R_{80}. The sweep consists of a series of images starting from a pre-focus position, gradually reaching focus, and then moving to a post-focus position. It illustrates the variation of the PSF size of a luminous source: large when out of focus, minimal at best focus, and increasing again beyond focus. R_{80} is a measure of the PSF size, in particular is the radius that contains 80% of the photons (energy) of the Encircled Energy (EE) beam; in a diffraction-limited PSF, it nearly corresponds to the Airy disk. The procedure of the search of the EE is shown in fig.3.22. I measured R_{80} by developing a Python code that cleaned the image of the beam, cropped it, and found the energy of the spot with respect to the background. The image cleaning was the weighted background subtraction, conducted by the removal of a dark image from the analyzed image rescaled to the exposure time of the samplings of the PIP: the TIFF format can be used as a photon count, if the exposure time is known, so the used formula was (eq.3.7).

$$I_{clean} = I_{raw} - I_{background} \cdot \frac{t_{exp}^{image}}{t_{exp}^{background}} \tag{3.7}$$

The image was cropped around the ROI, paying attention to include some background (an annulus of $5 - 10$ px thickness outside the PSF) to have a comparison between the PSF and the dark; finally the script found the centroid of the ghost with a 2D fit and performed the search of R_{80} around the centroid. Initially, the script found the most luminous pixel and used its position as a first guess of the centroid of the PSF; it then performed a 2D Gaussian fit of the PSF to find a more accurate centroid and, from it, calculated the normalized EE and the R_{80}. The 2D Gaussian fit was associated with an uncertainty well below the sensitivity of the micro-meters. I estimated the background error as the statistical standard error of the mean of the dark image, expressed in eq.3.8, in which σ_{px} is the uncertainty of the photon on each pixel and then performed the dark subtraction using the background value $\pm\ \sigma_{\text{bg}}$.

$$\sigma_{\text{bg}} = \frac{\sigma_{\text{px}}}{\sqrt{N}} \tag{3.8}$$

Indeed, the relative uncertainty of the R_{80} was negligible with respect to the relative error of the position on the components. I identified the error on R_{80} by repeating the search while varying the background within its uncertainty, resulting in a negligible uncertainty of only $\sim 0.004\ \mu$m. I plotted R_{80} as a function of the distance from L1 and fitted the curve using a parabolic fit to determine its minimum (fig.3.21), which corresponds to the dimension of the beam at the distance between the focused image of the PIP and the first surface of L1.

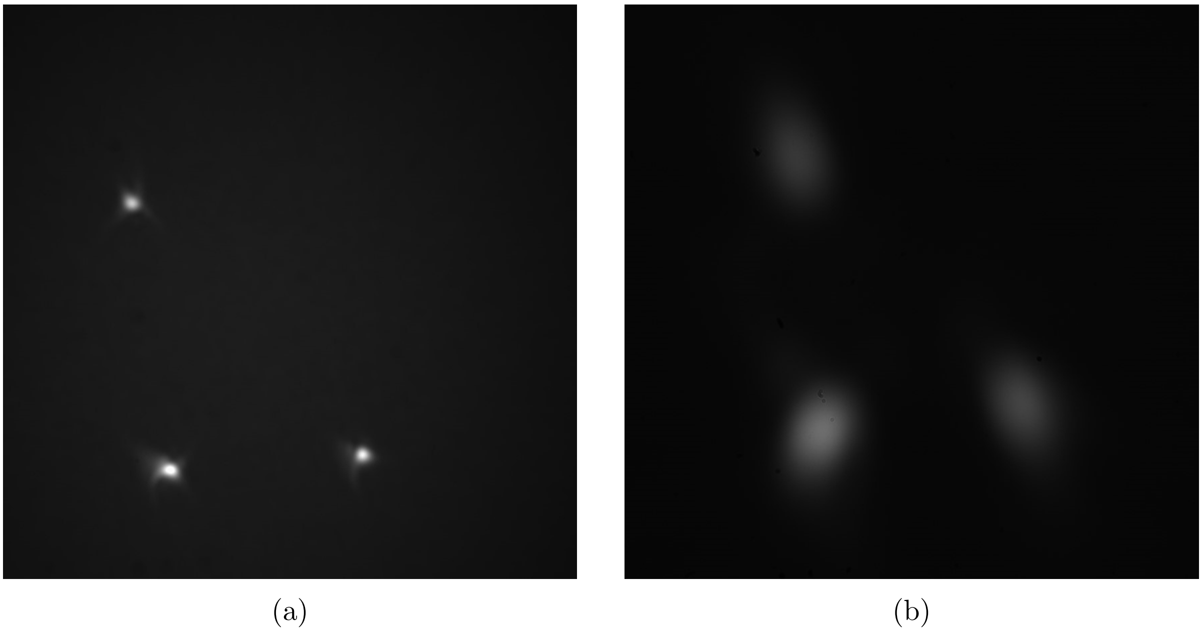
(a) (b)

Figure 3.20: Collimation procedure: (a) light passing through the holes seen in the close reference, (b) light passing through the holes seen in the far reference.

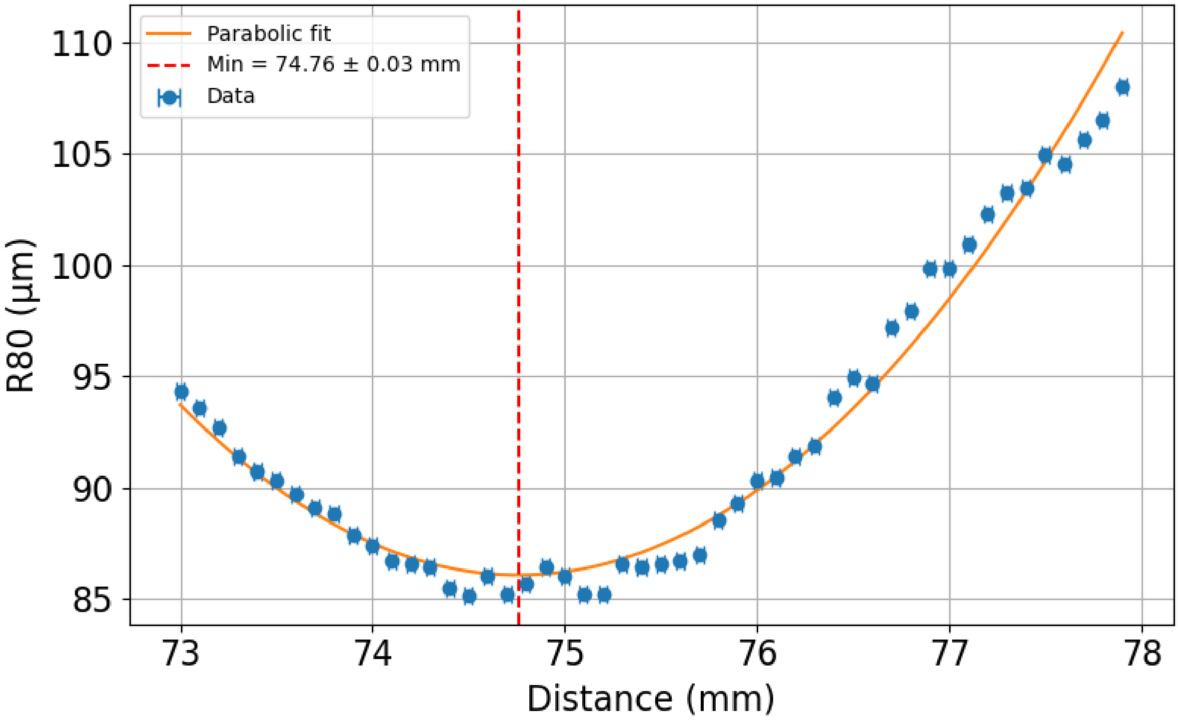

Figure 3.21: R_{80} of the image of the PIP vs its distance from the first surface of L1.

Assuming a collimated beam, since the divergence of 0.06" is negligible, the sweep in focus reported that the distance between L1 and the focus of image of the PIP was 74.76 ± 0.03 mm.

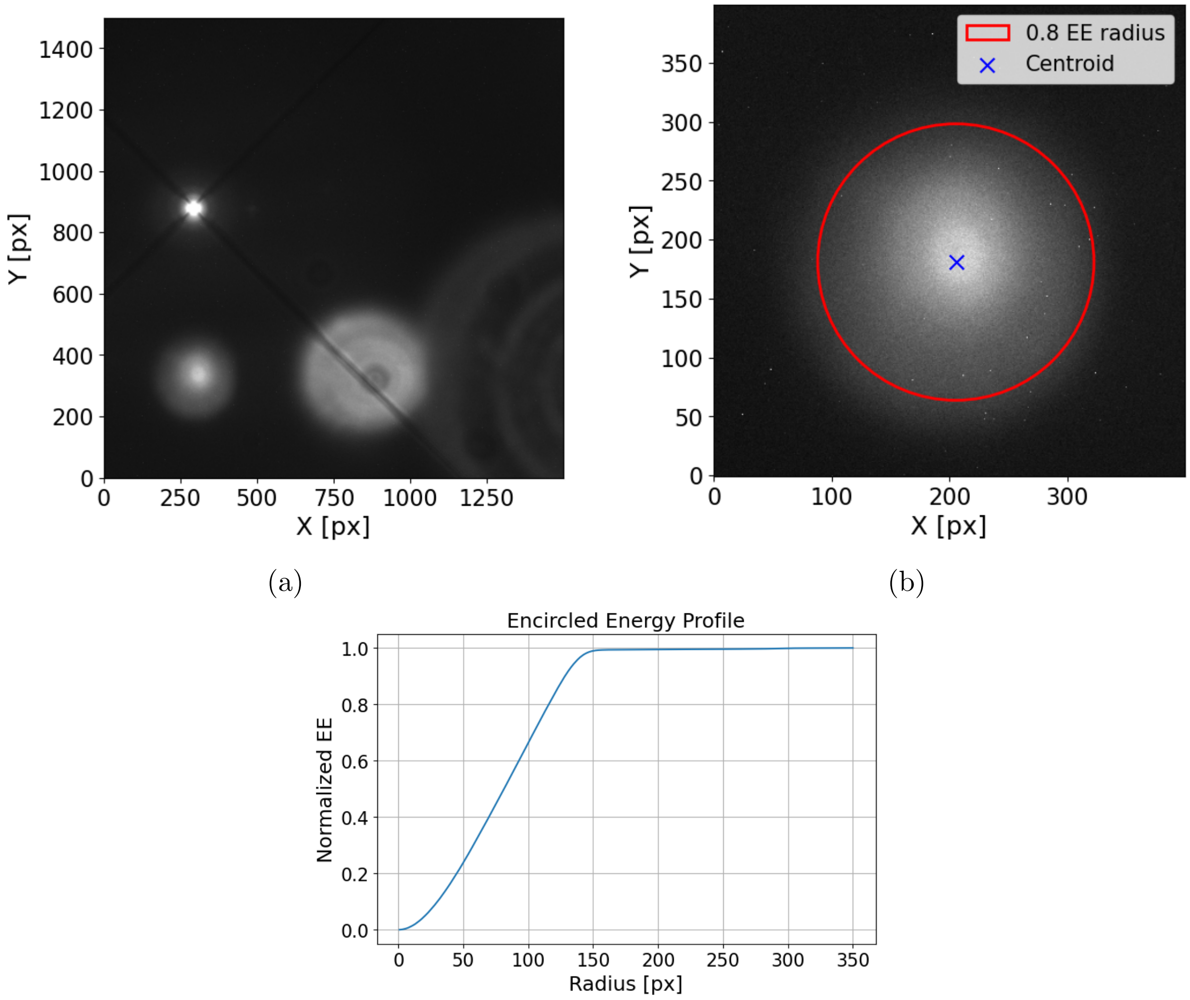

(a) (b)

(c)

Figure 3.22: Sweep procedure: (a) original image; the separation between the PSF and other light sources is crucial, otherwise the R_{80} and best focus position would be incorrect. (b) Cropped and background subtracted image, the centroid is found using 2D fit of the beam (blue cross) and the R_{80} (red circle) is found using a photon count. (c) Normalized EE profile.

3.3.5 Ghost characterization and alignment residual of L1

For locating the axial position of L1-G1 and L1-G3, I performed a sweep in focus of the 3 ghosts, to find the best focus position of each of them and estimate the alignment residual error of L1. I found R_{80} (fig.3.22) using the same Python script used for the sweep in focus of the PIP. The minimum of the parabola corresponds to the best focus position and the minimum PSF size. I tried to sample the ghosts when they were aligned at the center of the cross, but it was pretty difficult to perform a background subtraction, eventually leading to an error in the R_{80} computation. Hence, I used the micrometers of the MAT to decenter the ghosts and be able to observe them separately (fig.3.23); since the micrometers have a groove in the position marked as ”0”, the one that I kept fixed for all the experiment, it was easy for me to re-position them in the correct, original place once finished the sampling for the sweep in focus. The initial idea for the calculation of the positions of the focuses along the Z axis was to use the focus knob of the MAT as a metric reference. However, this method presented a serious criticality: the large uncertainty of the correspondence between the turn of the focus knob and the spatial distance of the focus of the MAT, since I could only rely on the coarse fit reported in fig3.2. I planned to conduct an experimental fit on this relation, but considering 160 grooves of the knob and the fact that the focus is extremely sensitive in the first turn and much more insensitive in the remaining 0.75 turn, I decided to adopt a different solution. I located 5 mechanical references at known distances along the useful sweep in the focus path. The distance of the references was measured using a caliper using the first surface of the L1 frame (facing the MAT); along the Z axis, I established that the negative verse was toward the MAT, while the positive verse was toward M0. The references were located at: -78.4 ± 0.1 mm; -50.0 ± 0.1 mm; -28.9 ± 0.1 mm; 0.0 ± 0.1 mm; $+23.9 \pm 0.1$ mm.

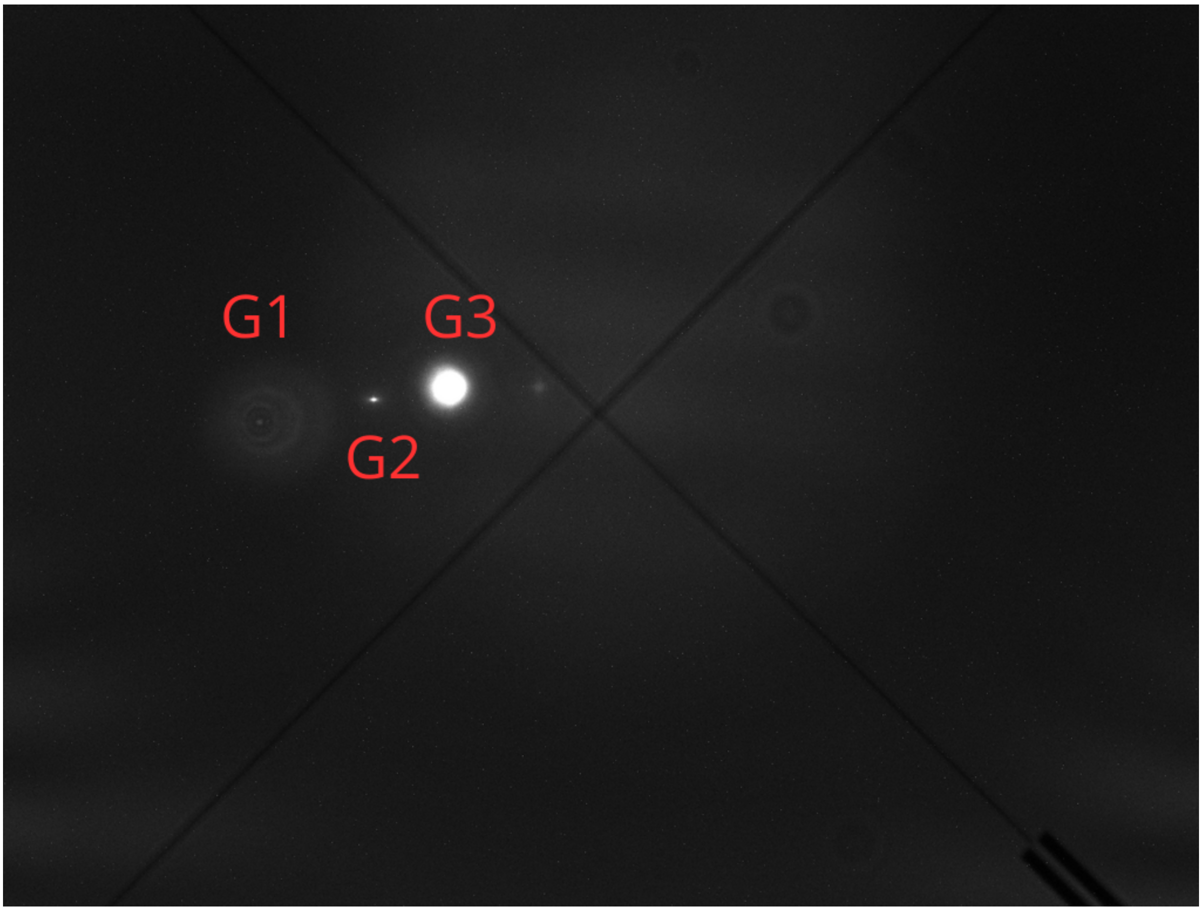

Figure 3.23: Image of the 3 ghosts of L1 in the FoV of the MAT: in the left L1-G1, in the middle L1-G2 and on the right L1-G3.

I measured the distance between the first surface of the lens and the frame with a caliper, resulting 5.25 ± 0.05 mm, and I subtracted it from the distances of the mechanical reference to effectively calculate the distance between the ghosts and the lens, and set it in the reference frame of L1-S1. Before sampling the images of the ghosts, I focused the MAT on a paper grid, located on the mechanical support, to find the exact position of the focus. I kept the gain and the other imaging parameters constant, only changing the exposure time, to avoid the saturation of the ghost. I also took a frame of the background with $t_{exp} = 1$ s so I could subtract it from the images of the ghosts, rescaling the photon count to the ghost frame exposure time. Unfortunately, L1-G2 was too faint and small with respect to L1-G1 and L1-G3 (due to a multiple reflection origin), so the noise coming from the other 2 main ghosts made it impossible to have a correct best focus estimate. Hence, I estimated the size of L1-G2 visually and its best focus position as the distance at which it was more luminous; these approximations are associated with a large error, because the focus had nearly the same size and luminosity along a relatively wide axial range.

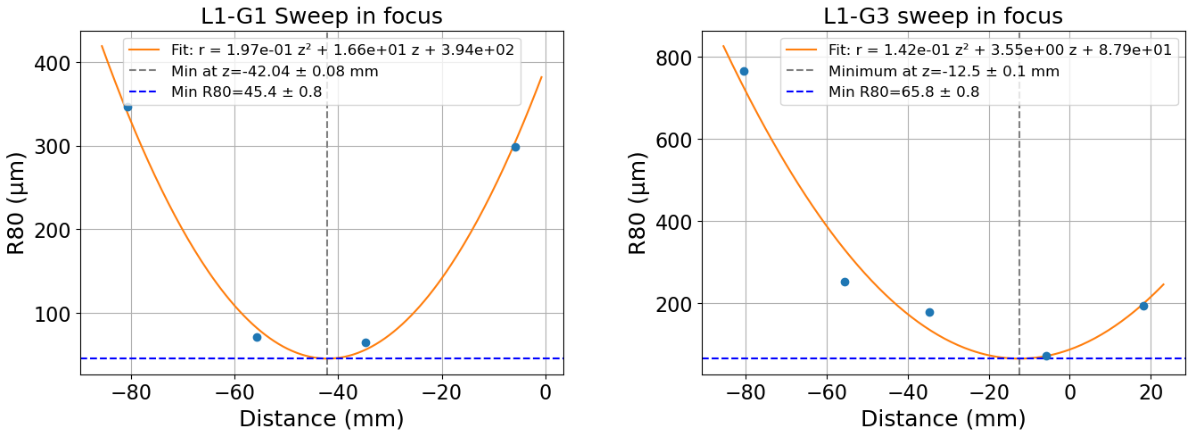

(a) (b)

Figure 3.24: Analysis of the ghost originated by L1: (a) fit of the sweep in focus of L1-G1, (b) fit of the sweep in focus of L1-G3, $\sigma_{R_{80}} \sim 4$ nm is negligible; $\sigma_{dist} = 0.1$ mm.

I found the position of the centroid of the ghosts using the same Python script used for the PIP alignment, but performing only the 2D fit. The results of the fit, superposed to the original ghost images, are shown in fig.3.26. For L1-G1, the residual of the alignment with respect to the cross of the MAT are shown in Table.3.5.

Ghost	Best focus (mm)	R_{80} (μm)	Δx (μm)	Δy (μm)
L1-G1	-42.04 ± 0.08	45.4 ± 0.8	1.7 ± 0.8	-0.5 ± 0.8
L1-G2	≈ 0	≈ 25	3.9 ± 0.8	1.1 ± 0.8
L1-G3	-12.5 ± 0.1	65.8 ± 0.8	3.6 ± 0.8	0.7 ± 0.8

Table 3.5: For each ghost originated by L1, the best focus position with respect to S1 of the lens, R_{80}, in the estimated ghost position, and residual position error with respect to the centroid to the center of the MAT cross.

The sweep in focus for the coaxial, aligned ghosts of L1, seen at different distances from the mechanical reference, is shown in fig.3.25; it was the visual indicator of the goodness of the alignment during the procedure.

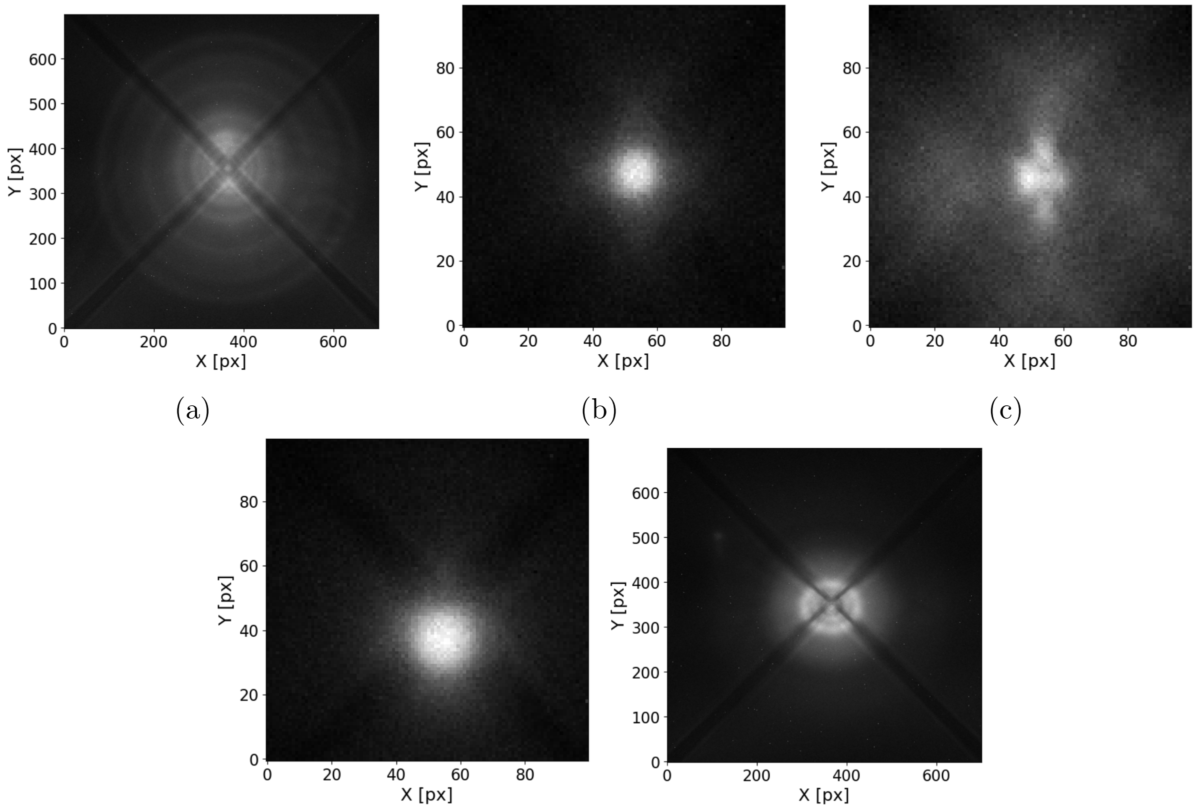

(a) (b) (c)

(d) (e)

Figure 3.25: Sweep in-focus of the background-subtracted, aligned ghosts of L1, taken with different t_{exp}. It is the stack of FoV of the MAT changing the focus; it is a visual test for the goodness of the alignment Distance between the ghost and L1-S1: a) -78.4 ± 0.1; b) -50.0 ± 0.1; c) -28.9 ± 0.1; d) 0.0 ± 0.1; e) $+23.9 \pm 0.1$ mm.

I calculated the alignment error of L1 using L1-G1 and L1-G3 as optical target references, computing both the tilt and the decenter of the lens. I assumed that the centroid of the ghosts was focused along the optical axis of the lens; hence, 2 centroids traced the axis of the lens. In the reference frame of L1, I set its geometrical center as the origin of its optical axis. I compared the axis of L1 traced using the ghost and passing through the origin of the lens with the optical axis of the MAT and the target of the alignment of both the lenses (null decenter within the tolerance of the position of the cross of the MAT and null tilt). The decenter between the 2 axes in the position of the geometric center of L1 (0) represents the decenter of the lens, while their angular distance represents the tilt. The tilt is computed in both X and Y axis, as the 2 axes are in a 3D space, according to fig.3.11.

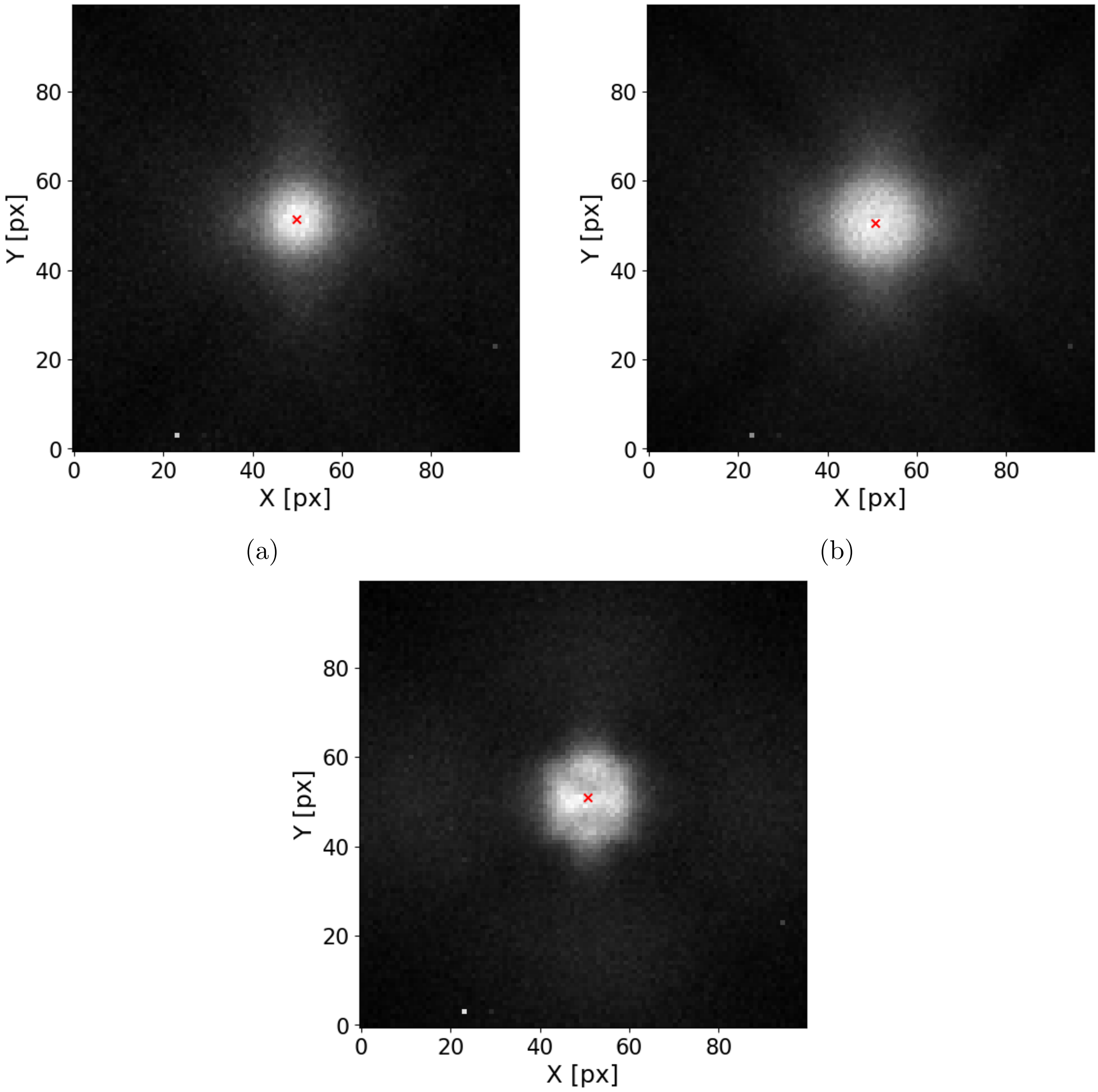

(a) (b)

(c)

Figure 3.26: Centroids of the ghosts found using the 2D Gaussian fit of: (a) L1-G1, (b) L1-G2, (c) L1-G3.

Results of the alignment residual errors of L1:

- Decenter
  - $\Delta x = 5 \pm 2$ μm
  - $\Delta y = 1 \pm 2$ μm
- Tilt
  - $\Delta\theta_x = 13 \pm 8$”
  - $\Delta\theta_y = 7 \pm 8$”

Back-reflection verification

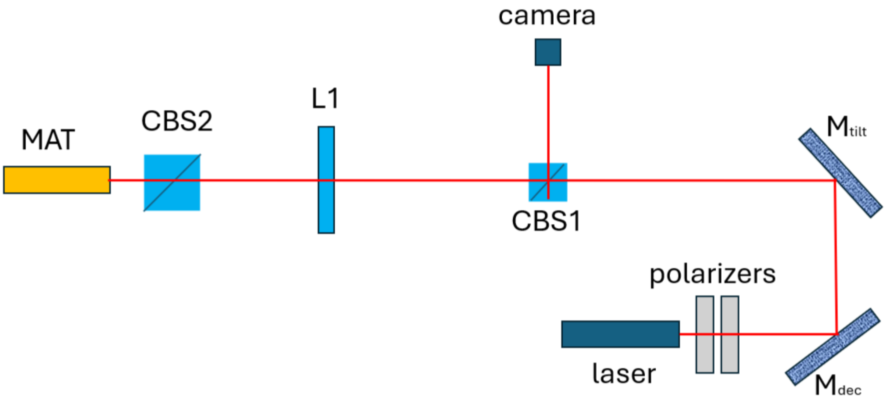

Figure 3.27: Scheme of the back-reflection validation setup.

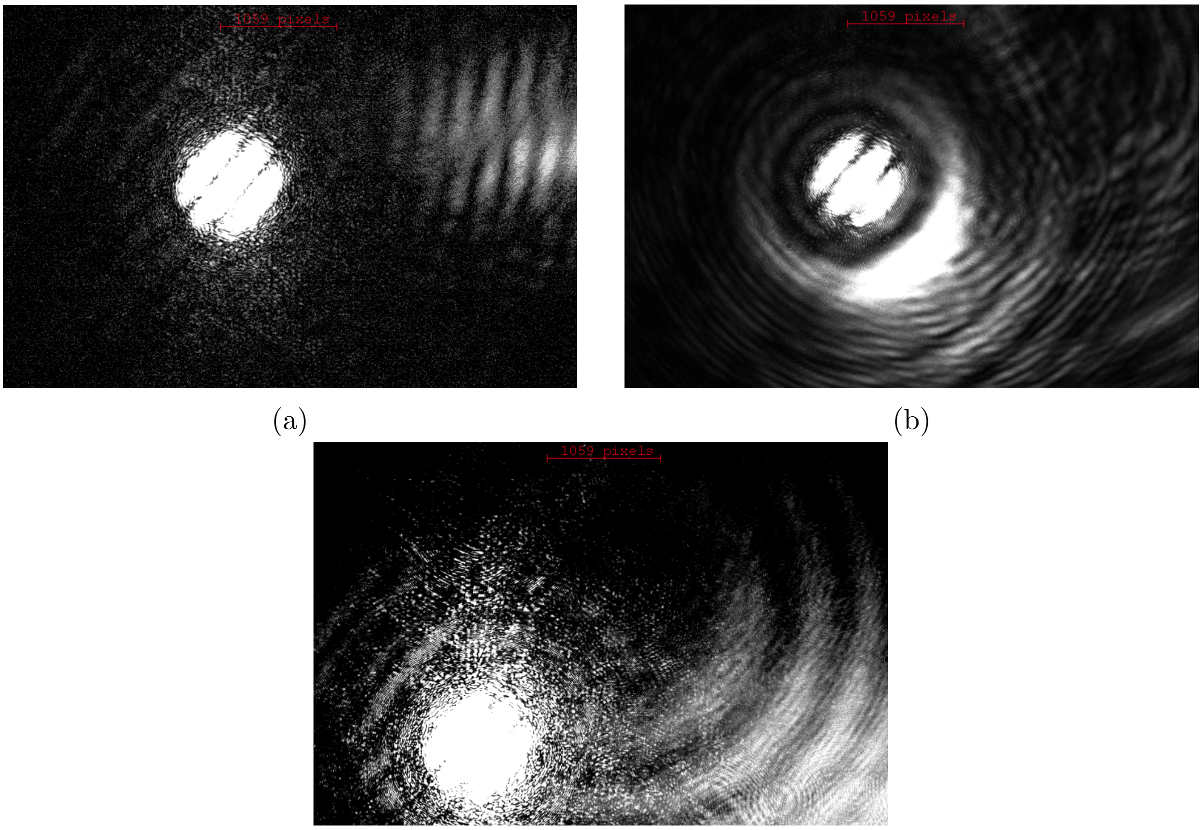

(a) (b) (c)

Figure 3.28: a) Back-reflections of the laser inside the aligned CBS1; the number of interference fringes depends on the reflection path inside the CBS1. b) Back-reflection of the alignment between laser and MAT; the interference fringes of the laser are centered with the Newton rings from the MAT c) Misalignment between laser and L1 back-reflections: the laser interference fringes were no longer centered with the MAT Newton rings after the re-insertion of L1.

To verify the alignment of L1, I observed the back reflection of the reference laser fired through the lens from the opposite verse of the optical axis of the MAT (the setup is shown in fig.3.27). This is also one of the validated techniques used in the MORFRO alignment procedure. To capture the back-reflection, I used a Newport, non-polarizing 1-inch cubic beam splitter (CBS1)[36], positioned 1528 ± 1 mm after the MAT, to reflect the beam into a CMOS camera. At first, I removed L1 and placed the CBS1 to coarsely aligned it with the help of a bubble level. For the fine alignment, I used the laser to adjust its positioning, centering the back-reflections on the surfaces of the CBS1 so they were fired back into the laser aperture. I also moved the CBS1 so the transmitted beam was centered with cross of the MAT. After the procedure, since the laser was aligned with the MAT, the laser, the CBS1 (fig.3.28a) and the MAT (fig.3.28b) were aligned to each other. I inserted the lens into the holder, where it was previously aligned using the PIP, and also checked that the PIP alignment was still correct. The CBS1 split the laser into 2 beams: one was the reflected part, directed to the CMOS camera, and one was transmitted toward L1, and its back-reflection was transmitted back and directed to the CMOS camera. I noticed that the back-reflected laser spots were no longer aligned (fig.3.28c). This is a direct consequence of the real wedge of the lens, which makes it impossible to satisfy the law of reversibility of light rays, thus the validation method suffers the error introduced by the optics.

3.3.6 L2 alignment

L2[37] is an achromatic doublet $f = 500$ mm lens. I repeated the alignment technique of L1, screwing the lens in a tip-tilt frame, mounted on a support equipped with X and Y axis translators. The position along the Z axis was not important for L2 because, without considering the tolerance on the divergence, the collimated beam was constant all over its path; I set the distance between the last surface of L1 and the first surface of L2 at $d_{L1-L2} = 75.0 \pm 0.1$ mm, equal to the focal length of L1; this choice allowed me to eventually insert a mechanical object between the lenses and to attenuate any possible side effect from L1. L2 was fixed to the optical table, with degrees of freedom in tilt and decenter on the X and Y axes; an additional degree of freedom along the optical axis would have been a useless complication to the setup, since the beam was collimated in every position after L1. At first, I aligned it visually, setting it as centered as possible, expecting to be able to see the ghosts using the MAT. However, the only visible ghosts were the ones produced by L1, so to improve the initial alignment of L2, I used the laser and its multiple back reflections on L2, occluding L1 using a black, mechanical stop. I put a sheet of paper in the half of the path between the laser and L2, making a hole to allow the beam to reach the lens; later, I used the decenter (micro-movements of the translators) to approximately center the first back reflection with the hole and the tilt (rotation of the knob on the frame) to center the Newton rings around the hole. I did not perform an accurate alignment, but only a coarse one to settle the lens in a position that could produce observable ghosts; in fact, when the lens was almost aligned by the laser back-reflections, the L2 ghosts appeared. There were 3 useful ghosts, a close one ($\mathrm{L2} - \mathrm{G_a}$), a middle one ($\mathrm{L2} - \mathrm{G_b}$) and a far one ($\mathrm{L2} - \mathrm{G_c}$), shown in fig.3.29; the 3 ghosts were comparable in terms of size and luminosity. I tried the same technique of alignment as for L1, using the close focus as a reference for tilt and the far one as a reference for decenter, however, after several iterations, the alignment degenerated (I was always moving in the same direction, but nothing macroscopically changed). So I used the close focus as a reference for decenter and the far one as a reference for tilt. L2 ghosts had a bigger size than L1 ghosts, and after a couple of sweeps, I learned how

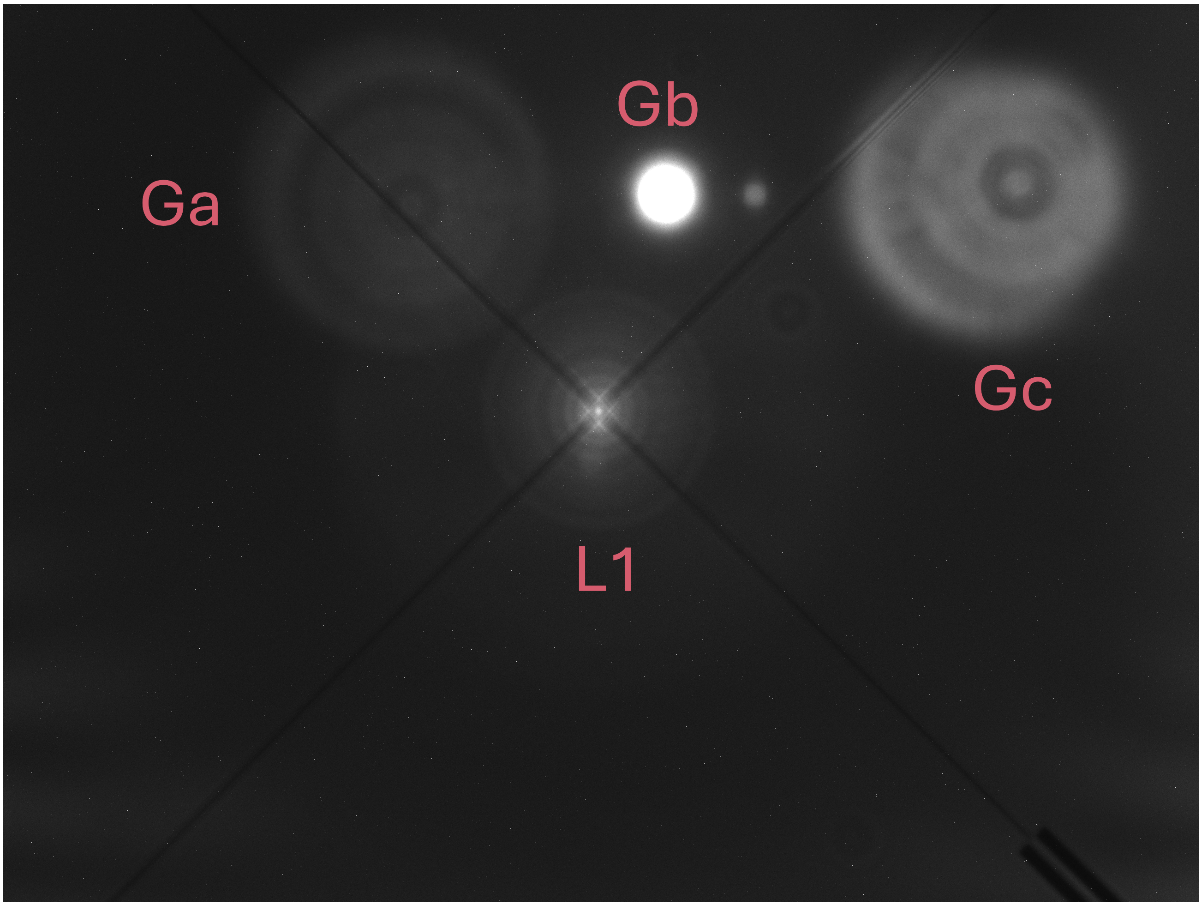

Figure 3.29: Misaligned ghost originated by L2, from the FoV of the MAT. From the left to the right: $L2 - G_a$, $L2 - G_b$ and $L2 - G_c$. Between $L2 - G_b$ and $L2 - G_c$, there is a notable parasite reflection, not listed as a ghost because its position did not change whenever L1 or L2 were moved. The 3 ghosts have approximately the same size and luminosity, but appear much different because the image was taken very close to the focus of $L2 - G_b$; in this position, adopting a certain t_{exp}, $L2 - G_b$ is saturated, whereas $L2 - G_a$ is barely visible. The beam marked as $L1$ is the aligned ghost sequence originated by the collimator lens.

to distinguish them based on the position of the focus and on their shape. After a few iterations and $10-15$ min, I had aligned the 2 reference focuses, in the best trade-off, with the cross of the MAT. I also tried to take the middle ghost as a reference, but I could not properly align it with either decenter or tilt, and, as shown in fig.3.30, it was the least aligned among the L2 ghosts. I used the same Python script of L1 to find the centroids and their relative uncertainty.

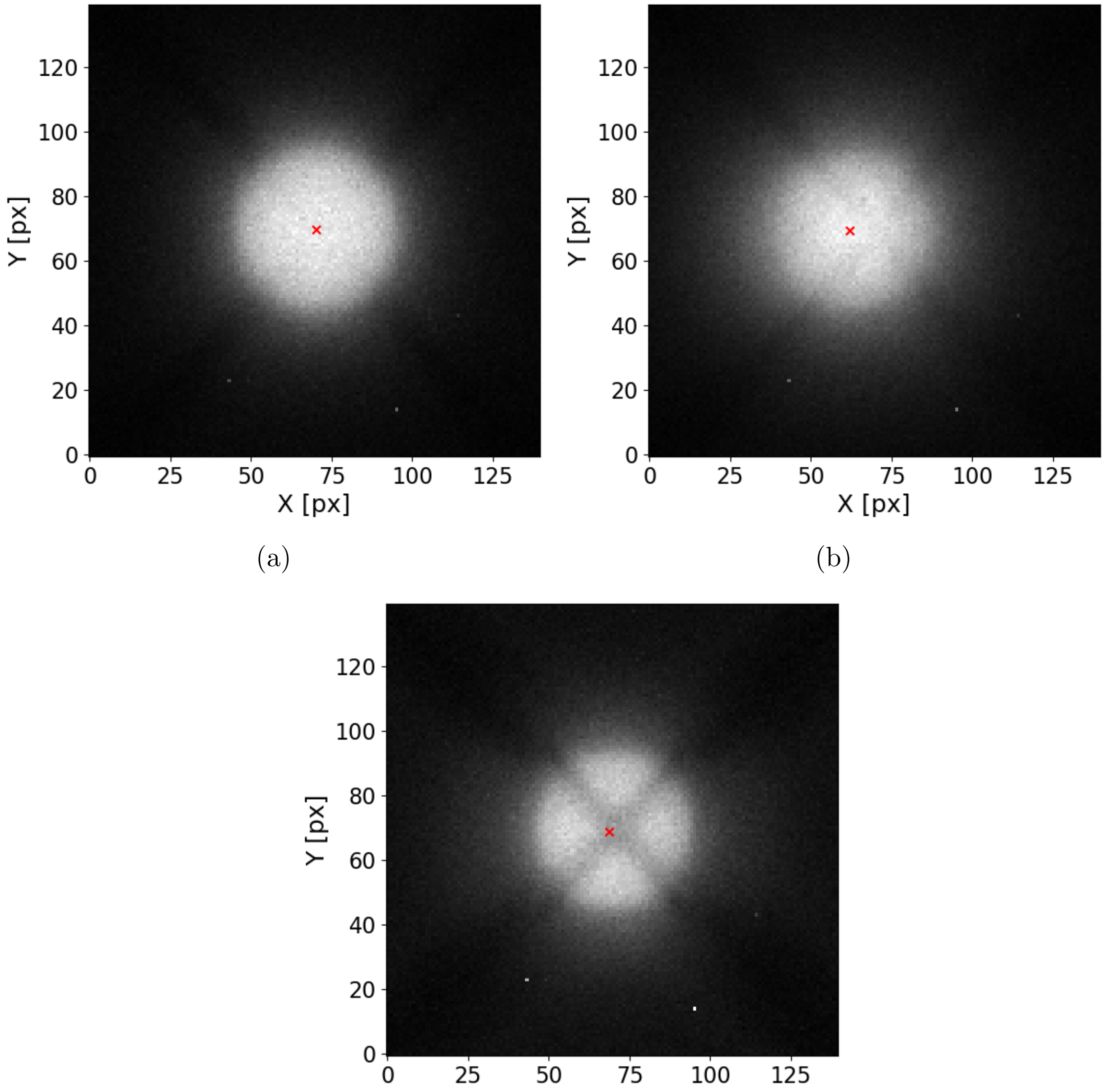

(a)

(b)

(c)

Figure 3.30: Position of the centroids of the ghosts of L2 found using the 2D Gaussian fit of the cross-erased PSF. a) $\mathrm{L2}-\mathrm{G_a}$; b) $\mathrm{L2}-\mathrm{G_b}$; c) $\mathrm{L2}-\mathrm{G_c}$.

I performed the fit of the sweep in focus of the off-axis ghosts, in the same way as the L1 ones. The results are in Table 3.6, while the fits are shown in fig.3.31, and the process of the fitting is shown in fig.3.22. Since the distance of the ghosts was calculated from the 1st surface of the L2 frame, I subtracted the thickness of the lens (6 mm) and the distance between the frame and L2-S3 (5.25 mm) to set the reference frame in the S1 of the lens. The fit best focus position derived for ghosts $\mathrm{L2}-\mathrm{G_c}$ does not present error because the sweep in focus was fitted using only 3 data points, so it does not have any uncertainty. I estimated the errors on the best focus and on the R_{80} being the same

Ghost	Best focus (mm)	R_{80} (mm)	Δx (μm)	Δy (μm)
L2-Ga	-203.90 ± 0.08	123 ± 1	2.4 ± 0.8	2.9 ± 0.8
L2-Gb	-203.08 ± 0.08	126 ± 1	-15.2 ± 0.8	3.8 ± 0.8
L2-Gc	-82.6 ± 0.1	252 ± 1	-0.4 ± 0.8	5.2 ± 0.8

Table 3.6: L2 ghosts, their best focus position with respect to L2-S1, R_{80} estimated ghost size and residual position error to the center of the MAT cross.

order of magnitude as the other 2 ghosts of L2.

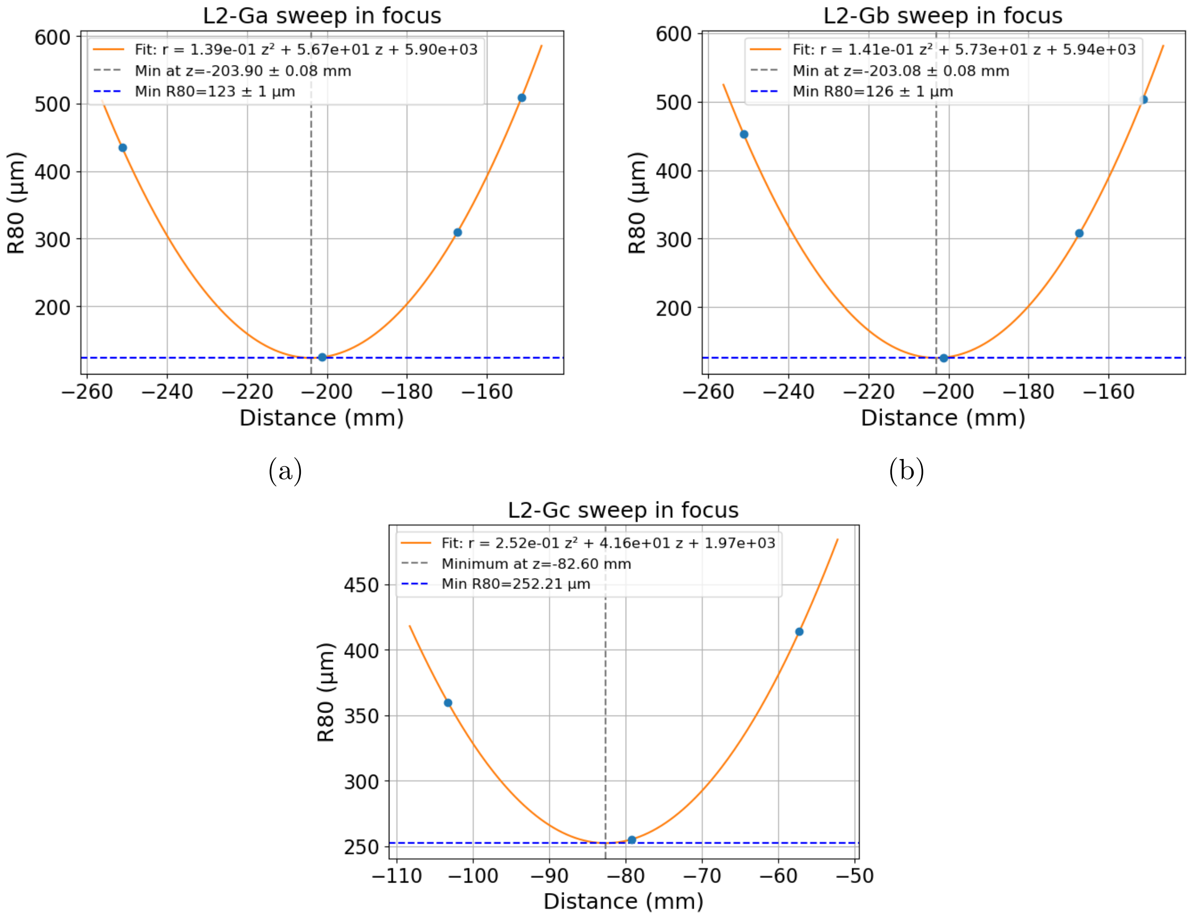

(a) (b)

(c)

Figure 3.31: Sweep in focus of the ghosts originated by L2:(a) ghost $\mathrm{L2-G_a}$, (b) ghost $\mathrm{L2-G_b}$, (c) ghost $\mathrm{L2-G_c}$.

Referring to eq.1.1, I set Δx as the difference between the position of the centroids of $\mathrm{L2-G_a}$ and $\mathrm{L2-G_c}$, and set L as the distance between their best focus position along the Z axis. Results of the alignment residual errors of L2:

- Decenter
  - $\Delta x = -2 \pm 2$ μm
  - $\Delta y = 7 \pm 2$ μm
- Tilt
  - $\Delta\theta_x = -5 \pm 2$”

- $\Delta\theta_y = 4 \pm 2$”

Let us consider the FoV of the MAT with respect to its focal length: the FoV is approximated to a circle having radius D. It is possible to estimate the maximum tilt angle of the lens that allows the observation of the ghost focused at a distance d from the lens. If the lens is tilted by angle α and the ghost is projected along its axis, for the approximation of small α, the distance l between the ghost and the axis of the MAT $l = d \cdot \alpha$ and, to be in the FoV of the MAT it must follow the eq.3.9, shown in fig.3.32

$$l = d \cdot \alpha < D \implies \alpha < \frac{D}{d} \tag{3.9}$$

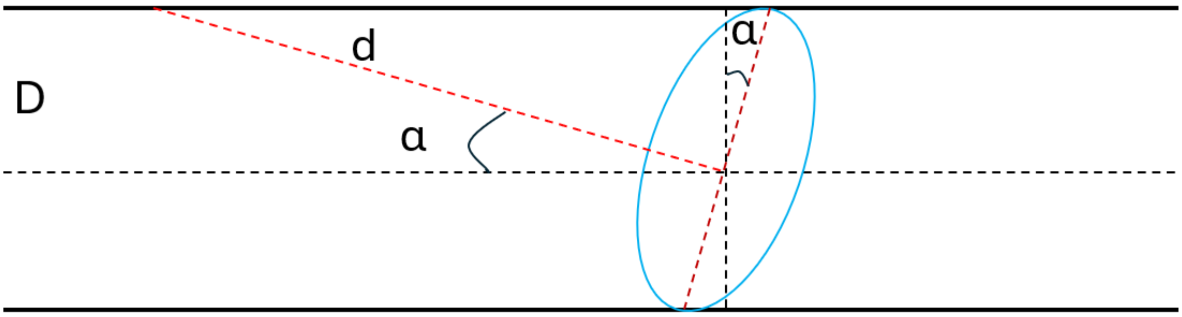

Figure 3.32: graphic explanation of the eq.3.9

In the case of a ghost focused at −203 mm from L2-S1, the distance between the MAT and the ghost is $D \approx 430$ mm at which the FoV is ≈ 21 mm, the result is that the tilt of the lens must be $\lesssim 6°$, while for a ghost focused at −40 mm from L1-S1 at which the FoV of the MAT is roughly the same, implies $\alpha \lesssim 32°$ (found with the cosine formula since it is no longer a small angle). Considering all the strong approximations of this calculation, it is reasonable to say that the ghosts from L1 were visible because of the wide range of visibility angle of the lens, whereas I also expected the ghosts from L2 to be visible, due to the amplitude of the maximum visibility angle esteemd; in fact the human eye should be sensible to 6° of tilt. The position of the ghosts of the entire system is shown in fig.3.33

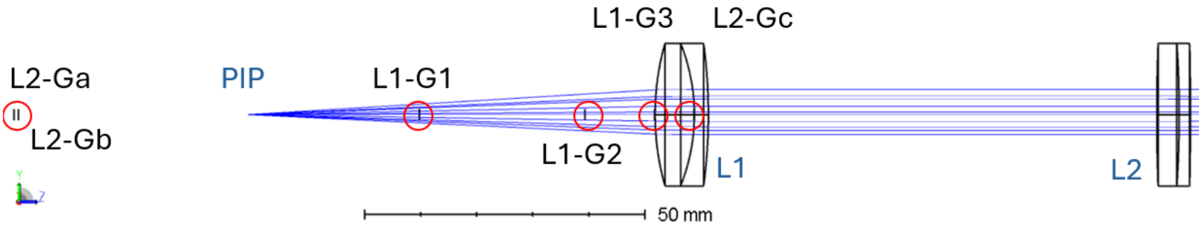

Figure 3.33: Position of the ghosts originated by both L1 and L2 and observed using the MAT.

3.3.7 Zemax simulation of the system

Characterization of the prototype

I simulated the system using Zemax, in order to find the optical features of the ideal, error-free model and the changes after introducing the alignment errors that I estimated. For the error-free system, I used a unique field, which in Zemax jargon indicates the angular distance from the source of illumination and the optical axis; I set the simulated PIP in axis (0° field) using the Numerical Aperture = 0.082718 calculated with eq.3.6, specifying a uniform apodization shape of the beam. I employed a set of wavelengths as light sources, from 400 nm to 700 nm in steps of 30 nm. It was only a small interval of the emission range of the halogen lamp ($360-2600$ nm), however I considered also the transmissivity of the other optical elements: the optic fiber transmits in the range $180-2400$ nm; L0 from the PIP setup, the CBS2 and L1 and L2 from the system has transmissivity range $400-700$ nm; finally the CMOS camera used for the samples has an observational range $\approx 350-1050$ nm. I selected the most stringent interval of wavelengths because it is the effective portion of the spectrum that is detected by the camera. I downloaded the Zemax design of L1 from the website of the manufacturer and imposed its optimization to collimate the beam, hence the first surface of the lens was positioned 72.660 mm after the PIP. The lens has a central thickness of 9.500 mm, consequently its geometric center was located at 77.410 mm from the PIP, which is larger than expected. Since the declared tolerance is ±1%, I anticipated that at a distance equal to the focal length ±1% the beam would be collimated. I downloaded the Zemax design of L2 and positioned the first surface of the lens 75.000 mm after the third surface of L1. Finally, I optimized the distance of the focus (focal plane) to obtain the best focus and the smallest RMS spot of the PSF; the focus was 490.122 mm after the last surface of L2, exceeding the tolerance limits. However, both the best focus and collimation position depend on the selected wavelengths, so it is reasonable to detect a relatively small offset from the theoretical value, compatible with the ones that I noted, respectively, $\approx 3\%$ for the collimation and $\approx 2\%$ for the focus. I used the "Wavefront Map" (fig.3.35b) and the "Spot Diagram" (fig.3.35a) tools to visualize the WFE and understand if the system was diffraction-limited. From the spot diagram, I got the dimensions of the PSFs at different wavelengths, compared to the Airy disk size; from the wavefront map, I noted the wavefront error at each wavelength and understood that the system was not diffraction-limited. We talk about the diffraction limit when WFE RMS $< \lambda/10$ and

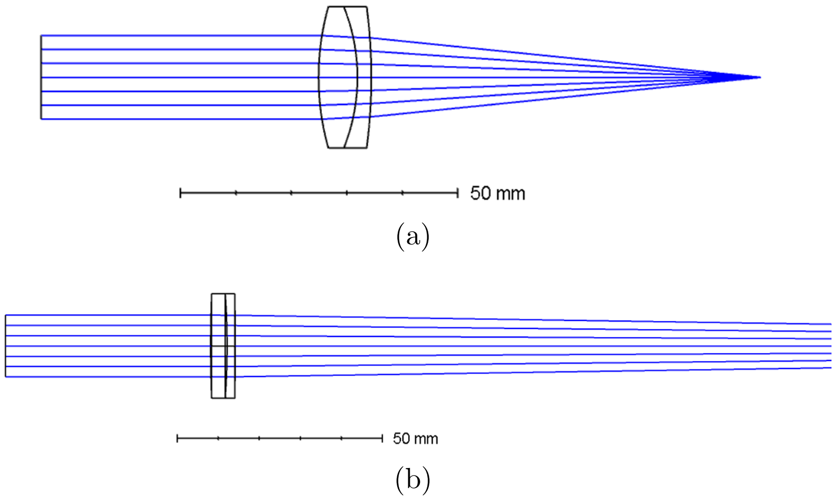

(a)

(b)

Figure 3.34: Size and effect on a collimated beam of the converging lenses (a) L1 and (b) L2.

the best result for the simulated system was WFE RMS $< 0.3910\lambda$ for $\lambda = 580$ nm. The Airy disk resulted in a radius $R_{Airy} = 19.273$ μm, while the $R_{RMS} = 135.692$ μm, confirming the fact that the system was not diffraction limited.

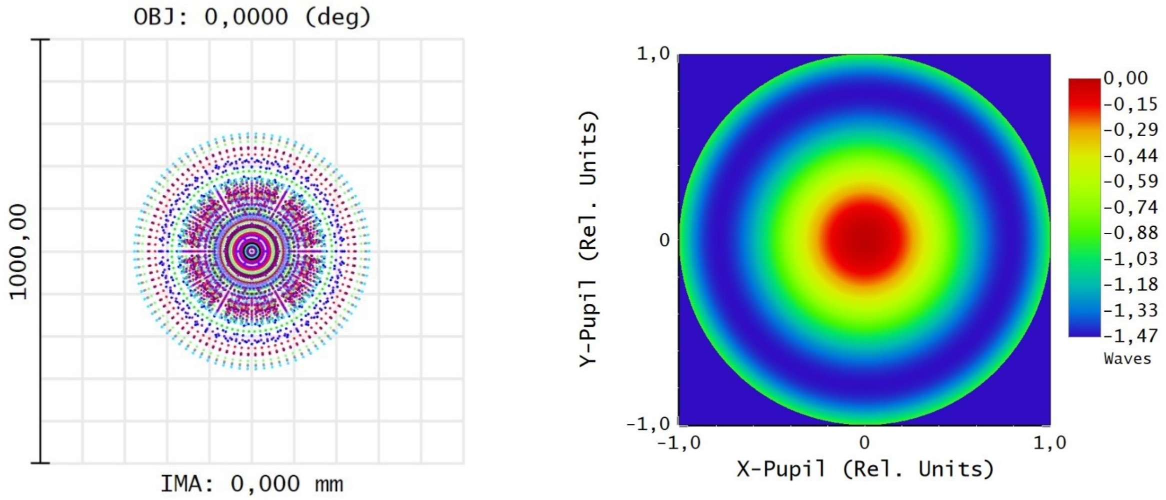

(a) (b)

Figure 3.35: From the ideal system: (a) standard spot diagram with the points colored according to the corresponding wavelength in μm and (b) wavefront map.

Ghost analysis

Zemax allows clients to have 2 different simulation modes: sequential (SQ) and non-sequential (NSQ). Sequential mode offers a faster but less accurate computation of the light propagation, based only on transmission and refraction on the surfaces of the system. Non-sequential mode, instead, requires more computational power but is a more accurate simulator, offering a wider selection of tools (like detectors) and a light interaction with them. In fact, in non-sequential mode, a parent ray can split into multiple child rays after hitting a surface, providing the simulation of the ray tracing in both the desired path and the stray light. The ghost analysis tool, in Zemax, is a generator of simulated reflection of the lenses of the systems, based on the conversion of reflecting surfaces into reflecting ones. It is improved for the search of the stray light (unwanted reflections caused by the components using optical bands), so there is no optimization tool able to change a system to form the ghosts. SQ mode is able to compute only 1st and 2nd generation ghosts, while NSQ mode is finer and can be used also for higher generations; however I since the 2nd generation ghost $L1 - Gb$ was barely visible, I assumed that from the 3rd generation upward I could not visually detect them. For both the SQ and NSQ simulations, I estimated the Relative Intensity (RI) based on the generation of the ghosts, assuming a reflectivity of 5%. The 1st generation has RI = 5%, while the 2nd generation has RI = 0.25%. The summary of the ghost found in the sequential mode of Zemax is in Table 3.7.

Since in the sequential mode of Zemax I could not find any ghost close to L2-G1 and L1-G2, I switched to the non-sequential mode, a more accurate configuration of the system. This mode is based on extremely realistic simulations of the system, including the exact coating of the lenses, which, theoretically, should only influence the percentage of reflected and transmitted rays. I specified the ray tracing of the ghosts of the first

Origin	**RI (%)**	R_{80} **(μm)**	**Axial position (mm)**
L1	5	46.8	-10
L1	5	82.8	-7.8
L1	0.25	113.4	$+4.3$
L2	5	144.0	-152
L2	0.25	45.0	$+31.5$
L2	5	45.0	-48
L2	0.25	45.0	-61
L2	5	45.0	0
L2	0.25	43.2	$+60$
L2	0.25	43.2	$+575$
L2	0.25	43.2	-75

Table 3.7: Summary of ghost reflections found with sequential simulation, normalized relatiev intensities, R_{80}, and positions with respect to the first surface of the origin lens.

Origin	**RI (%)**	**Axial position (mm)**
L1	5	-6
L1	5	-26
L1	0.25	$+7$
L1	0.25	$+14$
L2	5	-192
L2	5	-140

Table 3.8: Summary of ghost reflections found with the non-sequential simulation, normalized intensities (difference between single and double reflection), and positions with respect to the first surface of the origin lens.

generation, since they were relatively luminous and compact and they were focused before both the lenses (hence it could not be a 2nd generation ghost and extremely unlikely a 3rd generation one). I inserted a rectangular detector surface 192.3 mm before L2 (where I found the ghosts), having dimension 0.5 × 0.5 mm and 500 px on each side (pixel size = 1 μm). I imposed the minimum rays normalized intensity threshold at 10^{-6}, to be able to trace also the faintest 1st generation reflections. Visually, a fraction of the rays were focusing close to the detector position, marking a single ghost. Successively, I excluded the 1st generation rays coming from L1, and the ghost disappeared, confirming that the ghost was generated by L2, and finally, I searched surface by surface for L2 to understand which surface was its generator; I found out that it was S1. I moved the detector at ±1 mm (where I expected to fin the double ghost), ±5 mm and ±10 mm from the best focus to find the origin of what seemed 2 separate ghosts in the observation, but looking at the "detector view" in Zemax, I could not find any evidence of a double ghost, and the sampling within ±1 mm from the best focus position were extremely similar. However, in the non-sequential mode, the PSF analysis does not give as output the size of the spot, but it is just a simulation of a real detector (so I could only estimate the fact that the double ghost was not present). The sampling from one of the detector arrays is shown in fig.3.37. To optimize the comprehension of the detectors' sampling, even without conducting a proper sweep in focus of the simulations, I varied the size of the detectors and the number of pixels, in order to keep the pixel size unchanged. The detectors located at ±5 mm from the best focus had size 1 × 1 mm, while the ones located at ±10 mm from the best focus had size 1.5 × 1.5 mm. The only possibility of a similarity between the observation and the simulation is that the ray tracing of the ghost could suggest some increase and decrease in the observed ghost size (shown in fig.3.36)

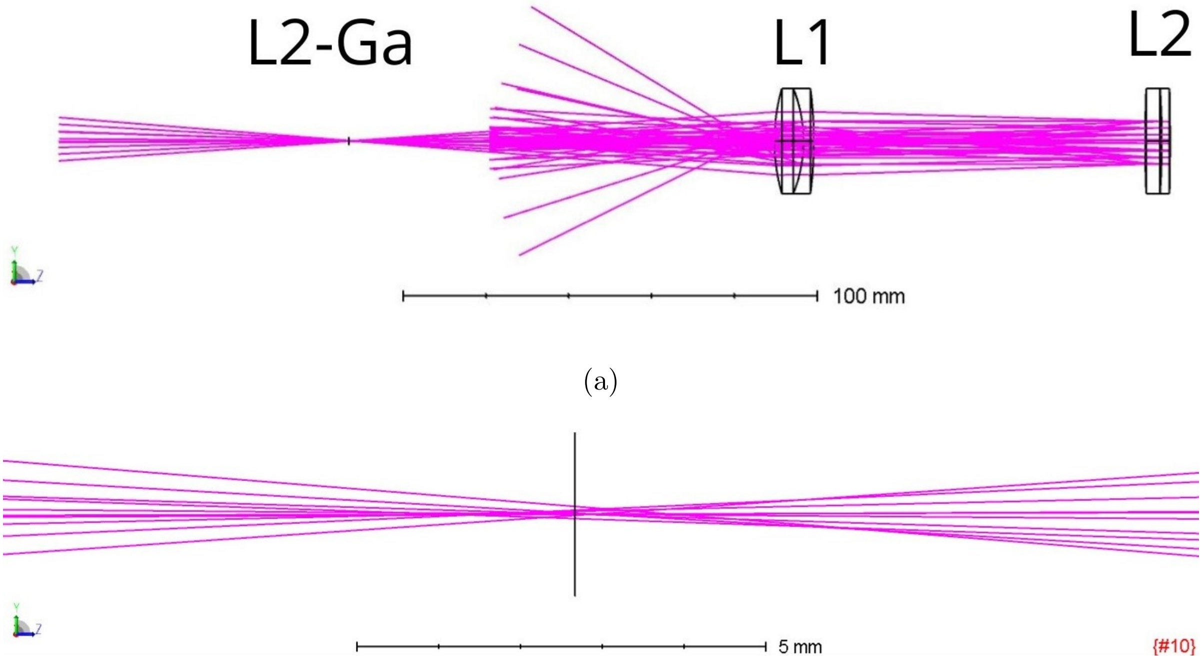

(a)

(b)

Figure 3.36: (a) Setup of the system highlighting the 1st generation ghosts. (b) Zoom on the focus position of ghost $\mathrm{L2}-\mathrm{G_a}$ and $\mathrm{L2}-\mathrm{G_b}$.

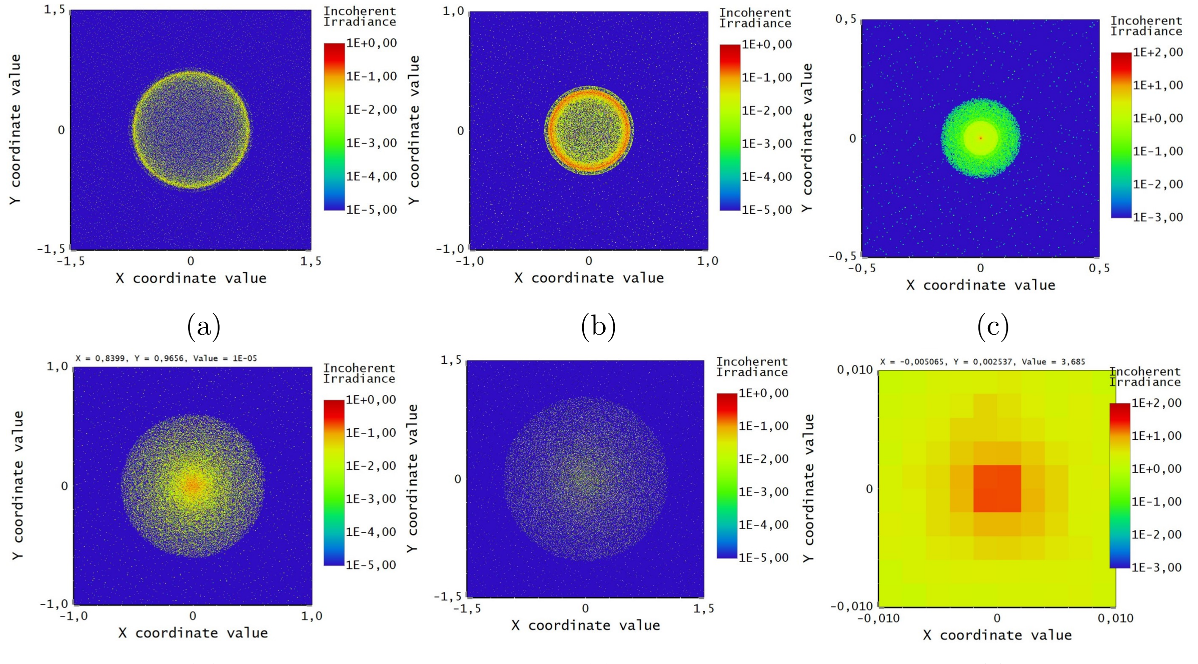

(a) (b) (c)

(d) (e) (f)

Figure 3.37: Simulated detectors: from top left to bottom right, images correspond to detector positions of −10 mm, −5 mm, 0, +5 mm, and +10 mm relative to the ghost best focus. The last image shows the centroid of the ghost at best focus.

Since I found the ghost with milli-metric accuracy, I also tried to locate the other ghost

I observed using the non-sequential Zemax mode. I found 2 1st generation ghost for L1 located $\approx$ 6 mm and $\approx$ 26 mm before L1-S1 and 2 2nd generation ghosts located $\approx$ 7 mm (inside the lens) and $\approx$ 14 mm after L1-S1. For L2, I only found 2 1st generation ghosts, located 192.3 mm and $\approx$ 140 mm before L2-S1; while I did not observe any focused 2nd generation ghosts for this lens.

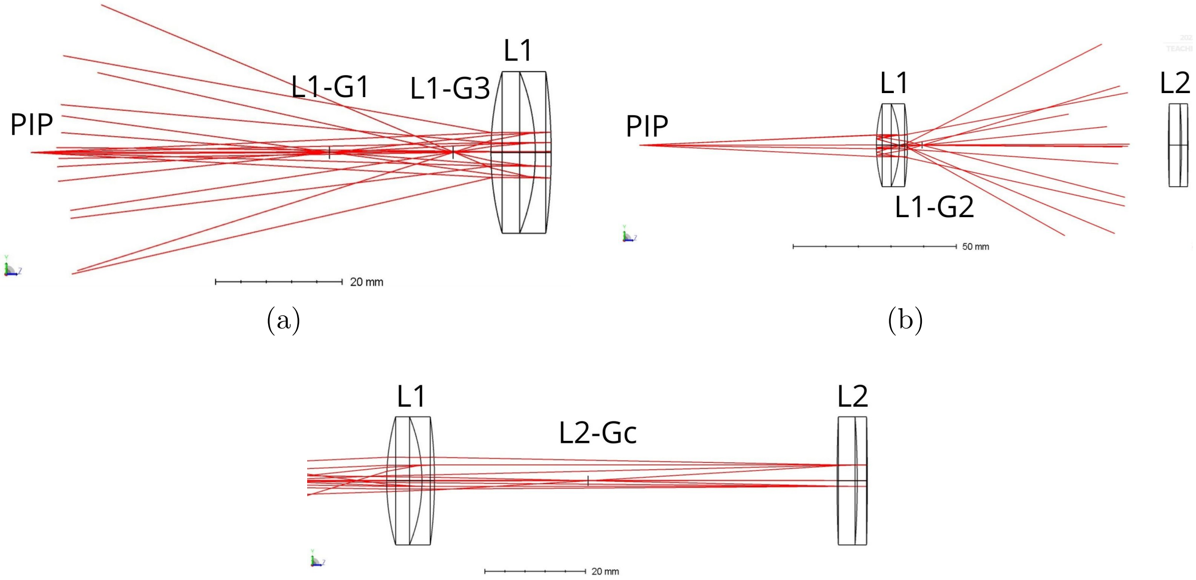

(a) (b)

(c)

Figure 3.38: (a) First generation ghosts originated by L1; (b) 2nd generation ghosts originated by L1; (c) 1st generation ghost originated by L2 (other than the one focused before the PIP image). No 2nd-generation ghost from L2 focused, according to the simulations.

I then proceeded to add the error found through the analysis of the ghosts. I introduced the lenses decenter and tilt errors in Zemax using the standard approach: inserting a "Coordinate Break" surface before and after the lens, with equal magnitudes but opposite signs for the errors. The PIP misalignment was modeled by applying the corresponding offsets to the entire L1–L2–focal plane system. This was achieved by inserting a single "Coordinate Break" surface before L1, so that all subsequent surfaces, hence the setup excluding the PIP image, were affected. The system performance did not change much: the new values of Airy disk and RMS size were, respectively, $\approx 16\mu$m and $\approx 122\mu$m, while the focus was $\approx$ 410 mm after L2, thus the residuals of alignment were small enough to imply an almost negligible contribution to the performance of the system.

3.3.8 MTF of the prototype

The Modulation Transfer Function (MTF) is a feature of the optical systems that indicates how good its performance is as an imager. The MTF describes the goodness of contrast transfer at different spatial frequencies, which is essentially a measure of the resolution of the system. This parameter was crucial for my test, since the alignment

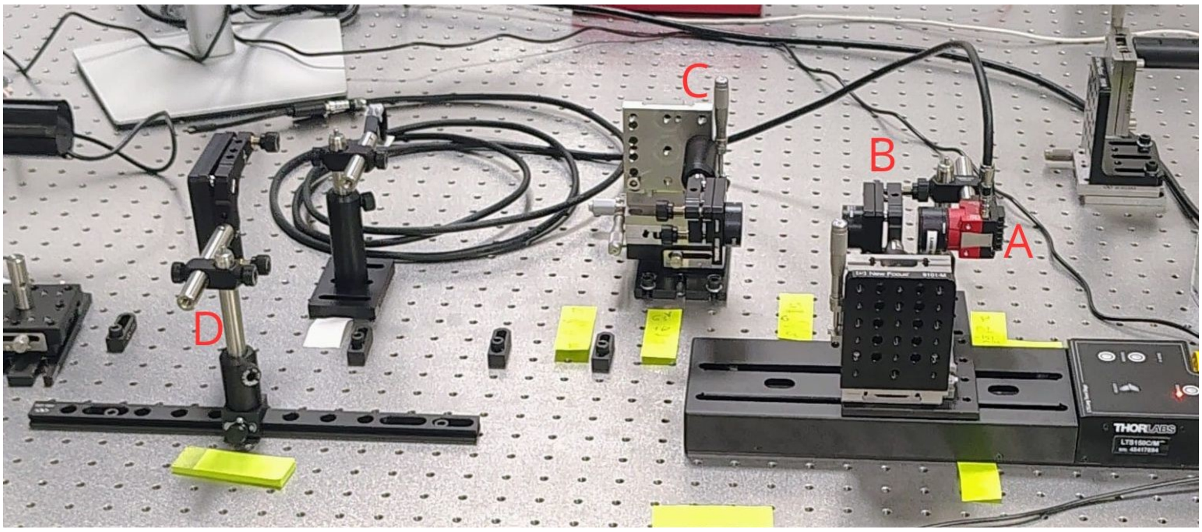

Figure 3.39: Setup for the measurement of the MTF. A) CMOS camera; B) L1; C) L2; D) MTF target.

strategy also required a careful consideration of the system's imaging quality. On the apposite targets (fig.3.41), resolution is often expressed in terms of line-pairs per millimeter (where a line-pair is a sequence of one black line and one white line), which is also a measure of the frequency. In order to verify the resolution, I used an Edmund Optics 2" x 2" Positive, USAF 1951 Resolution Target[38]; I mounted the silica target on a support in the position of the input focus of the systems, approximately 500 mm after L2 and I mounted a CMOS camera in the position corresponding to the output focal plane (fig.3.39). I back-illuminated the MTF target with a monochromatic, red source of light, using a page on the mobile phone screen to guarantee a unique wavelength, coming from an approximately uniformly distributed source (fig.3.40). To allow the best possible achievable resolution, I found the best contrast of the image, both with the position of the mobile phone, the position of the target, and the setting of the camera. Initially, I back-illuminated the target with a polychromatic light coming from the torch of a mobile; however, the contours of the MTF target appeared blurry, which was caused by the fact that every color (wavelength) in the light beam had a different diffraction with the obstacle (black parts) of the target.

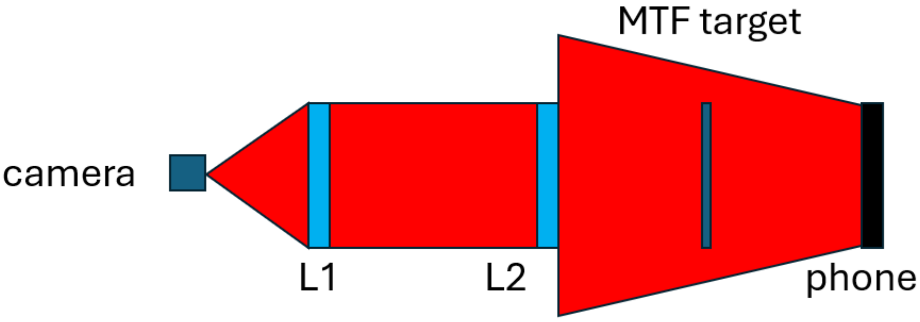

Figure 3.40: Scheme of the MTF setup. The red light comes from the mobile phone, crosses the MTF target, is collimated by L2 and focused on the CMOS camera by L1.

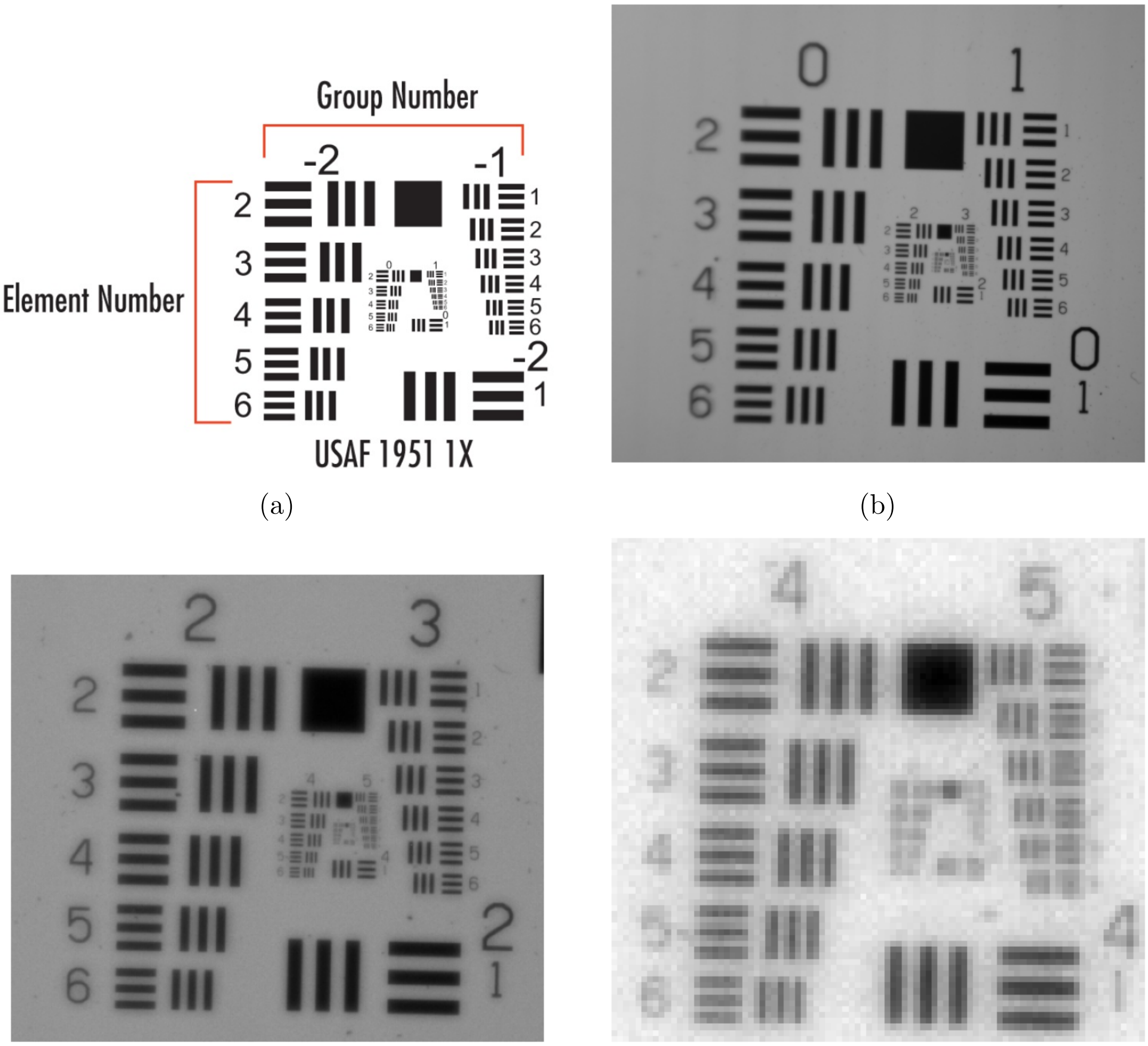

(a) (b)

(c) (d)

Figure 3.41: (a) Optical tool used to estimate the resolution of a system. (b)–(d) Progressive zoom of the image of the target for the estimation of the resolution, taken using the CMOS camera.

As explained by the constructor, the resolution is given by:

$$\text{Resolution} = 2\left(\text{Group Number} + \tfrac{\text{Element Number}-1}{6}\right) \tag{3.10}$$

using Group Number = 5 and Element Number = 4, as the smallest triplet of lines distinguishable, resulting in Res = 45.3 lines/mm . The constructor declares that the MTF of an aberration-free system, follows the equation:

$$MTF(\xi) = \frac{2}{\pi}\left(\phi - \cos\phi \cdot \sin\phi\right) \tag{3.11}$$

where

$$\phi = \cos^{-1}\left(\frac{\xi}{\xi_c}\right), \quad 0 \leq \xi \leq \xi_c \tag{3.12}$$

and ξ_c is the cut-off frequency, so the maximum resolution of the system. The results are shown in fig.3.42

Since the ideal system is not diffraction-limited, I used the Zemax tool "Geometric MTF" to visualize the projected MTF. I simulated the MTF for both the ideal system and the perturbed system, showing the results in fig.3.42; they appear very similar, witnessing that the error on the setup is negligible.

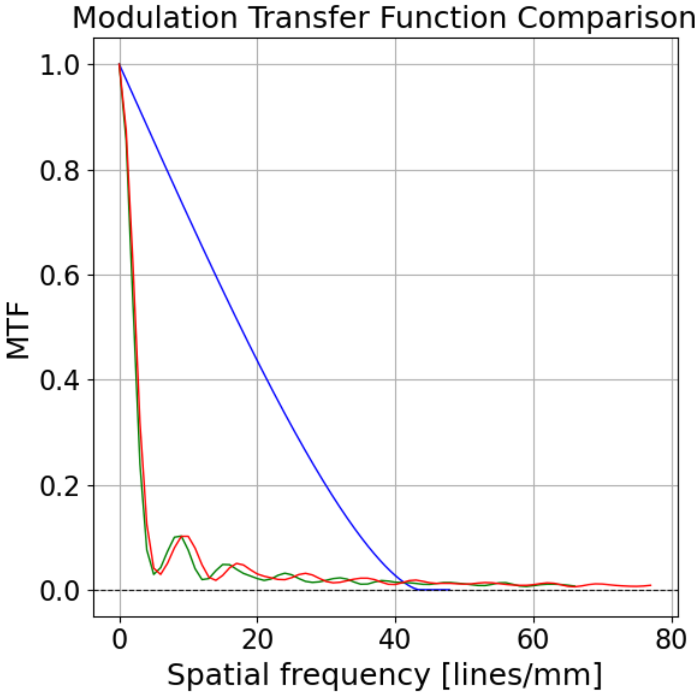

Figure 3.42: Comparison of different MTF profiles: the blue line represents the analytical MTF of the aberration-free prototype, found using eq.3.12; the green line represents the geometric MTF of the Zemax simulation of the prototype; the red line represents the geometric MTF of the Zemax simulation of the prototype perturbed by the alignment residuals calculated in the laboratory experiment.

3.4 Considerations from the prototype

Let us analyze the possible issues. The main criticality of the LGSO alignment conducted with the ghosts technique will be the search for the ghosts of the lenses, their belonging to the correct lens surface, and the distance between the ghosts to calculate the error. Since the ghosts of L1 were easy to observe, even with the misaligned lens, while L2 ghosts were visible only where it was almost aligned, and the FoV of the MAT may not be the responsible for this, it is reasonable that increasing the number of lenses, the difficulty in finding the ghosts will increase too, independently on the fine alignment of each lens. One of the concerns could be the dimension of the ghost: in L1 the largest ghosts had a $R_{80} \sim 50$ μm, while for L2 it was approximately 3-5 times bigger (two of them had $R_{80} \approx 125$ μm and one had $R_{80} \approx 250$ μm). I did not expect these values for 3 main reasons: Zemax simulation, expectation from the collimated beam and ghost position. First of all, the ghost analysis with Zemax gave an output of single and double reflection ghosts, which, according to the luminosity rescaling after any reflection, can be considered sufficient for my observations. Between the 11 simulated ghosts that I found, 8 of them had an RMS size of the PSF in the range ≈ 25 μm, while the others 46 μm, 63 μm and 80 μm. Assuming the PSFs to be a perfectly gaussian shaped, the values of R_{80} correspond to 1.8 times the RMS radius, hence between $\approx 45\ \mu$m for 8 of them and $\approx 80\ \mu$m, $\approx 115\ \mu$m and $\approx 145\ \mu$m (summary in tab.3.7). It is clear that the Zemax simulations are not efficient and reliable, both in terms of the number, position, and size of the ghosts, so they must be searched by chance, defocusing the MAT until they are found. The ghosts of L2 should have been, on average, more compact than the ghosts of L1; I expected so because they were formed by a collimated beam reflected on a long focal length lens, theoretically the best case scenario. Considering L1 − G2 and assuming the very likely hypothesis that it was a 2nd generation ghost, it was impossible to find its actual focus and size. Moreover, even if the sequential mode simulation modeled a few 2nd generation ghosts formed by L2, I was not able to observe them. Having troubles in the observation and characterization of secondary reflection ghosts is surely a disadvantage for this alignment technique, because it heavily reduces the optical lever for the alignment and calculation of the accuracy in the case of my setup.

Chapter 4

Expectation from the LGSO alignment

4.1 LGSO simulation

The LGSO module[3] will arrive at INAF-OAS after being assembled and aligned by the manufacturer. The LGSO will likely be a monolithic opto-mechanical assembly. The requirement for the constructor is that each lens will be aligned with tolerance on the decenter $\approx 100\ \mu$m and tilt $\approx 6 \cdot 10^{-3}$deg $= 21.6$". In the MORFEO Bologna Integration Hall, and later in the ELT facility, LGSO shall be aligned to MORFEO. The technique that will be used to align the LGSO to MORFEO is still under discussion, but will have to satisfy the requirements of decenter residual error < 1 mm and tilt residual error $< 0.1° = 360$". Referring to the ghost alignment method, the MAT will be fixed and aligned to MORFEO, before the corrective plate, using the back-reflection on its lenses. The minimum requirement is to have 2 usable ghosts for the entire LGSO system, while the best case is to have at least 1 usable ghost for every lens. The presence of the dichroic and the corrective plate shall not influence the reliability of the operation, so their ghosts shall be away from the relevant LGSO ghosts' path, making them identifiable.
I simulated the LSGO in Zemax to verify the theoretical feasibility of the ghost alignment technique applied to a lab prototype; in the Zemax settings, I chose the Sodium, monochromatic wavelength of the LSG at $\lambda = 589$ nm, and the on-axis field. The coating of the optical components is still not finalized, so I assumed 98% as the mean transmittance, even if it will probably be higher to optimize the LGS sensing. At first, I searched for the ghosts of the Corrective Plate (CP) (fig.4.1), positioned between M5, the last mirror of ELT, and M6, the first mirror of MORFEO. CP-S1 produces a ghost located 4986 mm along the optical path, before the plate itself, having $R_{RMS} = 22\ \mu$m, it will be very visible but probably will be focused behind the position MAT; CP-S2 produces a ghost located 4923 mm before the plate, having $R_{RMS} = 4130\ \mu$m, which will be more difficult to observe, thus none of them will be an obstacle for the search of the LGSO ghosts. The ghost originated by the double reflection between CP-S2 and CP-S1 would be focused slightly after the LGS-WFS so will produce a spot on the WFS with size $R_{RMS} = 1307\ \mu$m, decentered of -0.081 mm and -0.528 mm on the plane, polluting the sensing with a relative intensity of $\approx 0.04\%$. After that, I modeled the ghosts originated by the dichroic (fig.4.2), which at the LGS wavelength is a flat window tilted by -5.207° from the X axis and by 10.049° from the Y axis. As I expected, the single reflection ghosts, both from DIC-S1 and DIC-S2 of the dichroic are focused far from the optical

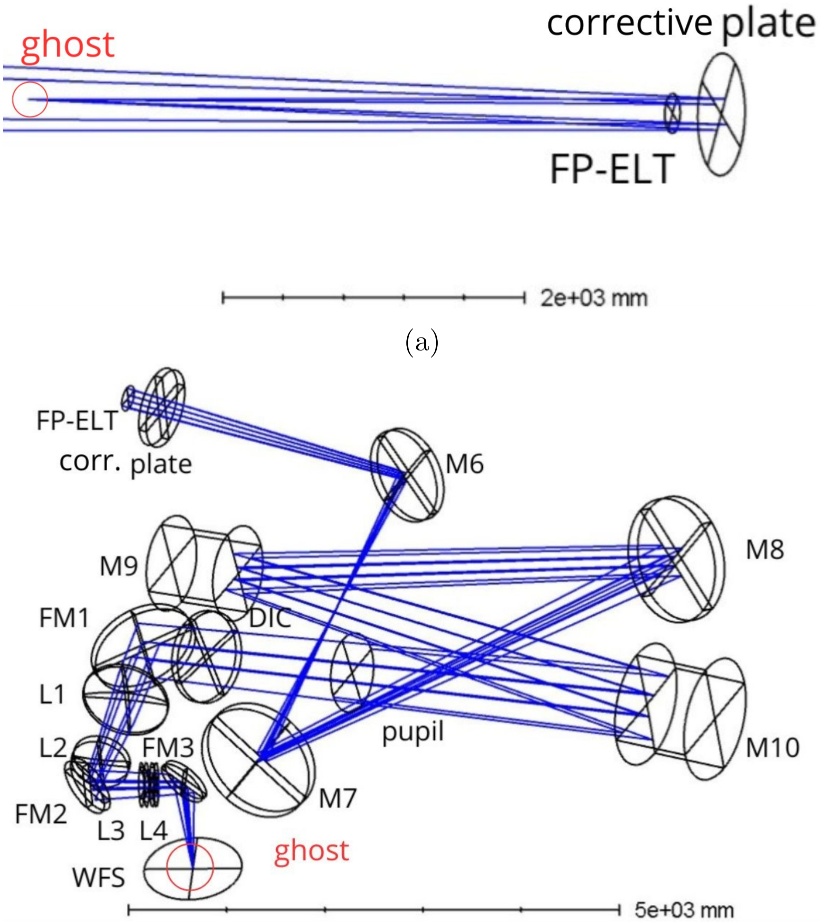

(a)

(b)

Figure 4.1: (a) Position of the ghost originated by the CP-S1; its position is also similar to the ghost originated by CP-S2, located in the optical path between M5 and M6. (b) Position of the 2nd generation ghost of the corrective plate, almost focused on the WFS, which could represent an issue for certain observations.

path, hence do not represent an issue for the LGSO alignment; the secondary ghost, however, follows the optical path of the LGSO and will be focused in extreme proximity of the LGS-WFS[39]. This is understandable, since the double reflection cased by a flat window are very close to the transmitted beam; in any case, it should not be a remarkable issue, since the prospected luminosity of the ghost is 0.04% of the LGS luminosity and it is decentered from the WFS of -3.855 mm and -1.285 mm. Since the size of the LGS-WFS is in the order of tens of mm, the 2nd generation ghosts originated by the corrective plate and the dichroic will be detected.

About the LGSO lenses, I first looked for the ghosts originating from LGSO-L1 (fig.4.3); nevertheless, LGSO-L1-S1 is convex, so I did not expect any ghost coming from the single reflection of the beam in this surface. The beam reflected by LGSO-L1-S2 initially diverges, but it becomes convergent after exiting LGSO-L1-S1 and is focused 1621 mm before the dichroic, outside the LGSO path. It would be a great advantage in terms of optic leaver to have such a distant ghost, however, $R_{RMS} = 7809$ μm, making it almost indistinguishable from the background, and the inclination of the dichroic also changes the direction of the beam, which is focused off-axis, resulting in its unusabil-

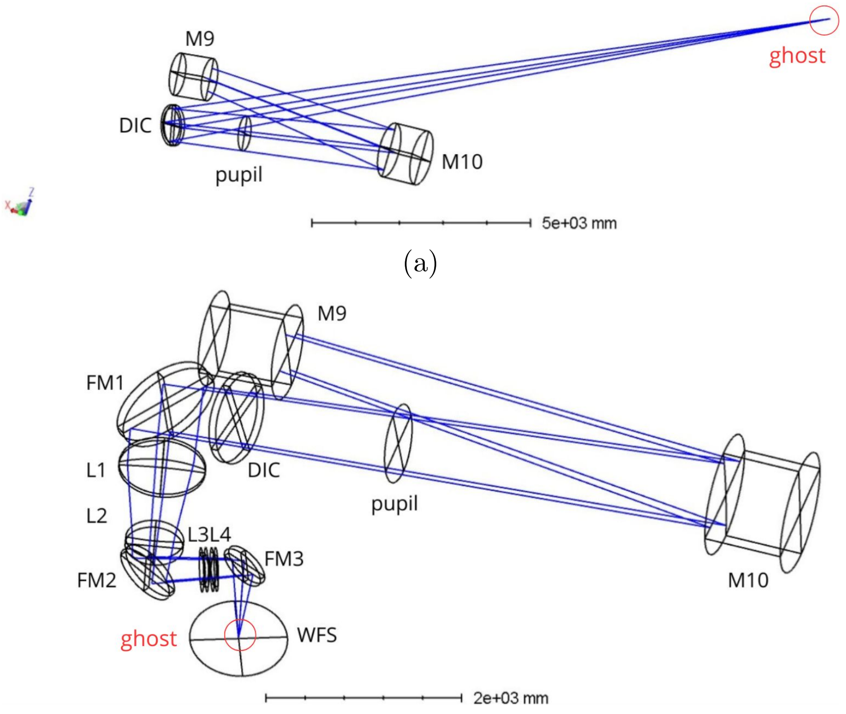

(a)

(b)

Figure 4.2: (a) Position of the ghost originated by the DIC-S2; its position is also similar to the ghost originated by DIC-S1, located outside the optical path of ELT+MORFEO. (b) Position of the 2nd generation ghost of the dichroic, almost focused on the WFS, which could represent an issue for wavefront sensins.

ity. The second-generation ghost formed by the double reflection between LGSO-L1-S2 and LGSO-L1-S1 converges 310 mm after LGSO-L1, but its low luminosity and its $R_{RMS} \approx 18000\ \mu$m make it difficult to observe and to compute an accurate search of the centroid.

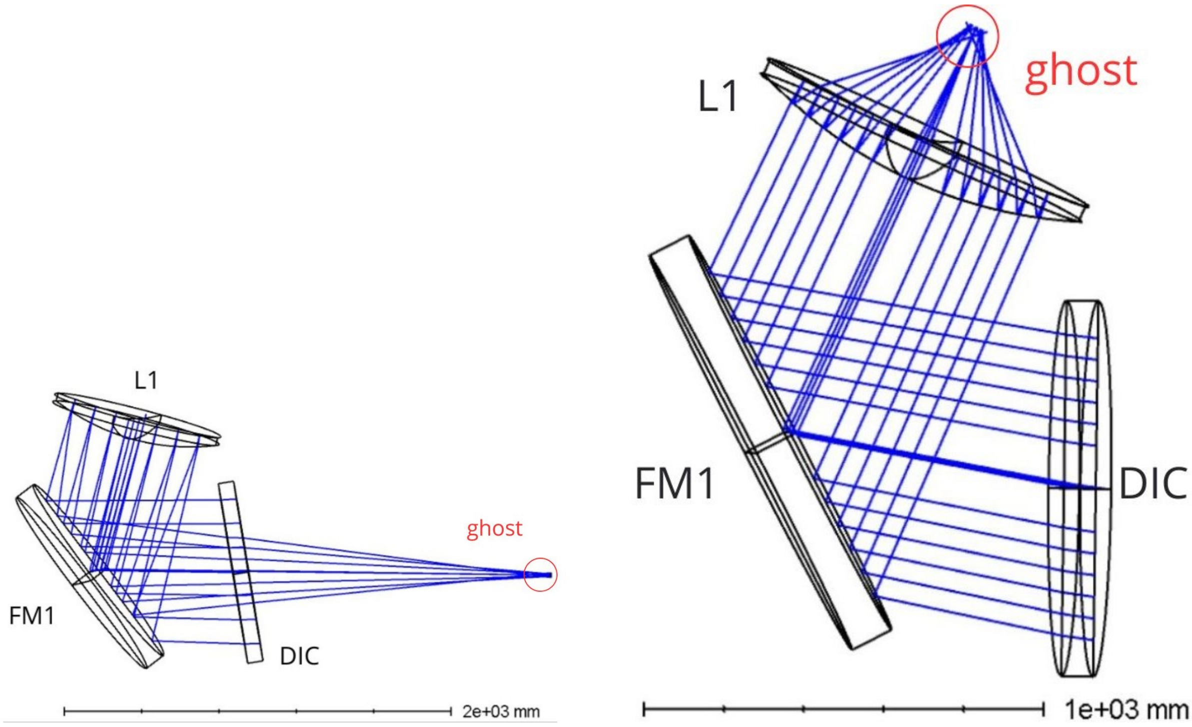

(a) (b)

Figure 4.3: (a) Ghost originated by LGSO-L1-S2 and focused before the dichroic, making it unreliable for the alignment purpose. (b) 2nd generation ghost of LGSO-L1.

LGSO-L2 forms 2 single reflection ghosts, yet one is difficult to observe, and one is at the limit of suitability for the alignment purpose. The ghost originated by LGSO-L2-S1 is focused 345 mm after LGSO-L1 and its $R_{RMS} = 1281$ μm; it is a limit case because its dimension is relatively big, but still observable, and the fact that the ghost is first generation increases the chance to be observed. It would be very useful in terms of optic lever and, even if not considered as a primary ghost for the computation of the alignment error, it could be used for the fit of the ghosts. The other first-generation ghost, formed by LGSO-L2-S2, is focused before the dichroic, hence presents the same issue of the LGSO-L1-S1 ghost, being off-axis and almost unusable.

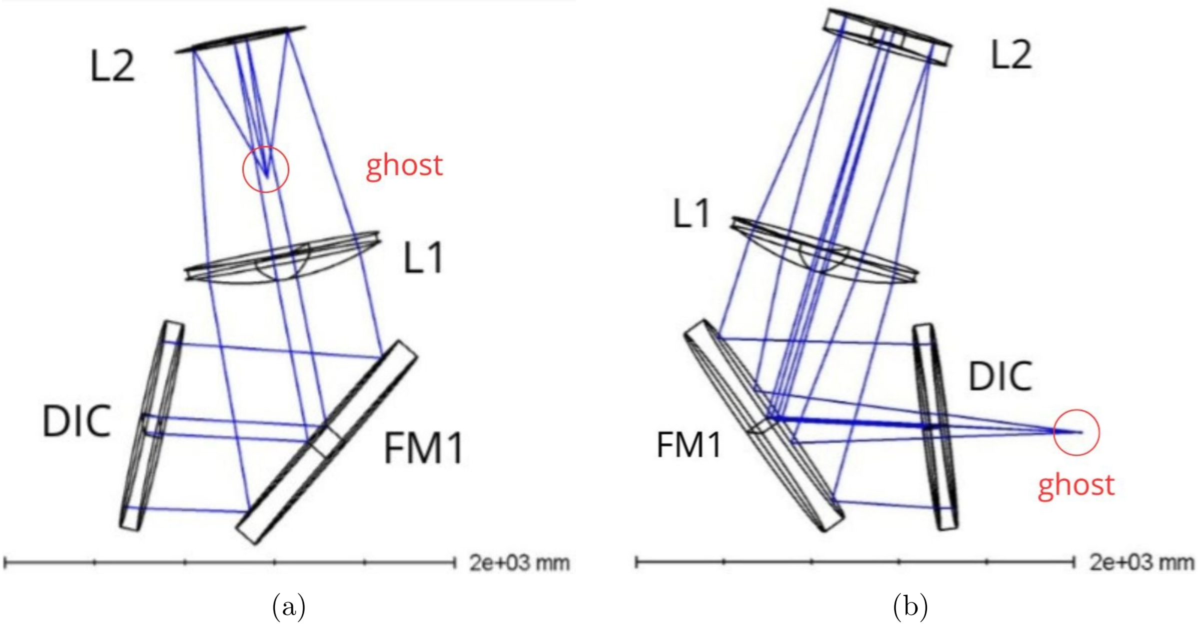

Figure 4.4: (a) Ghost generated by LGSO-L2-S1 (b) Ghost originated by LGSO-L2-S2 and focused before the dichroic, making it unreliable for the alignment purpose.

LGSO-L3 forms 2 1st generation ghosts. The one originated by LGSO-L3-S1 is focused 1639 mm after LGSO-L1 and its $R_{RMS} = 1522$ μm; as discussed for ghost LGSO-L2-S1, it is a limit case, more useful for the fitting of the centroids of the ghost than for the alignment error calculation. The ghost generated by LGSO-L3-S2 instead is focused 1266 mm after LGSO-L1 and its $R_{RMS} = 320$ μm; it would be suitable for the alignment due to its size and luminosity. However, the fact that 2 ghosts are so close, and relatively luminous, could influence the visibility and the centroid search of ghost LGSO-L3-S2, especially considering the correspondence between the rotation of the knob and the focusing distance.

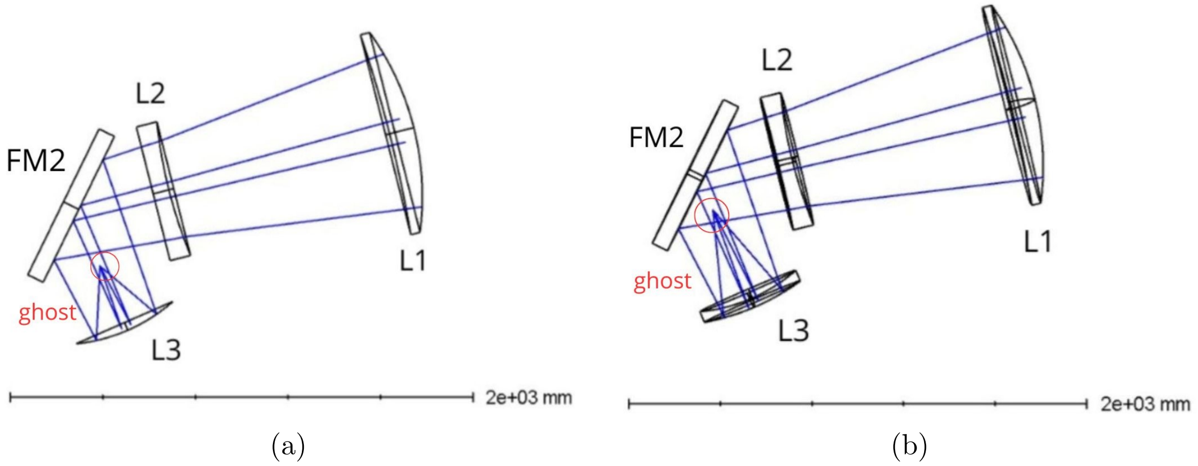

Figure 4.5: (a) Ghost generated by LGSO-L3-S1 (b) Ghost originated by LGSO-L3-S2. They are very close and could be difficult to distinguish.

Finally, LGSO-L4 produces a first generation and a second generation ghosts. LGSO-L4-S2 form the first generation ghost, focused 1486 mm after LGSO-L1 and its $R_{RMS} = 659$ μm, making it suitable for the accuracy computation. The second generation ghost is formed by LGSO-L4-S1 and LGSO-L4-S2 and is focused 2338 mm after LGSO-L1 and its $R_{RMS} = 1645$ μm, hence on the acceptability limit.

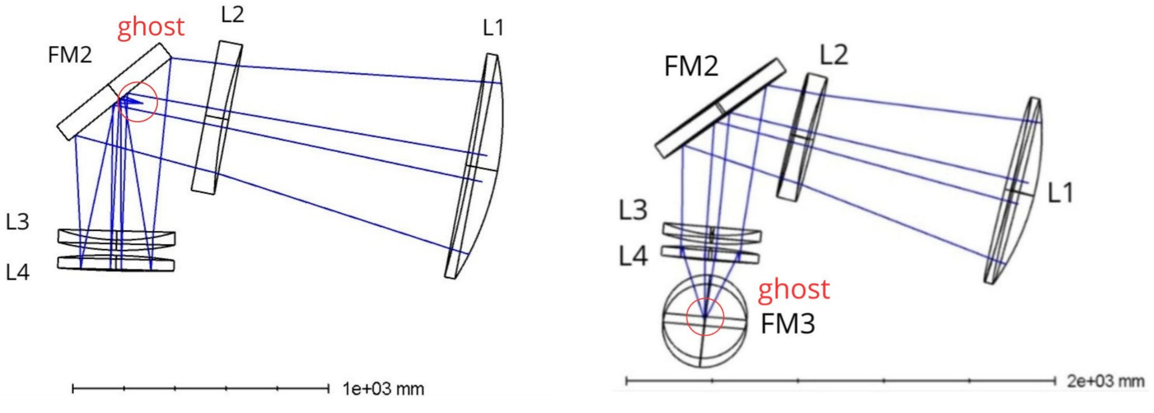

(a) (b)

Figure 4.6: (a) Ghost generated by LGSO-L4-S2 (b) 2nd generation ghost originated by LGSO-L4-S2 and LGSO-L4-S1 and being focused on the FM3.

Considering the best optical leaver achievable from the maximum distance between ghosts having $R_{RMS} \sim 1000$ μm, it is $L = (2338 - 345)$ mm $= 1993$ mm, whereas if I consider only the distance between the ghosts with $R_{RMS} < 1000$ μm, so the leaver dramatically decreases to $L = 220$ mm.

Ghost	**Origin**	**R_{RMS} [μm]**	**Distance from L1 [mm]**	**Usable?**
LGSO-L1-S2	S2	7809	before dichroic	No
LGSO-L1-S2-S1	S2 + S1	~18000	+310	No
LGSO-L2-S1	S1	1281	+345	Limit case
LGSO-L2-S2	S2	1427	before dichroic	No
LGSO-L3-S1	S1	1522	+1639	Limit case
LGSO-L3-S2	S2	320	+1266	Yes
LGSO-L4-S2	S2	659	+1486	Yes
LGSO-L4-S1-S2	S2 + S1	1645	+2338	Limit case

Table 4.1: Summary of LGSO ghosts characteristics.

4.2 Expectation for the alignment residual errors

If the alignment residual error on the decenter of the LGSO has the same magnitude as the worst case scenario of the prototype lenses, then decenter $= 7 \pm 2$ μm. Assuming the case in which the optical lever is 220 mm, established by the maximum distance between the ghosts with $\mathrm{R_{RMS}} < 1000$ μm, the residual tilt results tilt $= 13 \pm 4$"; in the case in which the optical lever is 1993 mm, the maximum distance between the usable ghosts, the residual tilt results tilt $= 1 \pm 1$". The residual tilt is calculated in the scenario in which only the external ghosts are used in the alignment and the magnitude of the decenter is 7 ± 2 μm, while their sign is opposite. The alignment residual errors estimated from the results of the lab prototype and applied the Zemax ghost analysis of the LGSO are orders of magnitude lower than the requirements: the required maximum decenter is 1 mm, while the maximum required tilt is 360". To decrease the alignment residual of the LGSO, it would be clever to fit the position of the centroid of each usable ghost. The addition of the other 2 methods of alignment, and a weighted combination of techniques would further decrease the uncertainty; these are, namely, the LGS-WFS sampling of the light passing in the LGSO and the use of the back-reflection from a laser fired on the lenses. During the alignment of the LGSO, the MAT will be positioned in proximity of the corrective plate (distant ≈ 35 m from L1) and distant ≈ 35.4 mm from the LGSO-L2-S1 ghost and ≈ 37.2 mm from the LGSO-L2-S1 ghost; these are the 2 most external ghosts that can be used for the alignment and have R_{RMS} acceptable. The correspondence in the rotation of the focus knob of the MAT is ≈ 0.1 thick, according to the fit shown in fig.3.2. Instead, considering only the ghosts having $R_{RMS} < 1000$ μm, the distance from the MAT will be respectively ≈ 36.3 m from LGS-L3-S2 and ≈ 36.5 m from LGS-L4-S2. This would reduce the rotation of the focus knob of the MAT to ≈ 0.01 thick. It will be a weakness of the ghost alignment method, because the sensitivity of the human hand and eye may not be enough to distinguish the selected ghosts from the other, useless ones. A possible solution could be a motorized reduced ($\times 1000$) to use in a similar way to the micro-metric binary. Moreover, the fit could also be applied to a stack of ghosts, if they are concentric and especially if the focal length of the system is long enough to allow the ghosts to be in the FoV for a sufficient distance and to stack them. Another possible criticality could be the pixel size of the camera of the MAT: assuming that the $R_{80} \approx 10$ px to be observed and having a valid 2D fit of the profile, the combination of the pixel size and the maximum achievable zoom shall guarantee the aforementioned relation, expressed in eq.4.1

$$px_{size} = \frac{FoV}{zoom \times n_{px}} = \frac{R_{80}}{10} \approx 0.1 - 0.2 \mu\text{m} \tag{4.1}$$

It would be a great improvement of the setup to develop a real-time software able to automatically detect the centroid of the ghosts and its distance from the target position, thus it would provide the possibility to have accuracy ~ 1 μm or even less (assuming a similar scenario of the lab prototype).

The size of the ghost within $R_{RMS} \approx 1000$ μm should not be an issue for the LGSO alignment, in fact the FoV at the distance of the ghosts of the MAT would likely guarantee the possibility to observe them. According to fig.3.3, at 35 m distance the FoV is 731 mm. The maximum distance from the usable ghosts and the originating lens in the LGSO is smaller than this value, so in any position of the ghost, it is observable in the FoV of the MAT, nevertheless its tilt.

The PIP studied for the actual LSGO should be different from the one I built for the prototype: first of all it shall be a source illuminating in a range of wavelengths close to the Na-layer LGS one. Then, it should be integrated in the MAT system, set on the same axis to reduce the uncertainty on its decenter and tilt. The divergence shall be small enough to avoid vignetting on the lenses.

The position of the focus of the ghosts from the corrective plate and the dichroic within a few mm from the WFS should be notified to the MORFEO consortium in order to conduct an in-depth analysis on the pollution of the sensing.

Chapter 5

Conclusions

For the lab prototype demonstrator, the tested alignment technique resulted reliable and efficient in terms of achieved results. Using the reference of the cross of the MAT, which established the optical axis of the system:

- The PIP was aligned with $\mathrm{dec_x} = 4.1 \pm 0.8\mu\mathrm{m}$, $\mathrm{dec_y} = 14.8 \pm 0.8\mu\mathrm{m}$ and $\mathrm{tilt_x} = 0.8 \pm 0.1$", $\mathrm{tilt_y} = -2.3 \pm 0.1$"
- L1 was aligned with $\mathrm{dec_x} = 5 \pm 2\ \mu\mathrm{m}$, $\mathrm{dec_y} = 1 \pm 2\ \mu\mathrm{m}$ and $\mathrm{tilt_x} = 13 \pm 8''$, $\mathrm{tilt_y} = 7 \pm 8''$.
- L2 was aligned with $\mathrm{dec_x} = -2 \pm 2\ \mu\mathrm{m}$ $\mathrm{dec_y} = 7 \pm 2\ \mu\mathrm{m}$ and $\mathrm{tilt_x} = -5 \pm 2''$, $\mathrm{tilt_y} = 4 \pm 2''$.

The most difficult and expensive part, both for the cost of the needed instrumentation ($100 - 150$ k€) and for the effort required for the alignment of the setup, was the setting of the references. In fact, it was the main activity, comprehensive of MAT, PIP setup, and CBS alignments; hence, the ghost alignment technique is efficient for high-budget projects for which a certain accuracy is required. This technique is also suitable for frequent alignments and calibrations, for example, of a setup that is used daily and sometimes needs to be re-positioned due to the natural, gradual misalignment of its components. The MAT is a powerful instrument, but its calibration, thus the part in which it is set and locked as a reference, must be carried out with extreme care and accuracy, since it is a long procedure and gives the reference for all the following observations. Thus, the ghost alignment becomes an efficient technique only when the MAT is always in the same, locked position and only sometimes shall be recalibrated. The worst weakness of the MAT is its focal distance knob, optimized for steady back reflection and not for the search for ghosts in a long distance range, but this issue could be overcome by adopting a reduction gear for the rotation of the knob. I used both the software of the MAT and the iDS software to observe the sight of the MAT. Although the SW of the MAT is expensive, ≈ 10 k€, while the iDS one is free, the latter offers much more analysis tools, so I recommend using it. The FoV of the MAT will not be a problem, assuming the relation computed in fig.3.2 and, in the opposite, it will ensure the visibility of the ghosts even in a wide range of distances from the optical axis.

The alignment of the LGSO module to MORFEO shall satisfy the requirement from the Consortium of maximum acceptable tilt residual error = 0.1° = 360" and maximum acceptable decenter residual error = 1 mm. Assuming that the ghost alignment method applied to the LGSO gives the results comparable to the ones of the prototype, in the worst case scenario, the residual decenter error is $7 \pm 2\ \mu\mathrm{m}$ and the residual tilt error is 13 ± 4". The fact that the ghost alignment does not necessarily require the use of

additional elements and mechanics reduces the complexity of the procedure and the error budget: in fact, every new insertion shall be aligned to the reference of the MAT, introducing errors.
Hence, the ghost alignment technique represents a valid strategy for the LGSO alignment to the scientific optical path of MORFEO, resulting more accurate than a laser tracker method, and more reliable than the back-reflection and wavefront sensors alignment techniques.

Bibliography

[1] European Southern Observatory (ESO). *ELT – The Extremely Large Telescope*. Consulted on August 14, 2025. URL: `https://elt.eso.org/` (visited on 08/14/2025).

[2] Officina Stellare. *Officina Stellare*. Website. Accessed: 2025-09-29. URL: `https://www.officinastellare.com/`.

[3] J. et al. Farinato. *MAORY System MAIT Plan*. PLA E-MAO-000-INA-PLA-010. Version 01. Owner: Jacopo Farinato; Approved by: Paolo Ciliegi; Released by: Ugo Di Giammatteo. INAF, Apr. 2021.

[4] C. et al. Bodendorf. "Multi-zonal computer-generated holograms for high-precision optical adjustment purposes: Part I: Sensitivity and optical performance". In: *Optics Express* 27.10 (2019), pp. 13637–13654. DOI: `10.1364/OE.27.013637`.

[5] H. et al Yama. "Optical Alignment Method for the PRIME Telescope". In: *Journal of Astronomical Instrumentation* (2023). arXiv:2305.10796 [astro-ph.IM]. DOI: `10.48550/arXiv.2305.10796`.

[6] Kaspar von Braun. *Stellar Ghost Image*. Accesso: 28 settembre 2025. URL: `https://www2.lowell.edu/users/kaspar/obs_mishaps/images/stellar_ghost2.html`.

[7] Fordracer1 et al. *Anybody know how to process out a "Schmidt Ghost"?* `https://www.cloudynights.com/topic/254071-anybody-know-how-to-process-out-a-schmidt-ghost/`. Accesso: 28 settembre 2025. 2010. URL: `https://www.cloudynights.com/topic/254071-anybody-know-how-to-process-out-a-schmidt-ghost/`.

[8] S. et al. Kendrew. "Mid-infrared astronomy with the E-ELT: Performance of METIS". In: *arXiv preprint arXiv:1006.4669* (2010). arXiv: `1006.4669 [astro-ph.IM]`. URL: `https://arxiv.org/abs/1006.4669`.

[9] M. Xompero et al. "MORFEO (formerly known as MAORY) @ ELT: preliminary design of the adaptive mirrors". In: *Adaptive Optics Systems VIII*. Ed. by Laura Schreiber, Dirk Schmidt, and Elise Vernet. Vol. 12185. Proc. SPIE. Bellingham, WA: SPIE, 2022, 121857S. DOI: `10.1117/12.2630742`.

[10] K. M. et al. Hampson. "Adaptive optics for high-resolution imaging". In: *Nature Reviews Methods Primers* 1 (2021), p. 68. DOI: `10.1038/s43586-021-00065-7`.

[11] Claire et al. Max. "Cloud Structures on Neptune Observed with Keck Telescope Adaptive Optics". In: *The Astronomical Journal* 125.1 (2003), pp. 364–374. DOI: `10.1086/344943`.

[12] L. et al. Close. "The Magellan Telescope Adaptive Secondary AO System". In: *Proceedings of SPIE - The International Society for Optical Engineering*. Vol. 7015. 2008. DOI: `10.1117/12.789527`.

[13] B. et al. Neichel. “TIPTOP: A New Tool to Efficiently Predict Your Favorite AO PSF”. In: *arXiv preprint arXiv:2101.06486* (2021). URL: `https://arxiv.org/abs/2101.06486`.

[14] P. Ciliegi et al. “MAORY: A Multi-conjugate Adaptive Optics RelaY for ELT”. In: *The Messenger* 182 (2021), pp. 13–16. DOI: `10.18727/0722-6691/5216`.

[15] J. Farinato et al. “The MAORY/MORFEO MAIT strategy in Europe”. In: *Adaptive Optics Systems VIII.* Ed. by Laura Schreiber, Dirk Schmidt, and Elise Vernet. Vol. 12185. Proc. SPIE. Bellingham, WA: SPIE, 2022, p. 1218571. DOI: `10.1117/12.2629537`.

[16] L. et al. Busoni. “MAORY/MORFEO @ ELT: preliminary design of the adaptive optics subsystem”. In: *Adaptive Optics Systems VIII.* Ed. by Laura Schreiber, Dirk Schmidt, and Elise Vernet. Vol. 12185. Proc. SPIE. Bellingham, WA: SPIE, 2022, 121854R. DOI: `10.1117/12.2629606`.

[17] M. et al. Bonaglia. “MORFEO/MAORY Low-Order and Reference WFS module preliminary design”. In: *Adaptive Optics Systems VIII.* Ed. by Laura Schreiber, Dirk Schmidt, and Elise Vernet. Vol. 12185. Proc. SPIE. Bellingham, WA: SPIE, 2022, 121854O. DOI: `10.1117/12.2628794`.

[18] Axiom Optics. *A brief history of Shack–Hartmann wavefront sensing.* Axiom Optics Blog. Retrieved August 18, 2025, from `https://www.axiomoptics.com/blog/a-comprehensive-history-of-shack-hartmann-wavefront-sensing/`. 2025.

[19] M. Munari et al. “MORFEO LGSO Optical Design”. In: *Ground-based and Airborne Instrumentation for Astronomy X.* Ed. by Julia J. Bryant, Kentaro Motohara, and Joël R. D. Vernet. Vol. 13096. Proc. SPIE. Bellingham, WA: SPIE, 2024, 130965K. DOI: `10.1117/12.3019893`.

[20] D. Magrin. “Final optical design of MORFEO for the ELT”. In: *Adaptive Optics Systems IX.* Ed. by Kathryn J. Jackson, Dirk Schmidt, and Elise Vernet. Vol. 13097. SPIE, 2024, p. 1309754. DOI: `10.1117/12.3020359`.

[21] G. et al. Fiorentino. *MAORY science cases white book.* PLA E-MAO-000-INA-PLA-009. Version 1. E-ELT MCAO Construction – MAORY, 2017.

[22] European Space Agency. *Gaia – ESA’s billion-star surveyor.* ESA Science & Exploration website. Accessed: 2025-08-26. URL: `https://www.esa.int/Science_Exploration/Space_Science/Gaia`.

[23] M. et al. Uslenghi. “AETC: A powerful web-tool to simulate astronomical images”. In: *Modeling, Systems Engineering, and Project Management for Astronomy VII.* Ed. by George Z. Angeli and Philippe Dierickx. Vol. 9911. Proceedings of SPIE. © 2016 SPIE. SPIE. 2016, 99112U. DOI: `10.1117/12.2233621`.

[24] Taylor Hobson. *Micro alignment telescopes.* Taylor Hobson webpage. Retrieved August 19, 2025, from `https://www.taylor-hobson.it/products/alignment-level/micro-alignment-telescopes`.

[25] Taylor Hobson Limited. *Optical Alignment with the Taylor Hobson Limited Micro Alignment Telescope and its Accessories.* Technical Manual. Taylor Hobson Limited.

[26] FLIR Integrated Imaging Solutions Inc. *BFS-U3-200S6 – Blackfly S industrial camera (20 MP, Sony IMX183).* FLIR website. Accessed: 2025-08-27. URL: `https://softwareservices.flir.com/BFS-U3-200S6/latest/Model/spec.html`.

[27] Allied Vision Technologies GmbH. *Alvium 1800 U-2050 industrial USB3 Vision camera (20.2 MP, Sony IMX183)*. Allied Vision website. Accessed: 2025-08-27. URL: `https://www.alliedvision.com/en/products/alvium-configurator/alvium-1800-u/2050/`.

[28] Technical Manufacturing Corporation. *Gimbal Piston® – Air vibration isolation system*. TechMfg website. Retrieved August 19, 2025, from TechMfg website.

[29] Thorlabs. *HeNe Lasers: Red*. Thorlabs website. Retrieved August 20, 2025, from `https://www.thorlabs.de/newgrouppage9.cfm?objectgroup_id=1516`.

[30] Newport. *20BC17MB.1 Broadband Non-Polarizing Hybrid Cube Beamsplitter*. Newport website. Accessed: 2025-08-20. URL: `https://www.newport.com/p/20BC17MB.1`.

[31] Thorlabs. *Step-Index Multimode Fiber Optic Patch Cables: FC/PC to FC/PC – M122L01 (Ø200 µm, 0.22 NA, Low-OH, 1 m)*. Thorlabs website. Accessed: 2025-09-01. URL: `https://www.thorlabs.com/newgrouppage9.cfm?objectgroup_id=5794%5C&pn=M122L01`.

[32] Thorlabs. *Tungsten-Halogen Light Source (SLS201L/M)*. Thorlabs website. Retrieved August 20, 2025, from `https://www.thorlabs.com/newgrouppage9.cfm?objectgroup_ID=7269`.

[33] Thorlabs. *ACT508-250-A-ML f=250 mm, Ø2" Achromatic Doublet, SM2-Threaded Mount, ARC: 400-700 nm*. Thorlabs website. Accessed: 2025-08-20. URL: `https://www.thorlabs.de/thorproduct.cfm?partnumber=ACT508-250-A-ML`.

[34] Thorlabs. *AC254-075-A f=75 mm, Ø1" Achromatic Doublet, ARC: 400-700 nm*. Thorlabs website. Accessed: 2025-08-20. URL: `https://www.thorlabs.com/thorproduct.cfm?partnumber=AC254-075-A`.

[35] Thorlabs. *300 mm Linear Translation Stage with Integrated Controller (LTS300C/M)*. Thorlabs website. Retrieved August 20, 2025, from Thorlabs website.

[36] Newport. *10BC17MB.1 Beamsplitter Cube, Non-Polarizing, 25.4 mm, 400–700 nm Broadband*. Newport website. Accessed: 2025-09-01. URL: `https://www.newport.com/p/10BC17MB.1`.

[37] Thorlabs. *AC254-500-A - f = 502 mm, Ø1" Achromatic Doublet, ARC: 400 - 700 nm*. Thorlabs website. Accessed: 2025-08-20. URL: `https://www.thorlabs.com/thorproduct.cfm?partnumber=AC254-500-A`.

[38] Edmund Optics. *Introduction to Modulation Transfer Function*. Edmund Optics Knowledge Center (Application Notes). Accessed: 2025-08-30. URL: `https://www.edmundoptics.com/knowledge-center/application-notes/optics/introduction-to-modulation-transfer-function/`.

[39] P. et al. Rabou. *MAORY LGS WFS Design Report*. DER E-MAO-PL0-IPA-DER-012. Version 01. Owner: Jean-Jacques Correia; Approved by: Zoltan Hubert; Released by: Philippe Feautrier. IPAG-UGA / INAF, Jan. 2021.